INVESTIGATION OF HOLOGRAPHIC TESTING TECHNIQUES

Final Report

27 November 1968 Through 28 July 1971

C. M. Vest

E. N. Leith

W. R. Ribbens

D. W. Sweeney

J. R. Varner

December 1971
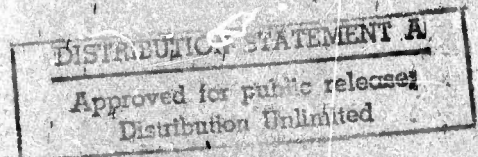
RADAR AND OPTICS LABORATORY

Willow Run Laboratories

INSTITUTE OF SCIENCE AND TECHNOLOGY

MISSING PAGE
NUMBERS ARE BLANK
AND WERE NOT
FILMED

NOTICES

Distribution. Initial distribution is indicated at the end of this document.

Final Disposition. After this document has served its purpose, it may be destroyed. Please do not return it to the Willow Run Laboratories.

DOCUMENT CONTROL DATA - R & D

(Security classification of title, body of abstract and indexing annotation must be entered when the overall report is classified)

1 ORIGINATING ACTIVITY *(Corporate author)*	2a. REPORT SECURITY CLASSIFICATION
Willow Run Laboratories of the Institute of Science and Technology, The University of Michigan, Ann Arbor	UNCLASSIFIED
	2b. GROUP

3 REPORT TITLE

INVESTIGATION OF HOLOGRAPHIC TESTING TECHNIQUES

4 DESCRIPTIVE NOTES *(Type of report and inclusive dates)*
Final Report, 27 November 1968 Through 28 July 1971

5 AUTHOR(S) *(First name, middle initial, last name)*

C. M. Vest, E. N. Leith, W. R. Ribbens, D. W. Sweeney, and J. R. Varner

6 REPORT DATE	7a. TOTAL NO. OF PAGES	7b NO. OF REFS
December 1971	xii + 137	81

8a. CONTRACT OR GRANT NO.	9a. ORIGINATOR'S REPORT NUMBER(S)
DAAG46-69-C-0017	
b. PROJECT NO	24200-28-F
ARPA Order No. 1245	
c.	9b. OTHER REPORT NO(S) *(Any other numbers that may be assigned this report)*
Program Code No. 8D10	
d	

10 DISTRIBUTION STATEMENT

11 SUPPLEMENTARY NOTES	12. SPONSORING MILITARY ACTIVITY
	Advanced Research Projects Agency Department of Defense Arlington, Virginia

13 ABSTRACT

This final technical report on holographic testing research includes a number of specific investigations conducted at the Radar and Optics Division of Willow Run Laboratories and at Cooley Electronics Laboratory of The University of Michigan. The investigations described include the following: (1) interferometric detection of microcracks; (2) detection of debonds in honeycomb sandwich structures, (3) real-time monitoring of stress-corrosion cracking, (4) interferometry of three-dimensional, refractive-index fields, (5) measurement of vibrational amplitudes, (6) holographic contouring, (7) optical determination of rms surface roughness, and (8) nondestructive inspection of shell casings and projectiles. The report also includes a brief introductory section on holography and holographic interferometry and a brief glossary of technical terms for the benefit of readers who are not acquainted with this technique.

DD FORM 1473 1 NOV 65

14 KEY WORDS	LINK A		LINK B		LINK C	
	ROLE	WT	ROLE	WT	ROLE	WT
Holography						
Interferometry						
Microcrack detection						
Debond detection						
Stress-corrosion cracking						
Refractive index fields						
Vibrational amplitude						
Holographic contouring						
Surface-roughness measurement						
Nondestructive testing						

24200-28-F

INVESTIGATION OF HOLOGRAPHIC TESTING TECHNIQUES

Final Report

27 November 1968 Through 28 July 1971

C. M. Vest

E. N. Leith

W. R. Ribbens

D. W. Sweeney

J. R. Varner

December 1971

Infrared and Optics Laboratory

Willow Run Laboratories

INSTITUTE OF SCIENCE AND TECHNOLOGY

THE UNIVERSITY OF MICHIGAN

Ann Arbor, Michigan

FOREWORD

This report was prepared by the Radar and Optics Division of Willow Run
Laboratories, a unit of The University of Michigan's Institute of Science and Tech-
nology, under the Advanced Research Projects Agency's Nondestructive Testing
Research Program, Contract No. DAAG46-69-C-0017, which began 27 November
1968. This final report covers work performed between 27 November 1968 and 28
July 1971. The Contract Monitor is Mr. Robert C. Grubinskas, Nondestructive
Testing Branch, Army Materials and Mechanics Research Center, Watertown, Massa-
chusetts.

The Principal Investigator for this project was E. N. Leith; C. M. Vest and W.
B. Ribbens served as associate investigators. Sections 2 and 3 of this report were
contributed by C. M. Vest. Sections 4, 5, 6, and 7 were contributed by C. M. Vest
and D. W. Sweeney, and Section 8 was contributed by J. R. Varner. Sections 9 and
10 were contributed by W. R. Ribbens of the Cooley Electronics Laboratory. The
work in Section 3 was partially supported by General Dynamics, Fort Worth, under
Air Force Contract No. AF33(657)13403, and that in Section 8 was partially spon-
sored by the Air Force under Contracts F33(615)-67-C-1814 and AF33(615)-68-C-
1310.

This work was submitted by the authors on 28 July 1971. This report has been
reviewed and approved.

iii

ABSTRACT

This final technical report on holographic testing research includes a number of specific investigations conducted at the Radar and Optics Division of Willow Run Laboratories and at Cooley Electronics Laboratory of The University of Michigan. A brief introductory section on holography and holographic interferometry and a brief glossary of technical terms are included for the benefit of readers who are not acquainted with this technique. The specific investigations described in this report consist of the following:

(1) Holographic interferometry was used to detect small cracks in high-strength steel structures by observing the response of the structures to differential loading. The results of these observations were compared with those of other, more standard inspection methods.

(2) Holographic inspection techniques for portable, hardwall construction panels and for an aircraft trim tab were developed and applied. The results of the trim tab inspection compared favorably with those of ultrasonic inspection.

(3) Real-time holographic interferometry was used to observe initiation and development of stress-corrosion cracking of Ti-6AL-4V in methanol. This technique has potential value as a laboratory tool for determining the susceptibility of materials to this type of damage.

(4) Basic research was conducted into various aspects of interferometry of three-dimensional, transparent objects. The principal result of this work is a method for determining three-dimensional, refractive-index fields from multidirectional, holographic interferograms.

(5) A new, coherent optical technique was devised for mapping the amplitude of a vibrating surface. It is more convenient in some respects than time-average holography and is primarily useful at fairly large amplitudes.

(6) Much work was done on the development of optical-contouring techniques, particularly of multiple-frequency holographic contouring. Included in the discussion of this work is a comparison of the applications of the various contouring techniques available.

(7) A method was devised to measure the rms surface roughness of metals by examining the way the surface scatters light. The use of holographic interferometry allowed the examination of curved surfaces. Results are compared with profilometer measurements.

(8) A series of experiments was carried out to evaluate the potential of holographic interferometry for inspection of shell casings and projectiles.

CONTENTS

FIGURES

TABLES

INVESTIGATION OF HOLOGRAPHIC TESTING TECHNIQUES
Final Report
27 November 1968 Through 28 July 1971

1
INTRODUCTION

This is the final technical report on a study of holographic testing techniques which began on 27 November 1968 and ended on 28 July 1971. The investigations reported herein were conducted at the Radar and Optics Division, Willow Run Laboratories, the Institute of Science and Technology, and at the Cooley Electronics Laboratory, both units of The University of Michigan. This report discusses the major technical accomplishments during the entire contract period. The accomplishments discussed fall into two categories: (1) direct development of holographic techniques for specific material-testing applications; and (2) investigation and development of holographic techniques which are of possible long-range applicability to material-evaluation procedures. In addition, Section 2 presents a brief introduction to basic optical holography and holographic interferometry for those readers who may not be familiar with the subject.

Holographic interferometry was found to have practical advantages. The technique was used for the detection of microcracks in metals, which we have investigated and demonstrated in several experiments. The test specimens were also studied by other existing NDT (nondestructive testing) methods, and the results are compared. The use of holographic interferometry for the detection of debonds in honeycomb, sandwich structures was investigated in two components: portable, hardwall construction panels used by the Army, and an aircraft trim tab supplied to us by the Air Force. The scheme developed for inspecting the construction panels was accurate; a different scheme used to test the trim tab was more cumbersome but attained results comparable to those attained by ultrasonic and radiographic techniques. Real-time holographic interferometry was shown to have significant potential as a tool for monitoring stress-corrosion cracking of metals. This potential could be developed as a rapid and convenient laboratory method for determining the susceptibility of metals to stress-corrosion cracking, particularly when the metal must be placed in special environments.

A new scheme for mapping the vibrational amplitude distribution of a vibrating surface was developed and demonstrated. This variable-sensitivity technique is simpler to apply than the normal procedure of time-average holography and in many instances operates satisfactorily in real time.

Analytical and experimental investigations have been conducted to develop schemes for determining the three-dimensional, refractive-index fields of transparent objects by holographic

interferometry. This application would be useful for three-dimensional stress analysis and for detection of nonhomogeneities. Schemes for obtaining multidirectional interferometric data of high quality and for varying the sensitivity of holographic interferometry were developed and demonstrated; also, significant progress was made in developing a scheme for analyzing multi-directional interferometric data.

Considerable work in holographic contouring was conducted during this investigation, which produced both basic developments and practical applications, with emphasis on multiple-frequency holographic contouring. It is shown that a low-sensitivity interferometry scheme can be based on holographic contouring. The features of several known optical-contouring techniques —both holographic and non-holographic —are compared from a practical point of view.

A new holographic scheme was developed for optically measuring the rms surface roughness of metals. Both analysis and experimentation are discussed, and experimental results are compared with profilometer data.

Finally, we conducted experiments to determine the feasibility of detecting various flaws in artillery shell casings and projectiles. Although this technique was not perfected, a number of practical difficulties were overcome, thus facilitating future developments in this area.

This report presents and summarizes the primary technical achievements of this investigation; however, some other portions of the work are not presented here. Appendix III contains the tables of contents from all previous technical reports from this contract to enable the reader to locate information regarding other aspects of the investigation if he so desires.

2
HOLOGRAPHY AND HOLOGRAPHIC INTERFEROMETRY

The report as a whole deals primarily with the application of holographic interferometry to problems of nondestructive inspection of material specimens and components. This section of the report is intended to serve as a brief introduction to the basic concepts of optical holography and holographic interferometry for those who are not already familiar with the technique. Appendix IV is a glossary of terms and their definitions to supplement this explanation of holography.

2.1. HOLOGRAPHY

Optical holography is a method of recording and later reconstructing an optical wavefront. The reconstructed wavefront duplicates the original with respect to both amplitude and phase distribution. By a simple extension of the method, polarization can also be recorded and repro-duced upon reconstruction. Most of the applications discussed in this report are based on the

fact that optical wavefronts can be reconstructed with such fidelity that they can be used to make interferometric comparisons.

Holography was originally developed by Gabor [1] who sought a new principle to provide a complete record of amplitude and phase distributions in a single recording (in contrast to conventional techniques, such as photography, which record only intensity distributions). He developed the basic theory of holography in considerable detail and conducted optical experiments to demonstrate its validity. His concept evolved from the fact that phase distributions could be recorded as interference patterns by superimposing coherent background illumination onto the wavefront of interest. His theory [2] showed that, upon reconstruction, a twin image, identical in amplitude to the recorded wavefront but with a phase distribution of opposite sign, was formed in addition to the wavefront of interest. Gabor's technique has been directly applied to make holograms of weakly scattering objects such as photographic transparencies, but it was limited by the fact that the twin image cannot readily be removed from the reconstruction.

In 1962, E. N. Leith and J. Upatnieks [3] of The University of Michigan, drawing on an analogy between Gabor's wavefront reconstruction technique and elementary communication theory, demonstrated an extension of the technique in which the twin image could be readily removed. The same authors [4] showed that their technique could be used to record and reconstruct wavefronts of light scattered by three-dimensional diffuse objects. The development of the Leith-Upatnieks' off-axis holography and of highly coherent laser light sources has lead to widespread and continually expanding interest in and application of holography. All of the applications of holography discussed in this report are based on the off-axis method.

The theory and practical realization of off-axis holography can be described with reference to the optical arrangement depicted in Fig. 1. The beam emerging from the laser is divided by a beam splitter. The portion reflected by the splitter is expanded by an objective lens system, and extraneous diffraction patterns (noise) are filtered out by passing the beam through a small pinhole aperture placed at the focus of the objective. This expanded and filtered beam, which is referred to as the "object beam," is scattered by the test specimen toward the hologram. It is this scattered wavefront which we wish to record. The portion of the laser beam which is transmitted by the splitter is expanded, filtered, and collimated, and also impinges on the hologram. This portion is referred to as the "reference beam." Physically, the hologram is a plate of photographic film, and the holographic recording process consists of simply exposing this film simultaneously to both the reference and the object beams.

The wavefronts of the monochromatic reference and object beams at the hologram plane can be represented by

$$\underline{U}_R(x, y) = U_R \exp\left(-i2\pi \frac{\sin \theta}{\lambda} x\right) \tag{1}$$

3
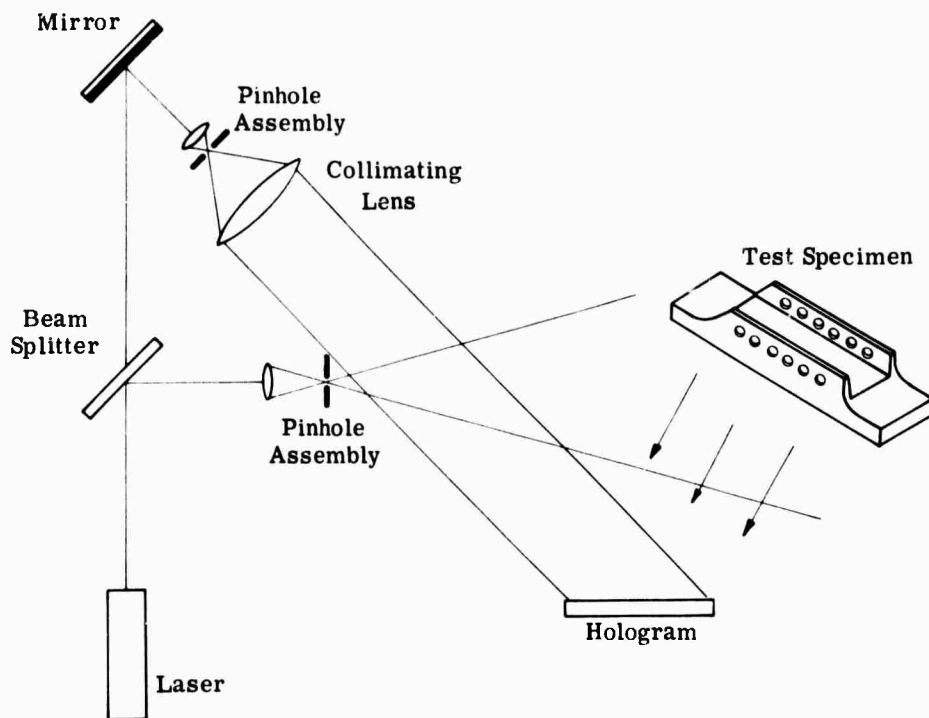
FIGURE 1. EXPERIMENTAL SETUP

and

$$U_O(x, y) = U_O(x, y) \exp\left[-i\phi(x, y)\right] \tag{2}$$

respectively. θ is the angle of the reference wave with respect to the hologram plane. In these expressions for the complex amplitudes, U_R and U_O, the time dependence is ignored, since it is of a constant temporal frequency; λ is the wavelength of the light, and $\phi(x, y)$ describes the phase distribution of the light scattered by the object. Here, U_R is assumed to be constant. Photographic emulsion responds to the intensity of the incident wavefront; hence, the intensity distribution

$$I(x, y) = \left|U_R + U_O\right|^2 = \left|U_R\right|^2 + \left|U_O\right|^2 + U_R U_O^* + U_R^* U_O \tag{3}$$

is recorded on the hologram when it is exposed simultaneously to the reference and object beams. The film can be developed so that its amplitude transmittance, $t(x, y)$ is linearly related to exposure; thus

$$t(x, y) = t_b + \beta\left[\left|U_O\right|^2 + U_R U_O \exp(i2\pi\alpha x) + U_R U_O^* \exp(-i2\pi\alpha x)\right] \tag{4}$$

4

where the constant t_b is the transmittance bias, β is the slope of the transmittance-versus-exposure curve of the film, and $\alpha \equiv (\sin \theta)/\lambda$ is the spatial frequency of the reference beam.

Reconstruction is accomplished by illuminating the developed hologram with the reference beam $\underline{U}_R$. By definition of amplitude transmittance, the amplitude distribution just behind the hologram is given by the product $t \cdot \underline{U}_R$. This transmitted field consists of four components:

$$\underline{U}_1 = t_b \underline{U}_R \qquad \underline{U}_3 = \beta U_R^2 \underline{U}_O$$

$$\underline{U}_2 = \beta \underline{U}_R |\underline{U}_O|^2 \qquad \underline{U}_4 = \beta U_R^2 \underline{U}_O^* \exp(-i4\pi\alpha x) \tag{5}$$

The components $\underline{U}_1$ and $\underline{U}_2$ represent waves propagating in the general direction of $\underline{U}_R$. The component $\underline{U}_3$ is of primary interest to us, since it is proportional to the original object wave $\underline{U}_O$. This component is deflected by the hologram at such an angle that if one looks through the hologram, a three-dimensional virtual image of the object will be seen to occupy the original object position. The remaining component $\underline{U}_4$ represents a real image, and this wave is seen to propagate in a different direction than does $\underline{U}_3$. Thus, the removal of the twin image which degraded the Gabor hologram is accomplished by the off-axis method developed by Leith and Upatnieks. The key point is that the object wave $\underline{U}_O$ can be reconstructed in detail in terms of both amplitude and phase distribution.

Physically, a highly complicated interference pattern is recorded on the film plate when it is exposed to the coherent object and reference waves. After it is developed, this film or holo-gram acts as a diffraction grating. The above analysis shows that when this grating is illumi-nated by the reference beam, the wavefront of the first diffracted order is a precise duplicate of the original object wave. A slight extension of this method allows recording and reconstruction of the polarization of the object wave as well as of its amplitude and phase [5, 6].

2.2. HOLOGRAPHIC INTERFEROMETRY

The principle underlying holographic interferometry is that the wavefront scattered by an object can be reconstructed so precisely that it can be compared interferometrically with the light actually emanating from the object, or with the reconstruction of another hologram of the object. The use of off-axis holography as a tool for interferometry was developed independently by several different researchers, among whom are Horman [7], Powell and Stetson [8], Haines and Hildebrand [9], Burch [10], and Heflinger, Wuerker, and Brooks [11].

In most of the applications discussed in this report, holographic interferometry is used to generate fringe patterns indicative of the displacement of diffusely reflecting surfaces in response to some type of loading. For a discussion of these applications, it is convenient to separate holographic interferometry into three categories: (1) two-exposure interferometry,

(2) real-time interferometry, and (3) time-average holography. Each of these categories of holographic interferometry is briefly discussed below, as is the related technique of holographic contouring.

2.2.1. TWO-EXPOSURE INTERFEROMETRY

Consider again the experimental apparatus depicted schematically in Fig. 1. The film (hologram) is exposed simultaneously by the reference wave, U_R, and by the object wave, $U_O = U_O(x, y)$ $\exp[-i\phi(x, y)]$. Following the first exposure, the test specimen is displaced or distorted (e.g., by the application of a mechanical load); the wavefront scattered by the test specimen (object) may be denoted by $U_O' = U_O'(x, y) \exp\left\{-i[\phi(x, y) + \Delta\phi(x, y)]\right\}$ at the hologram plane. A second exposure is then made on the same film plate while it is illuminated simultaneously by the reference wave U_R and by the perturbed object wave U_O'. Because of the linearity of the process, one can then consider two holograms —one of U_O and one of U_O' —to be recorded on the same photographic plate. When this plate is properly developed and illuminated by the reference wave U_R alone, both wavefronts are simultaneously reconstructed and interfere with each other. Looking through the hologram, one views a realistic, three-dimensional image of the object overlaid with a pattern of interferometric fringes. The fringes are indicative of the phase disturbance $\Delta\phi(x, y)$ caused by perturbing the object. This phase disturbance can be related to the field-of-surface displacement of the object.

Haines and Hildebrand [9] and Aleksandrov and Bonch-Bruevich [12] were the first to work on the problem of fringe interpretation in holographic interferometry of diffusely reflecting objects. Recently, Sollid [13] has derived a general relation by which holographic interferometry can determine small displacements. His analysis contains the results both of Haines and Hildebrand and Aleksandrov and of Bonch-Bruevich, as well as those of Ennos [14], who considered the special case of in-plane displacements. Tsuruta, et al. [15], Vienot, et al. [16], and others have also contributed to the literature on fringe interpretation.

For our present purposes, we need not be concerned with the details of fringe analysis. It may be noted, however, that the fringe at a point on the object is determined basically by the displacement of that point in the direction of the bisector of the angle between the ray connecting the light source to the point and the ray connecting the point to the observation position. For most of the interferograms presented later in this report, the fringe is approximately the component of displacement normal to the surface of the object.

2.2.2. REAL-TIME INTERFEROMETRY

Consider again the photographic plate in Fig. 1 to be exposed simultaneously by the reference and object waves. If this hologram is developed, replaced precisely in its original position, and illuminated by both the object and reference beams, one would view the actual and reconstructed

6

objects simultaneously. If the object is then displaced or distorted, the actual and reconstructed waves will interfere with each other, thereby providing information about the displacement or distortion. This interferometry technique is equivalent to the two-exposure technique except that experimental observations can be made in real time.

2.2.3. TIME-AVERAGE HOLOGRAPHY

Time-average holography is an interferometric technique for analysis of vibrating surfaces. It may be thought of as a generalization of two-exposure holography to a continuous time exposure of a vibrating surface. Suppose the test specimen in Fig. 1 is vibrating sinusoidally; a hologram would be recorded by exposing the film to both the reference and object waves for a time which is long in comparison to the period of vibration. If the resulting hologram is reconstructed by illumination with the reference wave, an image would be produced of the test specimen overlaid with interference fringes, which are indicative of the vibrational mode shape.

Powell and Stetson [8], who first developed this technique, analyzed the process by considering the effect on the hologram exposure of modulation of the object wave caused by the vibration. Their analysis shows that the brightness of the reconstructed hologram is proportional to $J_0^2[M(x_o, y_o)]$, where J_0 is the zero-order Bessel function of the first kind, and the modulation depth M at a point (x_o, y_o) on the vibrating object is given by $M = \frac{4\pi}{\lambda}A$, where A is the local amplitude of vibration. The fringes superimposed on the object, therefore, give a measure of the local amplitude of vibration.

The essence of time-average holography can be understood on simple physical grounds. The brightest areas on the hologram will be nodal areas, i.e., those parts of the object which do not move during the recording of the hologram. The other portions of the object surface will spend more time at their positions of maximum deflection than at intermediate positions; hence, the interference fringes on the reconstructed object essentially indicate the surface displacement from one maximum deflection to the other.

Stetson [17] has recently presented a rigorous treatment of holographic interferometry including time-average holography. Biedermann and Molin [18] and Stetson and Powell [19] have described real-time techniques for vibration analysis. Archbold and Ennos [20] have used a stroboscopic technique for holographic interferometry which offers certain advantages over the real-time methods of Biedermann and Molin or of Stetson and Powell.

2.2.4. HOLOGRAPHIC CONTOURING

Thus far we have discussed the use of holography to produce interferometric fringes when the surface of an object is physically displaced or distorted. Holographic contouring is a technique for superimposing fringes of constant range or depth on the image of an object. These fringes result from the interference between two holographic images which are optically dis-

placed from each other. Holographic contouring was first accomplished by Hildebrand and Haines [21], who described two contouring techniques. In the first, two consecutive holograms of the object are recorded on the same photographic plate; the point source which illuminates the object is physically displaced between exposures. In the second, two consecutive holograms are recorded on the same photographic plate, the first in light of one wavelength and the second in light of a different wavelength. Closely related to this latter technique is that reported by Tsuruta et al. [22] and extended by Zelenka and Varner [23], in which the object to be contoured is submerged in a fluid, the refractive index of which is changed between two consecutive hologram exposures. In each of these techniques, reconstruction of the hologram produces an image of the object overlaid with contour fringes, the precise interpretation of which depends on the recording geometry and technique used.

3
DETECTION OF MICROCRACKS

A portion of the investigation reported in this section was sponsored by the Fort Worth Division of General Dynamics. The remainder was conducted under the Advanced Research Projects Agency (ARPA) contract.

3.1. INTRODUCTION

The objective of the research program reported here was to determine if holographic interferometry can be used to detect the existence of microcracks in metals. In particular, we investigated the detection of small cracks induced in high-strength, aircraft, structural steel. Various methods of producing the strain fields required for this technique were tried and evaluated. The experimental results were compared with tests on the same specimen by other, well established, nondestructive, crack-detection techniques.

3.2. EXPERIMENTAL APPARATUS

3.2.1. OPTICAL APPARATUS

The basic experimental apparatus is shown in Fig. 1. The beam of laser light is divided by a beam splitter into a reference beam and a signal beam. Each of these beams is expanded when it is passed through a pinhole assembly consisting of a microscope objective and a 15-μm pinhole spatial filter. A collimating lens is used to produce a plane reference wave, while the test specimen is illuminated by the expanding signal beam. For our procedure, a 20-mW He-Ne laser was used as a light source, and all holograms were recorded on Kodak 649F spectroscropic plates. Since the experiment involved comparison of wavefronts separated in time, it was obvious that mechanical stability of the entire system is of critical importance. The optical

paths had to remain constant within 1/4 wavelength, not only during exposure of the plate but during the time interval between exposures as well. We met this requirement satisfactorily by using rather massive components placed on a large granite slab. The entire system was mounted on air-filled innertubes in order to isolate it from building vibrations.

3.2.2. SPECIMEN PREPARATION

A 5-in.-wide and 30-in.-long channel was fabricated of D6 ac steel. Two ribs extended from the edges of the 0.69-in.-thick channel base. Each rib was approximately 0.13 in. thick and 1.23 in. wide. Six 5/16-in. holes were drilled into each rib and reamed with a tapered reamer. The channel was heat-treated to 230 ksi (double-tempered to 1025°F).

Controlled-length cracks were artifically introduced near some of the holes. To accomplish this, a 0.03-in. notch was cut into the hole, and the area around it was burned with an arc from a 500-V capacitance discharge. A Taper-Lok bolt was then inserted and torqued to 50 in-lb. The crack was initiated by a 6 normal solution of hydrochloric acid contained by a dam of vacuum putty. We controlled crack length by increasing the torque while microscopically observing the crack growth. After inducing stress-etch cracking, we used a tapered reamer to remove the notched and burned area and to provide a final control on crack length. The specimen received no cleaning or surface preparation.

Crack lengths and hole conditions were varied to provide defect-free reference holes as well as holes with radial cracks of lengths ranging from C.01 in. to 0.44 in. Two holes which had untempered martensite deposits were also included. The specific condition of each hole is indicated in Table 1, which also gives the letters with which the holes were coded. The optical investigators did not know the conditions of the holes at the time the tests were conducted.

3.3. EXPERIMENTAL PROCEDURE

With one exception, the experiments were conducted by the double-exposure holographic interferometry method. One hologram of the test specimen in some initial state was recorded. The specimen was then stressed, and a second hologram was recorded on the same photographic plate. When the resulting composite hologram was reconstructed, the resulting interference pattern indicated the displacement field of the surface of the test specimen. In this investigation, we were concerned with finding anomalies in the interference fringe pattern, which might indicate the presence of microcracks.

During the course of the investigation, several schemes of thermal, vibratory, and static mechanical loading were tried. Thermal stressing by electrical heating and cooling with liquid nitrogen led to a number of practical difficulties (e.g., transient stress fields, lack of appropriate stress localization, and frost formation). An attempt to use time-averaged holographic

TABLE 1. CONDITION OF HOLES AND COMPARATIVE EXPERIMENTAL RESULTS

Test Hole No.	Condition of Tested Hole	Cracks/Anomalies Indicated by:			
		Holography	Magnaflux	Eddy Current	X-Ray
A	0.02-in. Crack	Yes	Yes	Yes	No
B	No Defect	No	No	Yes	No
C	0.01-in. Cracks Untempered Martensite	Yes	Yes	Not tested	No
D	0.03-in. Crack	Yes	Yes	Not tested	No
E	Untempered Martensite	Yes	No	Yes	No
F	0.44-in. Crack	Yes	Yes	Yes	Yes
G	0.10-in. Crack	Yes	Yes	Yes	No
H	No Defect	No	No	Yes	No
I	0.20-in. Crack	Yes	Yes	Yes	Yes
J	0.11-in. and 0.17-in. Cracks	Yes	Yes	Yes	No
K	No Defect	No	No	Yes	No
L	No Defect	No	No	Yes	No

interferometry [8] while the specimen was excited to vibratory motion was also unsatisfactory; the vibration was evidently too complex to make such a technique useful.

Several means of static loading were utilized during the investigation—e.g., placing the member in flexure, clamping the flanges in various ways, and pushing on the hole from behind. While all of these methods of loading produced interferometric fringe patterns, none of them appeared to produce sufficient differential displacement in the vicinity of the crack to yield observable fringe anomalies.

Differential torquing of tapered bolts, one of the simplest techniques attempted, produced the desired result. After a tapered bolt was drawn into the hole by application of an initial torque on the bolt, the first recording was made on the hologram plate. Additional torque was then applied to the bolt, and a second exposure was made. At least in the case of the longer cracks, this procedure produced a striking anomaly in the fringe pattern in the vicinity of the crack. This technique and the interpretation of the results are more fully discussed in the following section.

3.4. EXPERIMENTAL RESULTS

The discussion of the experimental results will be confined to results of those experiments in which the stressing of the test specimen was achieved by differential torquing of a tapered bolt. Of all the methods attempted, this appeared to be the most practical.

Figure 2 shows the fringe patterns produced by differential torquing of the tapered bolts. The head of the bolt can be seen extending from the hole and casting a shadow on the specimen. These photographs were produced without the aid of lenses by direct exposure of a sheet of film to the real image. It should be noted that because of fringe localization effects, some of the photographs lack the fringe clarity obtained when the hologram is viewed directly.

The changes in torquing of the bolts between exposures were on the order of 10 to 70 in.-lb. although this is not of particular importance, since our interest was in anomalies in the fringe pattern rather than in a quantitative correlation of loading and fringe pattern.

0.10-in.- to 0.44-in.-long cracks produced striking and obvious anomalies in the fringe pattern, as can be seen in Fig. 2, parts f, g, i, and j in comparison with parts b, h, k, and l of holes with no defects. Fringe pattern anomalies produced by cracks a decade smaller in length, although they are present, are not as obvious, as can be noted in parts a, c, and d of Fig. 2. Thus, cracks of 0.10 in. or longer seem to be readily detectable by this method. All holes which contained cracks on the order of 0.01 in. to 0.03 in. yielded fringe patterns which differed from those around holes with no defect; however, the fringe patterns did not render the crack or its location apparent. The holes shown in parts c and e were known to contain deposits of untempered martensite. The fringe patterns indicated are obviously different from those produced around flawless holes, but this is not sufficient evidence upon which to base any conclusion regarding the detection of such deposits.

Table 1 lists the specific condition of each hole and the conclusions drawn from the holographic tests. Also indicated in this table are the results of other tests conducted by General Dynamics on the same specimen by Magniflux, eddy-current, and x-ray techniques; further details are given in Ref. [24]. The eddy-current probe, although extremely sensitive, yielded false signals—i.e., indicated cracks which did not exist. The table shows that the holographic technique compares favorably with the other methods.

3.5. CONCLUSIONS

The detection of cracks by holographic interferometry has been shown not only to be feasible, but to offer distinct advantages over existing techniques. No special cleaning or surface preparation is required; paint, thin plating, dirt, or mild surface corrosion should have no effect on the application of the method. In general, microscopic examination is not required. Also, a permanant three-dimensional record of the test is obtained, which can be examined, even microscopically, at a time or location other than when or where the test was conducted. In addition, the method should also be applicable to nonmetallic materials and to materials which have anisotropic properties. No stringent restriction is placed on the shape of the member being tested.

(a) Area Surrounding Hole A

(b) Area Surrounding Hole B

(c) Area Surrounding Hole C

(d) Area Surrounding Hole D

FIGURE 2. HOLOGRAPHIC INTERFEROGRAMS OF TEST SPECIMEN

(e) Area Surrounding Hole E
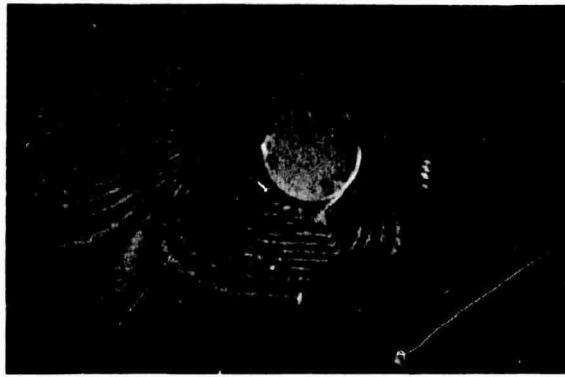
(f) Area Surrounding Hole F

(g) Area Surrounding Hole G

(h) Area Surrounding Hole H

FIGURE 2. HOLOGRAPHIC INTERFEROGRAMS OF TEST SPECIMEN (Continued)

(i) Area Surrounding Hole I

(j) Area Surrounding Hole J

(k) Area Surrounding Hole K

(l) Area Surrounding Hole L

FIGURE 2. HOLOGRAPHIC INTERFEROGRAMS OF TEST SPECIMEN (Concluded)

The method appears to be suitable for use in inspection of structures on an assembly-line operation. Although rather stringent, mechanical stability requirements are inherent in the use of optical holography, the technique may be made suitable for testing structures which are in service. This expansion of the technique might be accomplished by rapid loading between pulsed-laser holographic exposures, or by use of a reference beam which has been reflected by part of the surface under inspection in order to reduce the fringes caused by extraneous motion. This development would permit inspection of assembled structures when plating films and paints could not be removed, when volatile cleaning solvents could not be used, or when direct, visual examination could not be performed.

Detection of the small number of specimen holes which had deposits of untempered martensite does not justify a claim that optical holography can detect this condition reliably. The results do suggest a need for further study of the effect of local metallurgical differences on interferometric patterns indicative of surface displacement.

The results of the interferometric inspection considered here are highly dependent on the size, shape, and mechanical properties of the specimen, on the nature and size of the defect, and on the method of application and magnitude of the load. It is therefore difficult to make general statements regarding the applicability of the technique. Each specific application must be considered to determine whether or not a viable test can be developed.

3.6. SUMMARY

It was found that holographic interferometry could be used to detect the presence of small cracks in metallic structures. These cracks are detected by their effect on the surface displacement of the specimen when it is subjected to some load. The accuracy with which radial cracks extending from bolt holes in a high-strength steel could be located was as great as by any other inspection method. The holographic method has the advantage over other methods of permitting inspection of relatively large areas without point-by-point probing. Also, no cleaning or surface preparation of the material is required. It is generally difficult to determine in advance whether the technique is applicable to a particular inspection application.

4
DETECTION OF DEBONDS

4.1. INTRODUCTION

The detection of debonds in honeycomb panels has been one of the most successful applications of holographic interferometry to nondestructive testing. It has been used in industrial as well as laboratory testing (see, for example, Refs. 25 and 26). We have applied holographic interferometry to the inspection of an aircraft trim tab and of portable, hardwall, construction

panels. As in virtually all holographic nondestructive testing applications, these inspection pro-
cedures were based on the ability of holographic interferometry to display small deformations
of the object surface. A hologram of the test specimen in some initial configuration is recorded
on a photographic plate. The specimen is then subjected to a small load, and a second hologram
is recorded on the same photographic plate. When these two holograms are simultaneously
reconstructed, the viewer observes a realistic, three-dimensional image of the specimen over-
laid with interferometric fringes which are indicative of the surface displacement field. If there
is a debond between the core and skin, the surface displacement is locally perturbed; hence,
the presence of the debond is manifested as a local anomaly in the fringe pattern.

Since the experimental procedures used in testing the trim tab were significantly different
than those used in testing the construction panels, these two applications will be discussed
separately below.

4.2. INSPECTION OF PORTABLE HARDWALL CONSTRUCTION PANELS

4.2.1. BACKGROUND

This section deals with the testing of honeycomb panels used by the Armed Forces as con-
struction materials to fabricate portable hardwall buildings, such as medical stations and kitchens.
After such panels have been in service for a period of time, large areas of the adhesive between
the aluminum skin and the paper core tend to rupture. This problem was brought to our attention
by Mr. Morris Budnick of the Army Natick Laboratories.

It has been suggested that these large debonded areas may grow from smaller debonds that
are introduced during the manufacturing of the panel. These small debonded areas, which are
not large enough to affect the macroscopic mechanical properties of the panel just after manu-
facture, could serve as nucleation sites for subsequent development of larger debonds. This
section reviews the testing methods we have developed to locate small debonds in these panels.

4.2.2. EXPERIMENTAL PROCEDURE AND RESULTS

A typical experimental layout is shown in Fig. 3. A beam of laser light is divided into an
object beam and a reference beam which simultaneously strike the photographic plate to produce
the hologram. This system can be used for multiple-exposure interferometry or for real-time
interferometry. This application required recording holograms of large surface areas of the
panel. This requirement presented some difficulty, since the field size was severely limited
by the relatively short (25-cm) coherence length of our He-Ne laser. To alleviate this restriction,
we modified the laser by inserting a low-reflectivity mirror into its cavity, a technique developed
by G. D. Currie [27] of our laboratory, which greatly increases the coherence length. It differs
from other reported coherence extension techniques in that reduction of the total power output
is less than 10%, while the coherence length is extended by an order of magnitude. Figure 4

16
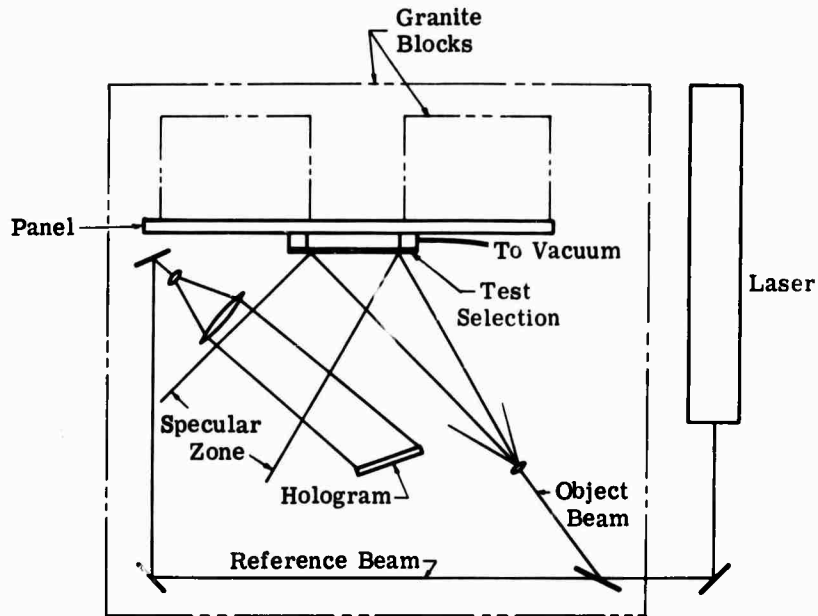
FIGURE 3. OPTICAL ARRANGEMENT FOR TESTING
HONEYCOMB PANELS
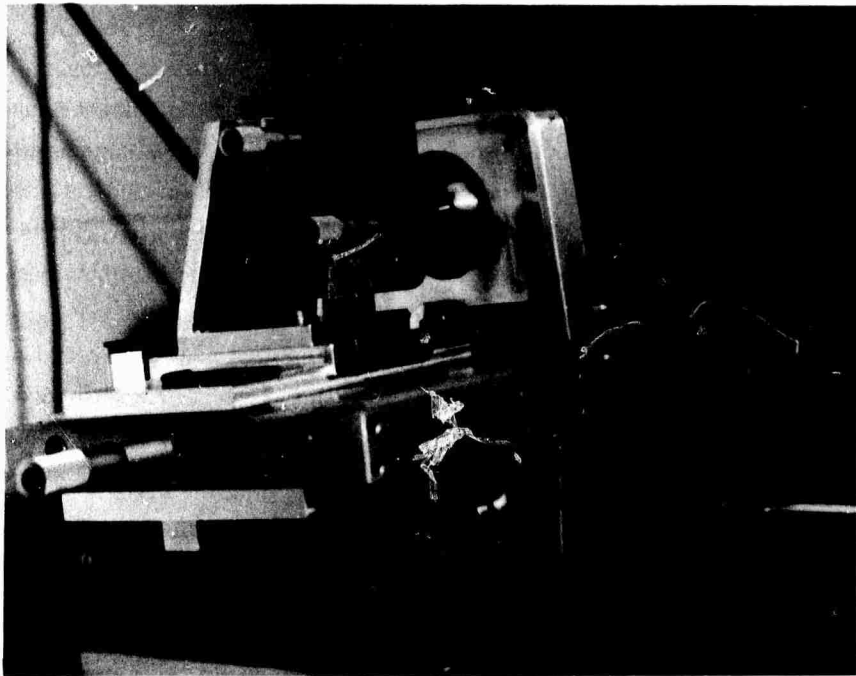
FIGURE 4. He-Ne LASER MODIFIED FOR MODE SELECTION

is a photograph of the modified laser. Alignment controls for the mirror are visible at the front of the laser. By proper alignment of the mirror, a single mode can be selected. Figure 5a shows the spectrum of the laser prior to insertion of the mirror into the cavity, and Fig. 5b shows the spectrum of the modified laser after the selection of a single mode.

The panels being tested are approximately 2-in. thick and have a honeycomb core of water-migration-resistant paper and a light-guage aluminum skin. The honeycomb cells are filled with a foam thermal insulation. Figure 6 shows a section of one of the panels. In preliminary tests, an artificial bond defect was introduced by cutting into the paper core very close to the skin. This defect is outlined with tape in the figures which follow.

Figure 7 shows reconstructions of multiple-exposure holograms produced by static loading. The photographic plate was exposed three times instead of the usual two. It was first exposed with a hemispherical probe pressing lightly against the front surface of the panel. The probe was then pushed 0.001 in. further into the panel surface, and a second exposure was made. Finally, the probe was moved 0.001 in. more into the panel surface, and the plate was exposed a third time. This technique was first proposed by Burch and his colleagues [28]. The exposure time was increased 10% for each successive exposure, as suggested by Biedermann [29], to produce equally intense reconstructed images.

Basically, each exposure pair produces a separate interferogram; the first and second, the second and third, and the first and third exposure pairs each produce a separate fringe pattern. These three superimposed fringe patterns combine to form a moiré pattern. If the displacements between exposures are all equal, all the fringe patterns have harmonically related fringe frequencies. The moiré pattern produced by the interferometric fringes is the same as that produced by a double-exposure hologram made from only the first two exposures, except that low-amplitude, high-frequency fringes fall between the broader fringes. If the displacements between exposures are not equal, the resulting interferometric fringes do not beat together to form high-visibility moiré fringes, as they do in the first case. The fringes tend to wash out and form patterns with varying visibility. This technique can be used to detect nonlinear responses to a deforming load by observation of the visibility of the resulting fringes. We used the above technique to determine if it would facilitate identification of debonds.

Figure 7a shows a reconstruction of a triple-exposure hologram; the probe is about 1 in. to the left of the defect. The moiré fringe pattern is clear and has high visibility. There is some change over the defect in the slopes of the fringes. This change is so slight, however, that flaws could not be detected reliably. Figure 7b shows a reconstruction a hologram made when the probe is directly over the defect; the defect is clearly indicated by the circular fringes around the probe. Over the remainder of the panel, the fringes are not nearly as distinct as those in Fig. 7a; hence, the movements of this portion of the panel between the three exposures were unequal.

(a) Unmodified   (b) Modified for Mode Selection
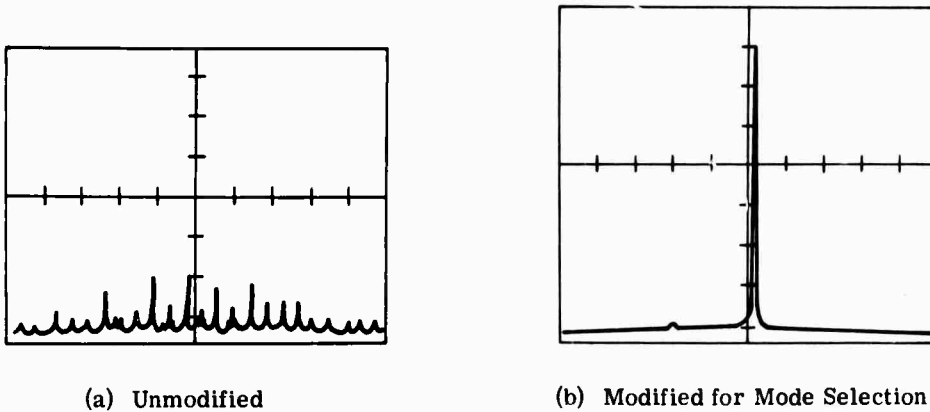
FIGURE 5. FREQUENCY SPECTRUM OF He-Ne LASER
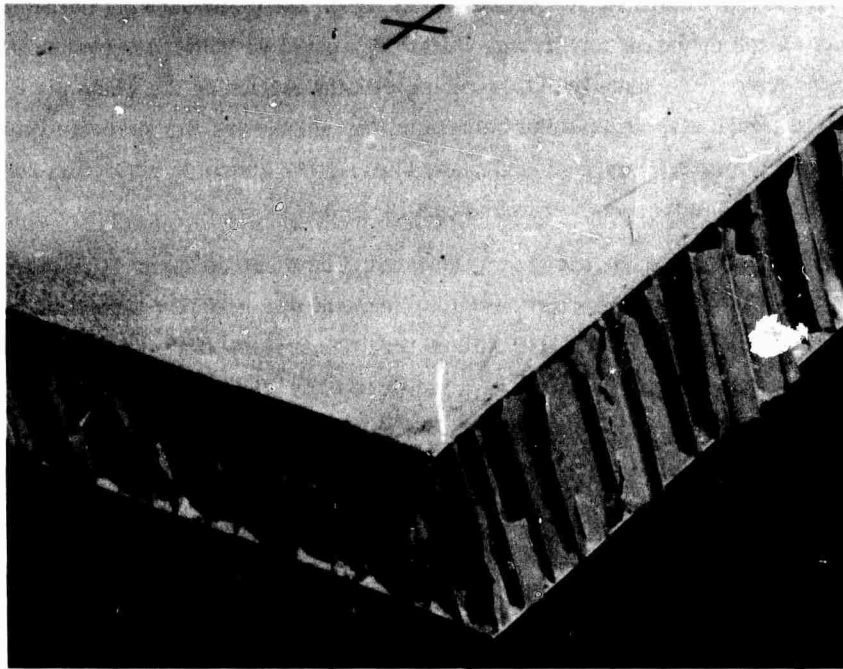
FIGURE 6. HARDWALL PANEL WITH PAPER CORE AND ALUMINUM
SKIN

Although this technique and similar double-exposure and real-time methods were found to
work, they require point-by-point probing of the surface. To take advantage of the whole-field
nature of holographic interferometry, we next loaded the panels by applying a uniform vacuum
to their front surfaces, which were then observed through a viewing window. Figure 8 shows the
system used. A chamber was constructed of a circular aluminum ring with a 1/4-in.-thick glass
cover plate and an aperture of 7 in. An O-ring in the back of the aluminum ring sealed it to the

19

honeycomb panel. With the use of this chamber, the pressure on the face of the panel could be either increased or decreased between exposures. We found that a differential vacuum technique achieved the best results because a vacuum tends to expand or open debonded areas rather than to compress them. Also, it was easier to seal the glass cover plate to the panel. Using this procedure, we placed the test cell against the panel, a 4-psi vacuum was introduced, and the first holographic exposure was made. The vacuum was then decreased to 2-psi, and the hologram was exposed a second time. The resulting interferometric fringes essentially represent contour lines of the difference in the normal surface displacements between the two exposures. A typical interferogram is shown in Fig. 9. The debonded area is characterized by an abrupt increase in fringe frequency, which indicates that regions over debonded areas are less restrained and move further than a bonded area under the same load.

Obviously, when the pressure in the test region changes, the glass viewing port deforms slightly. This introduces an extraneous fringe shift which could be bothersome when the interferograms are interpreted. We have found, however, that the motion of the glass plate will introduce only slight fringe distortion if the hologram does not record the specular reflections from the glass. To obtain maximum sensitivity and to avoid the specular reflection zone, the hologram should be placed in the location indicated in Fig. 3.

At first, it would appear that the viewing window could be made as large as necessary to analyze an entire panel; however, the maximum displacement of a circular plate under uniform pressure increases as the fourth power of the diameter. Thus, if the diameter were doubled, the fringe frequency would increase roughly by a factor of eight. The fringe anomalies, which indicate debonds, would then become less obvious to the viewer. This effect can be seen in Fig. 10. Figure 10a shows an interferogram with a 7-in.-diameter test window; the fringes over the defective area, which is outlined in black, are noticeably distorted. An interferogram of the same defect but with a 19-in. viewing window is shown in Fig. 10b; although the fringes are still perturbed, the effect is not nearly as pronounced. If the defect were smaller, or in a region of higher fringe frequency, the defect could conceivably be missed. This does not mean that large panel areas cannot be tested simultaneously, but a series of smaller loading chambers should be used. The technique of fringe control, recently developed by Champagne and Kersch [30, 31], has greatly alleviated this difficulty.

The National Bureau of Standards provided us with panels which included intentionally debonded areas of known location and size. Figure 11 shows three typical interferograms obtained while these panels were tested. The square-shaped defects in Fig. 11 measure 2-in., 1-1/2 in., and 3/4 in., respectively.

From these tests, it appears that the size and location of debonded areas over 1 in. in diameter can be detected with virtually 100% accuracy. Defects from 1/2 in. to 1-in. in diameter
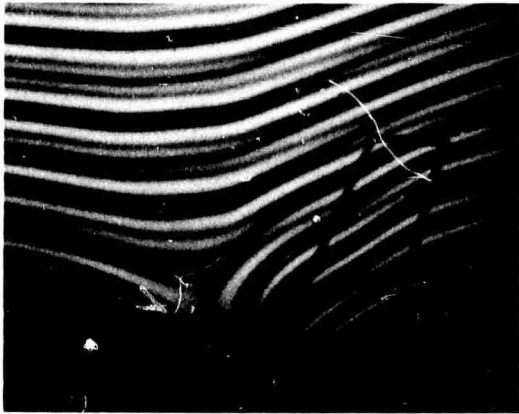
(a) Load Applied to Left of Defect

(b) Load Applied Over Defects

FIGURE 7. MULTIPLE-EXPOSURE FRINGE PATTERN NEAR DEBOND IN HONEYCOMB PANEL

FIGURE 8. VIEW OF EXPERIMENTAL
EQUIPMENT USED IN HONEYCOMB
PANEL TESTS
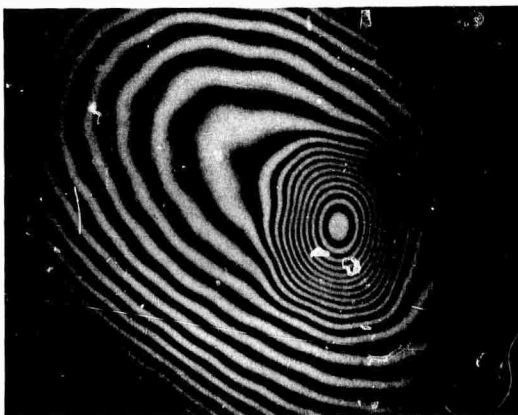
FIGURE 9. INDICATION OF DEFECT IN
PANEL WITH THE USE OF THE VACUUM
TECHNIQUE

can be detected with good accuracy, and defects of 1/2 in. or smaller (which is the order of the honeycomb cell size) appear to be about the lower limit of sensitivity with this particular system and panel.

4.3. INSPECTION OF AN AIRCRAFT TRIM TAB

4.3.1. BACKGROUND

An investigation of the use of holographic interferometry to locate defects in an aircraft trim tab of honeycomb construction was conducted. This work was carried out with the cooperation of Lt. James W. Bohlen, Air Force Materials Laboratory (MAMN), Wright-Patterson Air
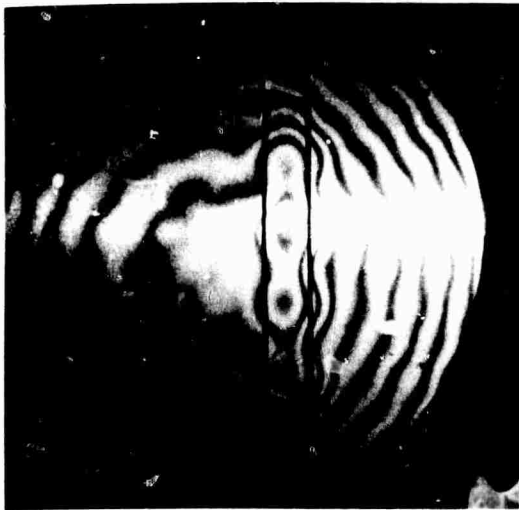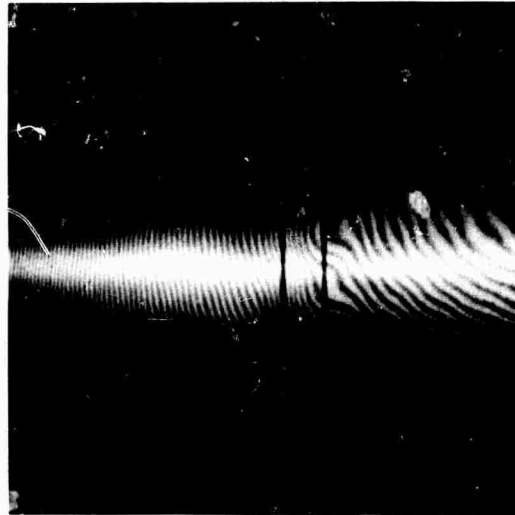
(a) 7-in. Test Window   (b) 19-in. Test Window

FIGURE 10. FRINGE ANOMALIES OVER DEFECT

Force Base, who made the aircraft component available to us. This investigation was important because it offered an opportunity to apply holography to an actual structure in which debonds are of concern and because we could later subject the aircraft component to a large variety of testing techniques and ev⌐ tually destroy it in order to locate and measure the actual flaws for comparison with the results of our tests. A quantitative comparison of the results of our holographic investigation with other techniques is reported below.

4.3.2. EXPERIMENTAL PROCEDURE AND RESULTS

The basic layout of the experimental equipment is shown in Fig. 12. This is an optical system for carrying out real-time holographic interferometry. The object is an aircraft trim tab, which is constructed by bonding a relatively thin metal skin onto an aluminum honeycomb core. The surface of the part was not specially painted or prepared for these tests.

In order to detect faulty bonds between the honeycomb core and the skin, the following procedure was used. A hologram of the test region was recorded in the usual way. With this simple setup, we were able to record holograms of about a third of the surface of the component, which was approximately 3 ft long. The plate was then developed in place. When the developed holographic plate was illuminated by the reference beam, the first diffracted order emanating from the hologram exactly reproduced the original wave pattern of the light scattered by the test area of the trim tab. When the surface of the tab was distorted, the resulting new wavefront combined with the holographically reconstructed one to form an interference pattern. The fringe

22
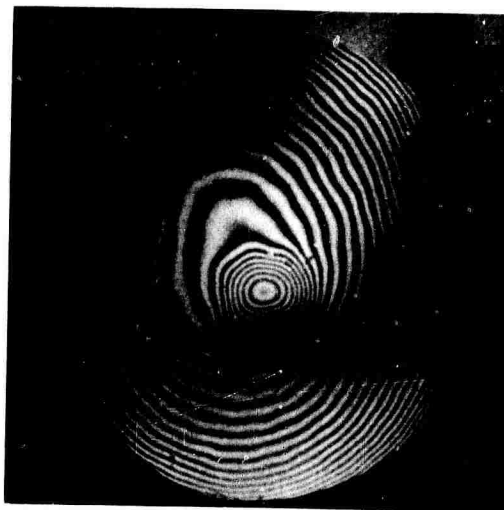
(a) 2-in. Defect

NOT REPRODUCIBLE

(b) 1 1/2-in. Defect
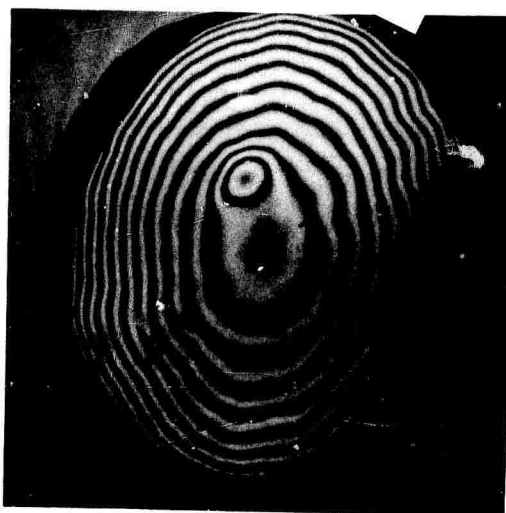
(c) 3/4-in. Defect

FIGURE 11. DEBONDED AREAS IN HARDWALL PANEL
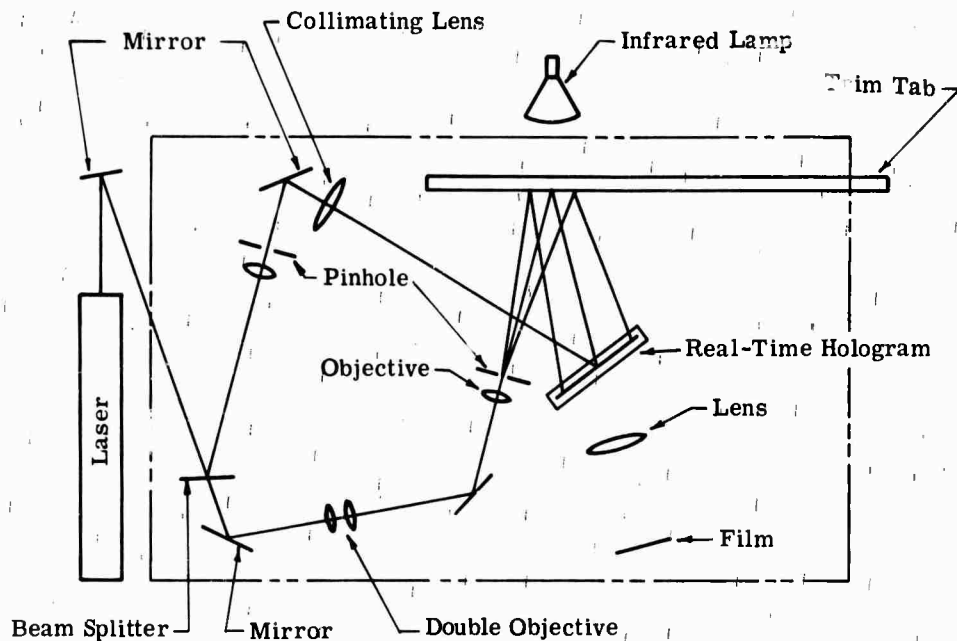
FIGURE 12. OPTICAL ARRANGEMENT FOR ALUMINUM HONEYCOMB DEFECT STUDY

location and frequency in this pattern were related to the surface displacements of the test region.

After the holographic plate was developed, the tab was irradiated from behind with a 150-W infrared lamp. The heat from the lamp was conducted to the front skin of the elevator in less than 1 sec. Since the thermal strain in the skin is related to the temperature variations in the structure, subsurface defects can be detected if they sufficiently perturb the temperature distribution on or near the surface.

The fringe anomalies resulting from the presence of defects were found to be most apparent while the skin of the trim tab was transiently conducting heat in the lateral directions. During this time, the pattern consisted of a growing set of approximately circular fringes spreading radially from the center of the heated region. As a given fringe reached the vicinity of a defect, it became locally wavy, sometimes forming a closed loop around the defective area. Figure 13 shows such an anomalous pattern near a large defect in a honeycomb panel used to check the procedure prior to testing the elevator itself. Apparently, the outermost rings show the approximate outline of a debond.

Figures 14, 15, and 16 show defects in the aircraft trim tab. Figure 14 shows defects 29 and 30; Figure 15 shows defects 18, 19, 20, 21, 23, 25, and 31; Figure 16 is the same as Figure 15 except that the defects are outlined. The defects are identified with numbers in Fig. 17 and in Tables 2 and 3. The fringe anomalies in the photographs are not nearly so pronounced as they

FIGURE 13. LOCATION OF A DEBOND
IN A HONEYCOMB PANEL

FIGURE 14. LOCATION OF DEFECTS
29 AND 30

FIGURE 15. LOCATION OF DEFECTS
IN A REGION OF THE TRIM TAB

FIGURE 16. OUTLINE OF DEFECTS IN
FIGURE 15

appeared when they were viewed directly by the eye. Tables 2 and 3 and Figure 17a indicate the position and size of the suspected defect locations as determined by holographic interferometry.

Lt. James W. Bohlen (MAMN) later supplied us with data which made possible an evaluation of these experimental results. These data and the evaluation are summarized here.

The trim tab was nondestructively inspected by ultrasonic and radiographic techniques, as well as by holographic interferometry. Following these inspections, the skin was peeled away from the honeycomb core, and the positions of core debonds were noted. Two large intentional defects had been manufactured into the trim tab; in addition, 22 unknown unintentional defects were revealed when the skin was removed. The holographic technique located 20 of the 24 defects:

25

TABLE 2. POSITION AND ESTIMATED SIZE OF SUSPECTED
DEFECTS (SIDE 1)

Defect	x Coordinate to Center of Defect	y Coordinate to Center of Defect	Approximate Diameter to Nearest 0.25 in.	Remarks
1	8.5	3.25	0.25	*
2	9.5	4.75	0.25	*
3	10.5	7.0	0.5	*
4	11.5	1.0	0.5	
5	2.25	2.5	0.25	
6	13.5	5.5	0.5	
7	15.25	7.0	0.25	*
8	15.5	6.25	0.25	*
9	16.25	4.5	0.25	*
10	16.0	1.0	1.0	
11	16.25	3.0	0.25	*
12	16.50	3.25	0.25	*
13	17.75	5.5	0.50	
14	17.75	6.75	0.50	
15	19.0	6.5	0.25	*
16	19.5	5.25	0.25	*
17	20.0	2.25	1.0	Elliptical
18	21.5	1.25	1.0	Elliptical
19	22.0	3.5	0.25	*
20	22.75	2.75	0.25	*
21	23.0	1.0	0.25	
22	24.5	1.0	0.50	
23	23.75	4.25	0.50	
24	25.0	3.75	0.75	
25	24.0	4.5	0.25	*
26	26.5	4.5	0.75	
27	27.75	2.75	0.75	
28	29.0	3.5	1.5	Kidney-shaped
29	30.0	5.0	2.0	Elliptical Max: 2.75 Min: 1.50 (Largest Defect)
30	32.25	4.5	0.50	
31	22.5	0.25	0.75	

*These defects were not as pronounced during the tests as the others. Without past experience, it is impossible to determine whether these are debond defects, defects in the honeycomb structure, defects in the skin material, or false indications.
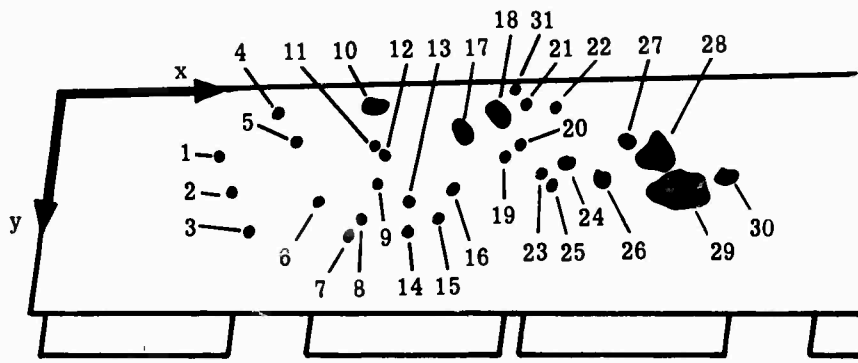
(a) Side 1
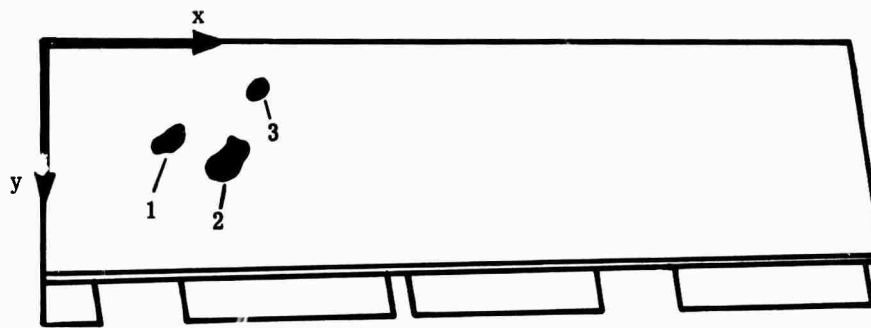
(b) Side 2

FIGURE 17. CODE FOR DEFECT LOCATIONS

TABLE 3. POSITION AND ESTIMATED SIZE OF SUSPECTED
DEFECTS (SIDE 2)

Defect	x Coordinate to Center of Defect	y Coordinate to Center of Defect	Approximate Diameter to Nearest 0.25 in.	Remarks
1	5.5	5.0	0.25	*
2	7.75	5.0	0.25	*
3	8.0	2.0	1.0	**

*These defects were not as pronounced during the tests as the others. Without past experience, it is impossible to determine whether these are debond defects, defects in the honeycomb structure, defects in the skin material, or false indications.

**This defect is opposite the largest defect on side 1 (i.e., defect 29); this indication may be an image of 29 and not a defect.

however, some false indications were also present in the holographic data. The overall effectiveness of the holographic technique was comparable to that of the ultrasonic and radiographic techniques which we also used. In a sense, the techniques were complementary; i.e., one technique found the defects missed by others and vice versa.

In Table 2, we indicated 31 suspected defects. Of these, 13 were reported as possible false indications, since the corresponding fringe perturbatic s were quite subtle. Figure 18 and Table 4 permit comparison of our results with the actual location of suspected defects. Figure 18a shows the location of suspected defects as indicated by holographic interferometry. Figure 18b shows the location of the actual bond defects. The key to these figures is presented in Table 4.

The holographic technique of locating bond defects in an actual aircraft component appears to give results comparable to those produced by ultrasonic and radiographic techniques. The main problem arose in evaluation of the more subtle fringe perturbations which were initially suspected of being false indications. Had these been ignored, 16 of the 24 defects would have been correctly located and 4 false indications would have resulted. Of the 13 subtle perturbations originally suspected of being false, 9 were in fact false. It is likely that if further investigations were carried out and if equipment were designed for testing a particular component, the method could be enhanced to improve the certainty of defect detection.

4.4. SUMMARY

The use of holographic interferometry to detect areas of debond in honeycomb sandwich structures was investigated. Two sponsor-supplied specimens were tested: (1) aluminum-skin, paper-core panels used in constructing portable hardwall structures, and (2) a composite-skin, aluminum-core, aircraft trim tab. Different techniques were developed for these two applications. The use of holographic interferometry was shown to provide clear and accurate indications of debonds of areas greater than the cell size of the core in testing of the hardwall panels. The slightly more difficult procedure for testing the trim tab produced indications of debond areas with a certainty comparable to ultrasonic scanning methods.

5
MONITORING OF STRESS-CORROSION CRACKING

5.1. INTRODUCTION

Many metals are susceptible to the formation and propagation of cracks when they are placed in certain environments, even though they may be statically stressed below the yield point. Holographic interferometry makes possible the early detection of such cracking processes if they are manifested by alteration of the field-of-surface displacement of the test specimen. The concept involved is similar to that of debond inspection and microcrack detection discussed

28
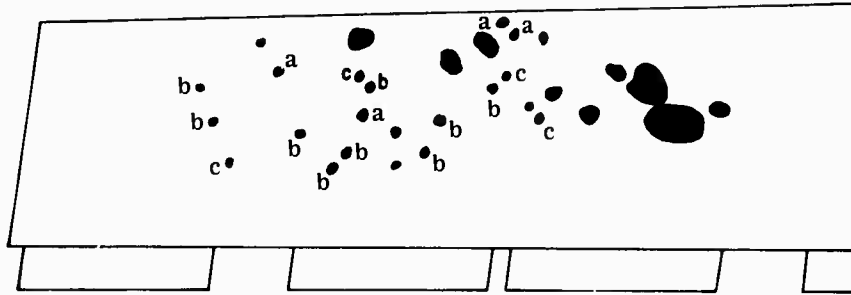
(a) Suspected Defects
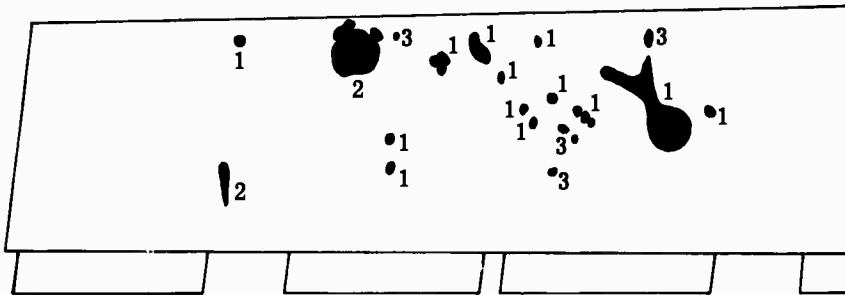
(b) Actual Defects

FIGURE 18. BOND DEFECT LOCATIONS

TABLE 4. KEY TO FIGURE 18; LOCATION OF
SUSPECTED AND ACTUAL BOND DEFECTS

Code	Significance	Total Number of This Type
a	False indication of defect	4
b	False indication of defect, but originally suspected to be false	9
c	Correct indication of defect, but originally suspected to be false	4
1	Properly located defect	18
2	Properly located defect, but misjudgment of size	2
3	Defect not located	4

29

in previous sections. In this case, however, the observed surface displacement is directly caused by the cracking process—no externally applied differential load is utilized. Real-time holographic interferometry offers two particular advantages for this application:

(1) Its great sensitivity makes it possible to detect or possibly to predict cracking without actual visual identification of a crack.

(2) Cracking can be continuously monitored without removing the specimen from a special test environment for inspection.

Observation of stress-corrosion cracking by holographic interferometry was suggested by R. Fitzpatrick of the Army Mechanics and Materials Research Center.

5.2. EXPERIMENTAL PROCEDURE AND RESULTS

As a prototype problem, we have observed stress-corrosion cracking of the titanium alloy Ti-6AL-4V submerged in anhydrous methanol. This problem was chosen primarily because of the rapidity of stress-corrosion cracking in this system. This alloy is also of current technical importance for use in aircraft and missile components. A brief review of the technical literature dealing with this cracking process is given in a previous report [32].

The optical arrangement for this experiment is shown in Fig. 19. As usual, the laser light is divided by a beam splitter int an object beam and a reference beam which are then expanded and filtered. A 20-mW He-Ne laser was used to record holograms on 649-F spectroscopic plates. In situ processing was used in order to avoid the realignment problems associated with removing the plate for development following the holographic exposures. The plates were mounted in a glass enclosure which could be filled with photographic chemicals. This plate holder (sometimes refer.ed to as a liquid gate) was filled with water in which the plate was submerged for 5 min prior to exposure; soaking the plate effectively sensitizes it and thereby reduces the required exposure time by a factor of approximately 5. After the plate is developed, the holder is again filled with water, and the hologram can be viewed immediately. This procedure avoids problems of emulsion distortion associated with drying.

The test specimen was a small (2-in. by 7/8-in.) flat, 0.10-in.-thick notched coupon of titanium alloy. It was loaded in three-point bending in a simple fixture until the nominal stress approached the yield stress. A hologram was recorded, and the specimen was observed by real-time interferometry. If relaxation occurred, it was indicated by formation of interferometric fringes. When this fringe pattern became stationary, relaxation was concluded, and the stress-corrosion-cracking tests were begun.

The loaded specimen was placed into a glass tank which was then filled with anhydrous, reagent-grade methanol and sealed to avoid water vapor contamination, which is known to suppress the corrosion-cracking process. A hologram was then recorded and developed in place. When

30
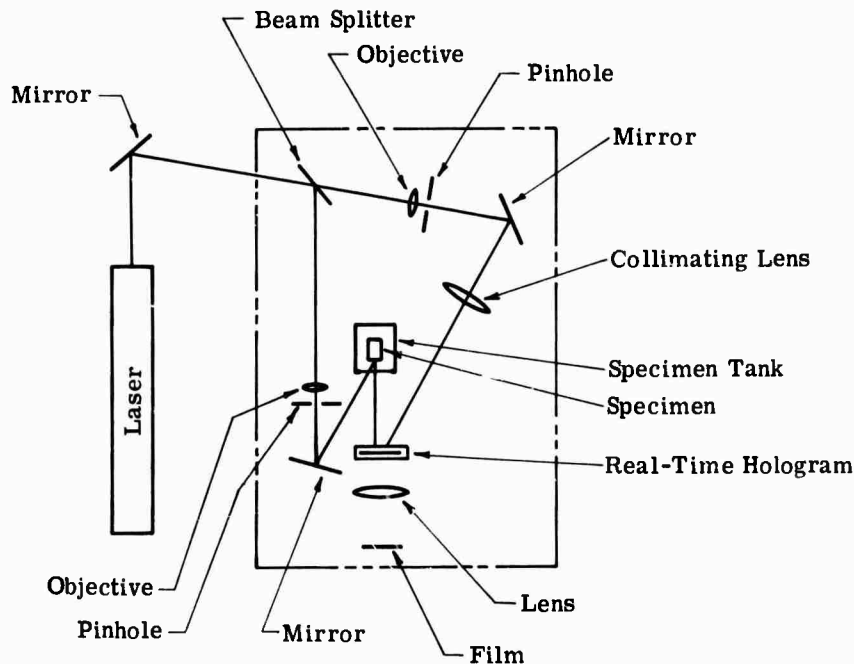
FIGURE 19. OPTICAL ARRANGEMENT FOR STRESS-CORROSION
STUDIES

the illuminated specimen and reconstructed hologram were viewed simultaneously, a fringe pattern which changed with time was observed to be superimposed on the specimen. This pattern, which was indicative of the stress-corrosion-cracking process, was photographed at various times during the test. The tank and specimen, along with the in situ development plate holder are shown in Fig. 20.

Figures 21 through 27 are photographs of fringe patterns taken at various times during the test. The specimen was first nominally stressed to approximately the yield point. Holographic interferometry was then used to check for stress relaxation before the specimen was subjected to methanol. Figure 21 shows a typical interference pattern which indicates the surface displacement produced as the specimen relaxes, i.e., that the entire surface is fairly uniformly affected. This pattern should be contrasted with those discussed below. After this fringe pattern ceased to change with time, the stress-corrosion-cracking test itself was begun.

Figures 22 through 26 show the fringe patterns observed at various stages of crack initiation and propagation in a specimen (t = time). In this particular experiment, very little activity was observed until several hours after the specimen was submerged in methanol. The hologram used to produce these fringes was recorded 9 hr after the specimen was first exposed to the methanol. Figure 22 shows an early indication of stress-corrosion activity. Note that the deformation is obviously initiated at the notch on the left side. This is presumably an early indication that

31
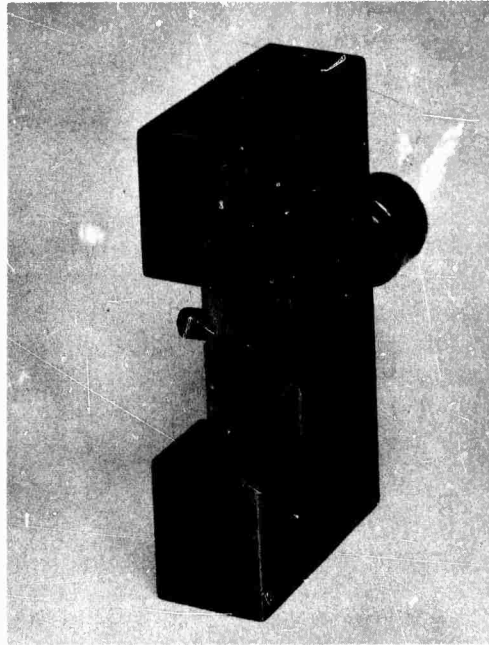
(a) Test Specimen and Loading Fixture

NOT REPRODUCIBLE
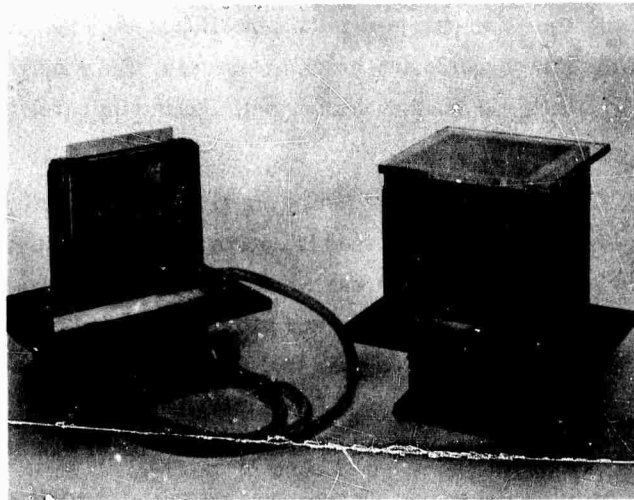
(b) Real-Time Plate Holder and Specimen Tank

FIGURE 20. TEST EQUIPMENT

FIGURE 22. FRINGE PATTERN, t = 9.1 hr

NOT REPRODUCIBLE
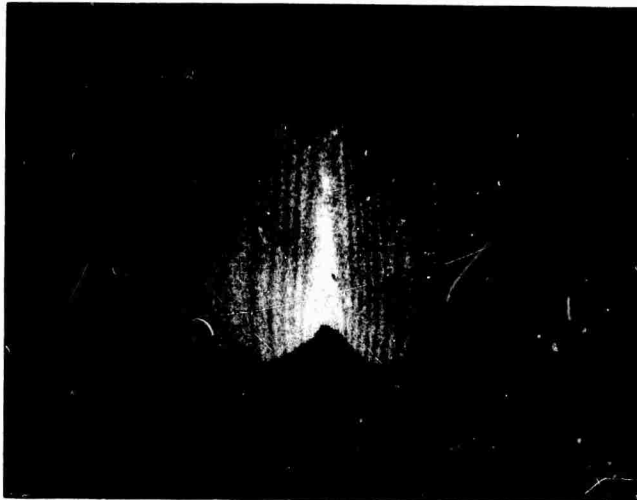
FIGURE 21. STRESS-RELAXATION FRINGES

33
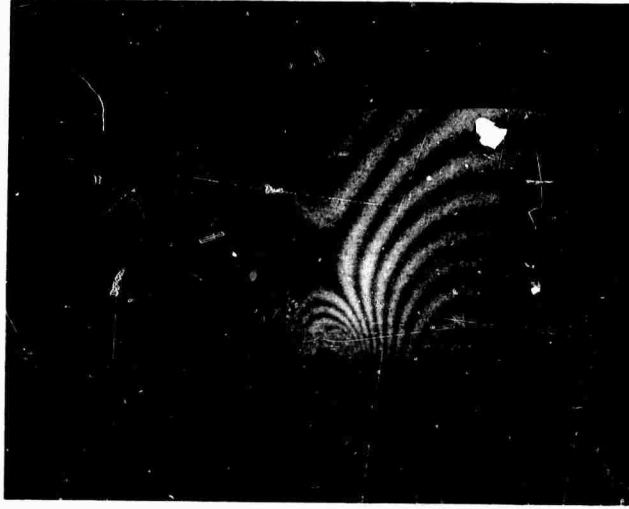
FIGURE 24. FRINGE PATTERN, t = 11.8 hr

NOT REPRODUCIBLE
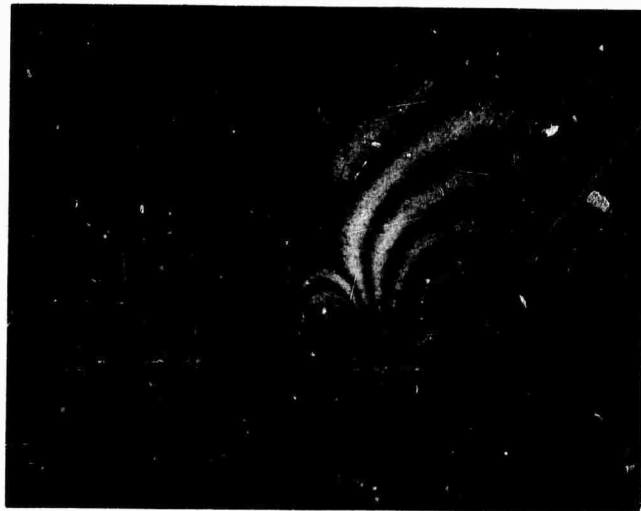
FIGURE 23. FRINGE PATTERN, t = 10.8 hr
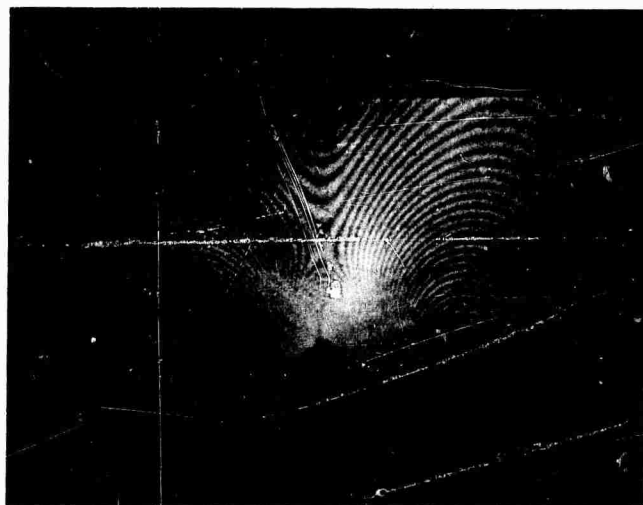
FIGURE 26. FRINGE PATTERN, t – 16.8 hr

NOT REPRODUCIBLE
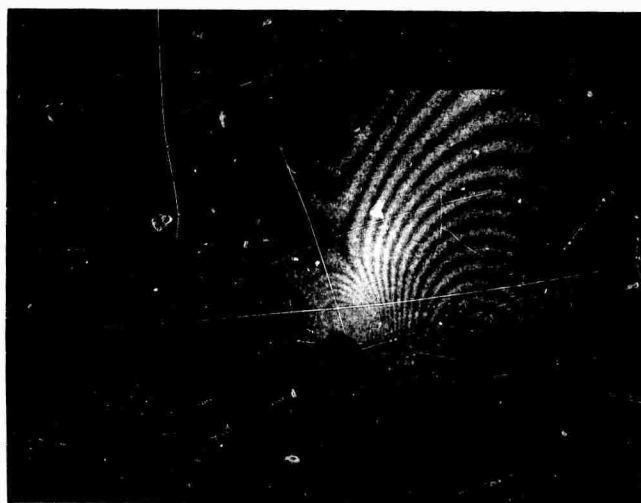
FIGURE 25. FRINGE PATTERN, t = 13.8 hr
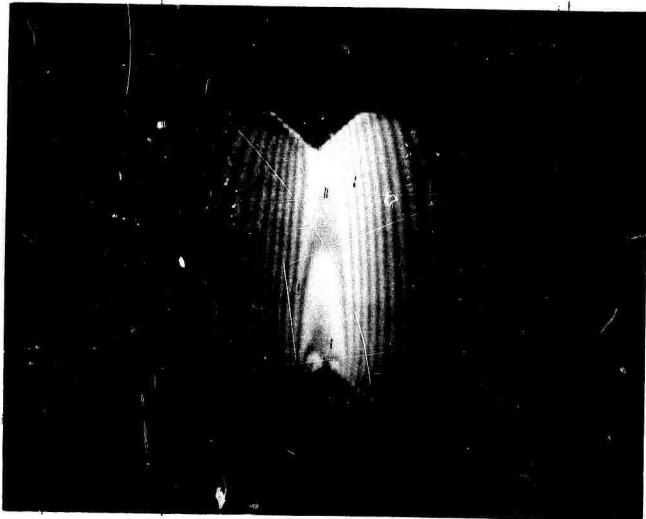
FIGURE 27. STRESS RELAXATION WITH CORROSION-CRACKING FRINGES

stress corrosion is occurring in that region of stress concentration. In other tests, this initiation occurred near the other notch or simultaneously near both notches.

The next four figures show the progressive change in the fringe pattern as the stress-corrosion-cracking process proceeds. Only in the last two figures are cracks clearly visible to the unaided eye. It may also be noted that the fringes in these last figures were too fine to be readily photographed with a simple camera.

In the experiment described above, we were careful to separate the effects of stress relaxation and stress-corrosion cracking. If relaxation is not so great as to produce extremely fine fringes, this separation is not necessary, although it is clearly desirable. Figure 27 is a typical fringe pattern produced when the loaded specimen is immediately submerged in methanol before stress relaxation occurs. This pattern is a clear indication of simultaneous stress relaxation and stress-corrosion crack initiation. Note that in this figure, corrosion cracking appears to be initiated near both notches. This specimen did, in fact, eventually crack on both sides.

No effort was made to evaluate precisely the surface displacements indicated by the fringe patterns; they are considered as qualitative visualizations of the progress of stress-corrosion cracking. Basically, however, the fringes are lines of constant surface displacement relative to the surface configuration when the hologram was recorded. For the particular experiment described above, each fringe represents a displacement of roughly 0.3 μm.

5.3. CONCLUSIONS

The results reported in the previous section indicate that holographic interferometry can be used to monitor delayed cracking phenomena such as stress-corrosion cracking. In a sense, the variation of interferometric fringes with time indicates the degree of stress-corrosion attack as a function of time. The probable region of crack initiation can be located before an observable macroscopic crack appears. The method, therefore, may well prove to be useful in studying the susceptibility of materials to delayed cracking before actual failure of the material.

There are, however, certain limitations which should be noted. First, the mechanical stability requirements inherent in real-time holographic interferometry discussed earlier must be satisfied. Second, the environment of the specimen must be transparent to laser light, so that the object may be observed, and it must remain at constant temperature to avoid extraneous fringes. Finally, gross corrosion of the surface cannot occur. If it does, the optical correlation between the hologram and the surface will be lost, and meaningful interferometric fringes will not be produced.

5.4. SUMMARY

A technique was developed for real-time monitoring of stress-corrosion cracking in laboratory specimens of materials. Because the method provides an indication of corrosion-cracking

activity prior to formation of a visible crack, it can speed up tests for susceptibility of materials to cracking. The method is not applicable when gross degradation of the surface occurs because of corrosion or when the specimen must be placed in an opaque environment.

6
INTERFEROMETRY OF THREE-DIMENSIONAL TRANSPARENT OBJECTS

6.1. INTRODUCTION

Preceding sections have dealt with the application of holographic interferometry in which the object surface is opaque and diffusely reflecting. Holographic interferometry can also be used to study transparent objects and is therefore a potentially powerful tool for studying three-dimensional strain fields in transparent models and for detecting nonhomogeneities and flaws in glass and other transparent materials. The present understanding of holographic interferometry and its application to the study of three-dimensional transparent objects is generally not as far advanced as for diffusely reflecting objects. In this section, we report the development of a number of basic techniques for the study of transparent objects which we hope will be of long-range usefulness in material testing and stress-analysis applications.

6.2. BASIC EXPERIMENTAL CONFIGURATION

The basic apparatus used to record holograms of transparent objects (also referred to as phase objects) is shown in Fig. 28. The laser light is divided into two beams which are then individually expanded, filtered, and collimated. As previously described, the hologram is the recorded interference pattern of these two beams as they intersect each other in the plane of a photographic plate. The transparent object under study is placed in the test section as indicated in Fig. 28. A hologram is then recorded on the same photographic plate after the object has been stressed, heated, or displaced. When the developed hologram is exposed to the reference beam, the wavefronts which emanated from the object in its initial state and from the object after it had been perturbed will be reconstructed simultaneously and will interfere with each other. The resulting interference pattern is indicative of phase differences introduced by the change in the condition of the object between exposures.

There are four primary factors which lead to the phase changes indicated by the interference pattern:

(1) Index of refraction variations caused by local compression or dilation in the object

(2) Distortion of the overall dimensions of the object

(3) Birefringence effects (if polarizing elements are introduced into the optical system)

(4) Displacement of the entire object
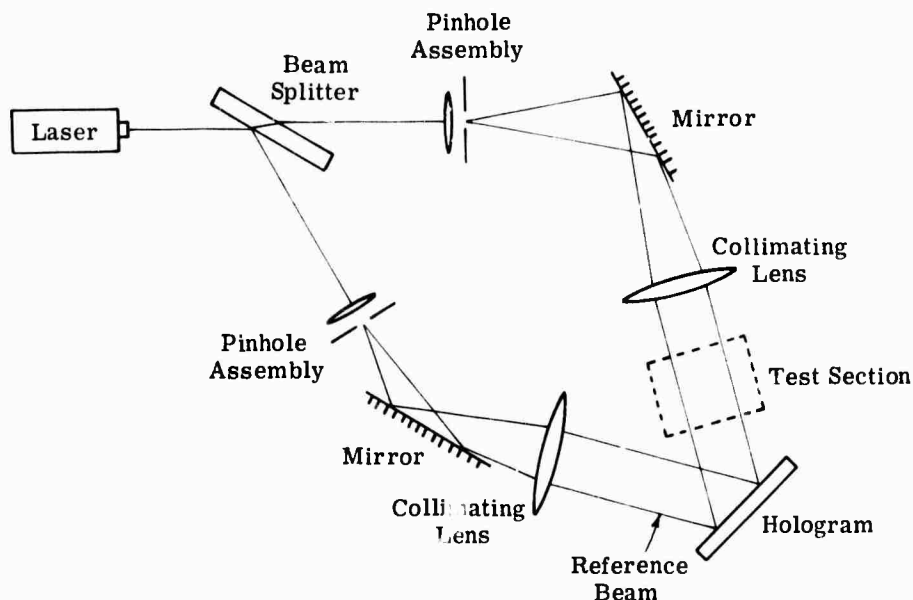
FIGURE 28. EXPERIMENTAL SETUP FOR TRANSPARENT OBJECTS

If the apparatus shown in Fig. 28 is used, the fringes will not be localized; i.e., they may be viewed by placing a viewing screen, or photographic film, in the reconstructing object beam at any arbitrary distance from the hologram. (Of course, appropriate focusing is required for high clarity and resolution.) In the tests reported here, this system was modified by placing a diffusing screen (ground or opal glass) between the collimating lens and the test section. When a holographic interferogram produced with such diffuse illumination is viewed, the fringes appear to be localized at a certain position in space. Furthermore, this surface of localization and the fringe pattern itself change as the viewing angle is varied. The reason for this is discussed furthe · in Appendix I. It should be noted, however, that localization provides additional information about three-dimensional structures which cannot be obtained by classical interferometry.

The investigations reported below deal only with interference caused by changes of refractive index. Birefringence effects are discussed briefly in a previous report [33]. More detailed information regarding holographic photoelasticity for stress analysis may be found in Refs. [34] through [39].

6.3. MULTIDIRECTIONAL ILLUMINATION

6.3.1. BACKGROUND

This information about a transparent object, which is derived from a holographic interferogram, is strongly dependent on the nature of the wavefront used to illuminate the object. Most

research to the present has dealt with either plane-wave illumination or diffuse illumination. In plane-wave illumination, holographic interferometry is basically an analog of classical interferometry such as that done with a Mach-Zehnder interferometer. The primary difference is that holography allows comparison of the object at two different points in time. In addition, the interfering wavefronts are recorded and can be reconstructed, at will, for examination and processing by other techniques such as by the Schlieren method. It also has the practical advantage of being a true, single-path interferometer; therefore, the effects of refraction, e.g., in test section windows, within the system are minimized.

Diffuse illumination of transparent objects is used to take advantage of the three-dimensional nature of holography. Specifically, an interferogram produced with diffuse illumination can be viewed from an arbitrary direction compatible with the aperture of the hologram. Although the observed fringe field represents the integration of the refractive-index field over the entire optical path, the ability to view the interferogram from an arbitrary direction along with the phenomenon of fringe localization enable one to visualize the three-dimensional field qualitatively. Although such interferograms are pleasing to view, if one tries to photograph the fringes or to resolve fine fringes, they prove to be rather unsatisfactory because of the problems associated with fringe localization and laser speckle. The phenomenon of fringe localization is described briefly in Appendix I, which demonstrates that when a diffusely illuminated transparent object is perturbed, by mechanical loading, for example, the resulting holographic interferogram shows the fringes to be localized in some surface in the vicinity of the object. As the viewing angle is varied, both the fringe pattern and the surface of fringe localization are observed to change.

In the general case of a large, unsymmetrical, refractive-index distribution, the surface of apparent fringe localization may be quite complicated. The corresponding depth of field required to photograph the fringes necessitates the use of a small aperture in the viewing system. Such an aperture, however, cuts off the high-spatial-frequency content of the object illumination, thus producing laser speckle and reducing the signal-to-noise ratio. The use of a small aperture is detrimental, since the visibility of the interferometric fringes rapidly decreases as the number of fringes per unit of length approaches the number of speckles per unit of length.

The problem of fringe clarity has been considered in some detail by Tanner [40, 41]. Utilizing Goldfischer's [42] model for laser speckle, he redefines fringe visibility in order to characterize interferometric fringes in the presence of speckle. This definition is applied to holographic interferometry with a diffuse light source, and optimum viewing aperture size is determined according to a rather involved set of criteria. As an example, he shows that for a typical object with an axial dimension of 10 cm, sufficient fringe clarity would be obtained only for optical path changes not exceeding about 1 fringe/mm. In most applications, this degree of clarity would be unacceptable, since it limits the magnitude of change in refractive index which can be studied.

40

The problem with laser speckle can be overcome if one is willing to view the interferogram from a number of discrete viewing angles rather than from completely arbitrary directions. This procedure is reasonable, since techniques for approximately determining three-dimensional, refractive-index distributions will, no doubt, involve the use of fringe patterns obtained from a finite number of viewing directions. Tanner [40] has suggested that the object be illuminated by several plane waves originating from an array of point sources behind the collimating lens. If one considers the lenses and spatial filters required to obtain point sources of sufficient quality, this system is somewhat impractical, especially if one wishes to construct a square array of point sources. We propose a simple practical method for recording holographic interferograms which can be viewed from several discrete directions. This method involves the placement of an appropriate phase grating in the object beam coupled with simple spatial filtering of the output.

6.3.2. EXPERIMENTAL METHOD AND RESULTS

The usual arrangement for recording a holographic interferogram of a transparent object with diffuse illumination is shown in Fig. 29. In the technique which we propose, the diffusing screen shown in Fig. 29 is replaced by a grating. In our experiments, the results of which are discussed below, a sinusoidal phase grating of frequency f and square aperture of dimension ℓ was used. When such a grating is illuminated by a plane wave of unit amplitude, the field immediately to the right of the grating is given by

$$u(x, y) = \left(\text{rect } \frac{x}{\ell} \text{ rect } \frac{y}{\ell}\right) \sum_{\nu=-\infty}^{\infty} J_\nu\left(\frac{m}{2}\right) \exp\left(i2\pi\nu f x\right) \tag{6}$$

where m is the peak-to-peak phase delay, J_ν is the Bessel function of the first kind of order ν, f is the spatial frequency, and rect (x) is unity for $|x| \leq 1/2$ and zero otherwise. This expression is derived in Ref. [43], p. 69. Hence, the energy of the incident wave is deflected into a number of component plane waves propagating at angles of approximately $\pm n f \lambda$ with respect to normal. By adjustment of the parameters m and f, a grating can be designed to yield an appropriate spectrum for a given application.

The hologram is recorded with the system shown in Fig. 30. If the double-exposure method is used, we obtain the interferogram upon reconstructing the hologram by illuminating it with the reference beam. As shown in Fig. 30, the output of the hologram is then Fourier-transformed by a spherical lens. We can then obtain the interference pattern for each discrete viewing angle by sampling only the neighborhood of a single spectral component in the transform plane. The corresponding portion of the reconstruction can then be imaged or processed in any desired manner, and it has all the properties associated with an interferogram produced with a single, collimated object beam.
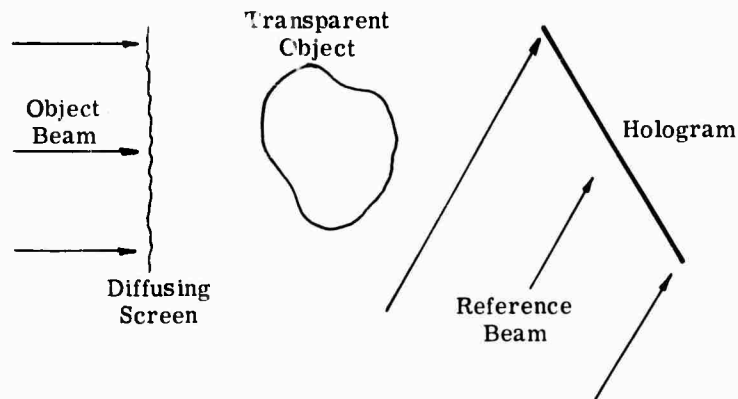
FIGURE 29. SYSTEM FOR INTERFEROMETRY WITH DIFFUSE
ILLUMINATION
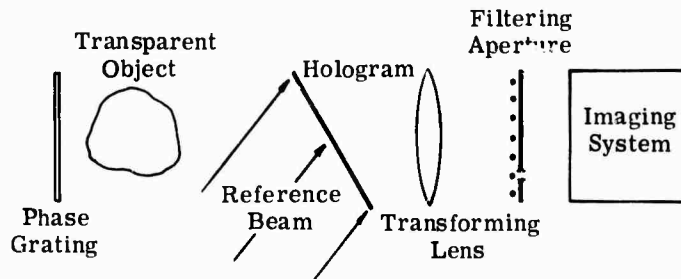
FIGURE 30. SYSTEM FOR INTERFEROMETRY WITH DISCRETE
VIEWING ANGLES

To illustrate the application of this technique, we used, for simplicity and ease of reproduc-
ibility, the field of refractive-index change caused by the natural convection above a heated
horizontal wire immersed in water. The electrically heated wire was 0.25 mm in diameter and
7.3 cm long. We were able to resolve interferometric fringes of frequency greater than 20 lines/
mm, which allows us to observe considerably greater phase shifts than would be possible with
diffuse illumination.

Figure 31 shows three different interferograms of essentially identical fields. The inter-
ference pattern in 31a was produced holographically with the use of a single, collimated object
beam. The pattern in 31b was produced by the use of a phase grating in the object beam; it is of
essentially the same quality as that in 31a except for some slight degradation traceable to
imperfections in the grating. The fringe pattern in 31c was produced with the use of a diffuser,
a plate of fine-structured opal glass, in the object beam. The aperture of the hologram was
carefully adjusted to optimize fringe clarity. Only about 5 lines/mm could be resolved. This
resolution is in essential agreement with Tanner's analysis [41].

42
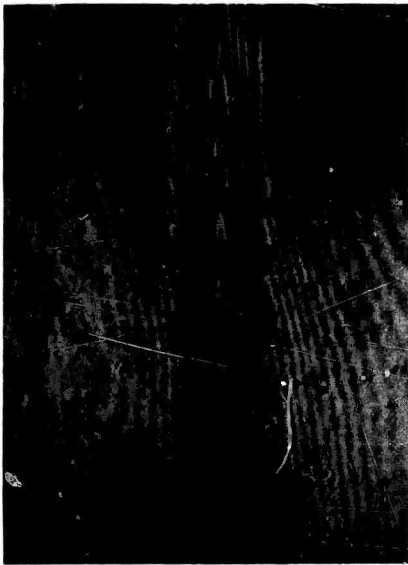
(a) Plane-Wave Illumination

(b) Single Component of Grating Illumination
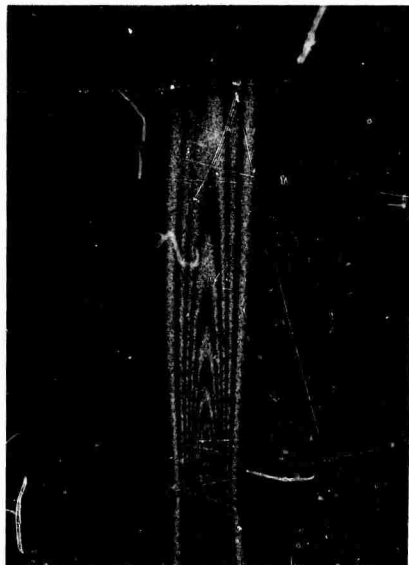
(c) Diffuse Illumination

FIGURE 31. COMPARISON OF FRINGE CLARITY OBTAINED WITH VARIOUS TYPES OF OBJECT ILLUMINATION

43

Figure 32 shows two different views obtained from a single holographic interferogram produced with the use of the phase grating. This figure clearly indicates that the method is capable of generating high-clarity fringe patterns for a variety of viewing angles.

We obtained the results of Fig. 32 by using a grating of frequency f = 50 lines/mm. This grating frequency afforded an effective variation of viewing angle of about 10.8°, which we could increase if we desired by increasing the grating frequency or by adjusting the peak-to-peak phase delay to diffract more energy into higher-order spatial components. We also carried out experiments using crossed phase gratings like those described by Leith and Upatnieks [44]. The use of crossed phase gratings yields component plane waves equivalent to those derived from a square array of point sources. The viewing angle could then be varied about both the vertical and horizontal axes.

6.3.3. CONCLUSIONS

We have demonstrated a practical technique for producing multidirectional holographic interferograms which are free of laser speckle. The fringe patterns corresponding to each discrete viewing direction are of a quality normally associated with interferograms produced with a single, plane object wave. The use of structured wavefronts for object illumination may prove to have other interesting applications in the field of holographic interferometry.

6.4. DETERMINATION OF THREE-DIMENSIONAL, REFRACTIVE-INDEX FIELDS

Classical interferometry has been limited to the study of two-dimensional (or axisymmetric) phase objects. The increased information content of holographic interferograms recorded with multidirectional illumination makes possible the approximate determination of three-dimensional, refractive-index fields. A technique for determining such three-dimensional fields with interferometric data must be developed before holographic interferometry can be used to locate accurately flaws or nonhomogeneities in transparent media. This section presents a technique which we have developed for this purpose. The analysis and examples given here are of a preliminary nature, but they seem to be a promising approach to this problem.

6.4.1. BACKGROUND

Although the determination of three-dimensional, refractive-index fields by holographic interferometry is of potential importance in several technological applications, it has received relatively little attention. Matulka and Collins [45] have recently accomplished such a determination. The phase object in their experiments was a free air jet. Their analysis technique is based on earlier work by Maldonado, Olson, and colleagues [46, 47, 48, 49] on plasma emissions. The required inversion of the governing integral equation (which is discussed in the following section) is achieved by expanding the unknown function (the refractive-index field) in a generalized

(b)

(a)
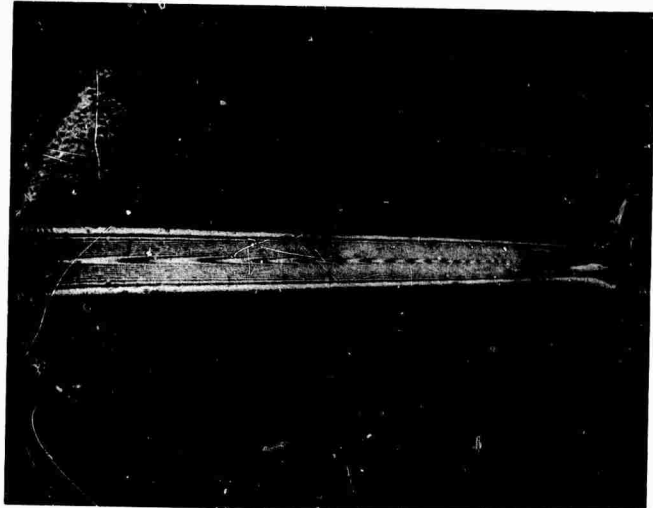
FIGURE 32. TWO VIEWS OF THE INTERFERENCE PATTERN PRODUCED WITH A PHASE GRATING IN THE OBJECT BEAM. The two views are separated by an angle of 10.8°.
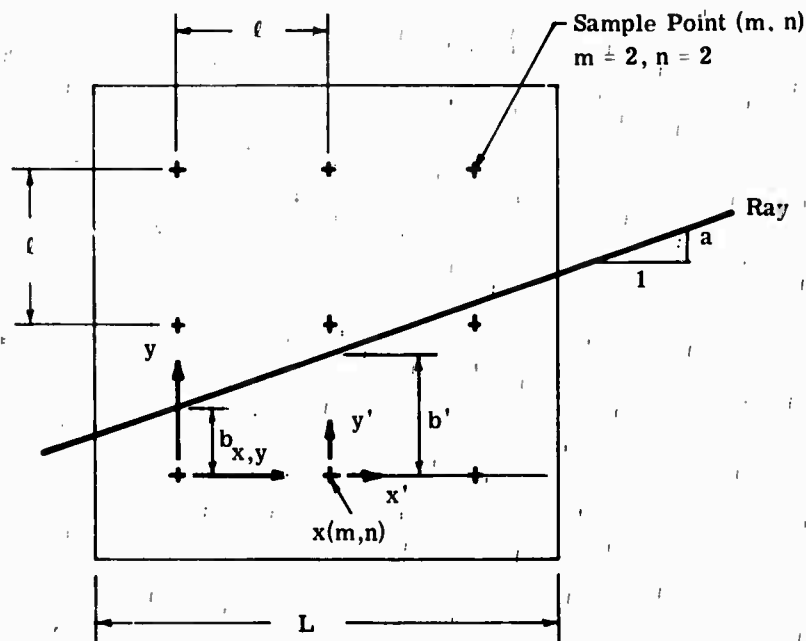
FIGURE 33. NOMENCLATURE AND COORDINATE SYSTEM

Fourier series. The coefficients of this rather complicated, two-dimensional expansion are determined by substitution of the series into the governing integral equation, the nonhomogeneous part of which is determined from the interferometric data. This inversion technique was shown to be capable of generating quite accurate results, although convergence was not always rapid (1700 terms in the case of an axisymmetric distribution with a severe discontinuity). One practical drawback is that, in the absence of symmetry, data must be obtained over a 180° range of viewing angle in order to carry out the necessary orthogonalization. Another limitation, although a minor one, is that the phase object under study must be represented in a circular region outside of which it vanishes.

Rowley [50] derived an expression for the two-dimensional Fourier transform of the unknown refractive-index field in terms of interferometric data. A knowledge of the optical path of all rays passing through the object over a 180° range is required. If this method were applied on an approximate basis with the use of discrete data, it would be found that the transform is heavily sampled near the origin and sparsely sampled away from it, which might make direct application of Rowley's method to experimental data difficult.

Berry and Gibbs [51] independently used an approach similar to that of Rowley for an analogous problem in x-ray shadowgraph interpretation. They carried the analysis further than Rowley by formally taking the inverse transform to obtain an explicit expression for the refractive-index distribution. This expression, an integral, has a rather troublesome singularity. Tanner [52],

however, has presented an alternative form which avoids this difficulty; his method also requires data over a 180° range, although he indicates that a smaller range will yield a good approximation if the distribution is sufficiently elongated.

Pal [53] has also derived the same result as Berry and Gibbs; however, he uses a scheme for avoiding the singularity problem, which is much more cumbersome than that used by Tanner [52]. Reference [53] also includes a discussion of a discrete-element technique in which the phase object is considered to be divided into N grid elements, each of which has a constant refractive index. The governing equation is replaced by a system of N simultaneous linear equations in N unknowns. This technique was found to be extremely sensitive to factors such as mesh size. Although little detail regarding this finite element approach is presented, it was apparently not satisfactory. In the following section, we discuss a promising alternative to these techniques.

6.4.2. ANALYSIS

Suppose that a holographic interferogram of a transparent object is recorded and that either diffuse or multidirectional plane-wave illumination is used, as discussed above. An initial exposure is recorded in the usual manner. The object is then perturbed, and a second exposure is recorded. The resulting interferogram can then be viewed from several different directions. In a given viewing direction, the fringe pattern enables one to determine the difference in optical path length of the rays passing through the object before and after it was perturbed. This differential optical path, denoted by ϕ_i, where the subscript i identifies a particular ray, is given by

$$\phi_i = \int_{S_i} \Delta n(x, y, z) \, dS_i \tag{7}$$

where Δn is the change in refractive index between exposures and dS_i is the differential distance along the ray. The integral is evaluated along the path of the ray, which is assumed to be a straight line. The problem then becomes one of inverting this integral equation to solve for Δn when the ϕ_i are given. To accomplish this on an approximate basis, a particular plane, z = constant, in the object is selected for study and is considered to be overlaid with a number of discrete points (see Fig. 33). On the basis of sampling theory (see e.g., Ref. 43), we can represent the unknown distribution as

$$\Delta n(x, y) = \sum_{m=1, 2, \ldots}^{S} \sum_{n=1, 2, \ldots}^{S} \Delta n' \left[\frac{L}{S}(m), \frac{L}{S}(n) \right]$$

$$\mathrm{sinc} \left[\frac{S}{L} \left(x - \frac{L}{S}m \right) \right] \mathrm{sinc} \left[\frac{S}{L} \left(y - \frac{L}{S}n \right) \right] \tag{8}$$

47

where the $\Delta n'$ are the values of Δn at the discrete points given by the coordinates $\left[\frac{L}{S}(m), \frac{L}{S}(n)\right]$, and S^2 is the number of sampling points. The sinc function is defined by sinc $x \equiv (\sin \pi x)/\pi x$. Such a representation is exact if Δn has a two-dimensional Fourier transform of finite extent (i.e., if it is band-limited) and if the sampling intervals L/S are properly chosen. In our case, although this condition is not met exactly, we should be able to give an accurate approximation if the distribution does not contain severe discontinuities in magnitude or slope. When the series (8) is substituted into the integral equation (7), it becomes

$$\int_{S_i} \sum_{m=1}^{S} \sum_{n=1}^{S} \Delta n'(\ell m, \ell n) \, \text{sinc}\left(\frac{x - \ell m}{\ell}\right) \, \text{sinc}\left(\frac{y - \ell n}{\ell}\right) dS_i = \phi_i \tag{9}$$

where $\ell = L/S$ is the grid spacing and m and n are integers. The S^2 values of $\Delta n'$ are now the unknown discrete variable. For convenience, let

$$x' = x - \ell m \quad y' = y = \ell n \tag{10}$$

Assuming that the order for summation and integration can be interchanged, we obtain

$$\sum_{m=1}^{S} \sum_{n=1}^{S} \Delta n'(\ell m, \ell n) \int_{S_i} \text{sinc}\left(\frac{x'}{\ell}\right) \, \text{sinc}\left(\frac{y'}{\ell}\right) dS_i = \phi_2' \tag{11}$$

The rays, which are assumed to be straight lines, can be represented by

$$y' = ax' + b' \tag{12}$$

Equation (11) then becomes

$$\sum_{m=1}^{S} \sum_{n=1}^{S} \Delta n'(\ell m, \ell n) \int_{-\infty}^{\infty} \text{sinc}\left(\frac{x'}{\ell}\right) \, \text{sinc}\left[\frac{(1 + a^2)^{1/2}}{\ell}(ax' + b')\right] dx' = \phi_i \tag{13}$$

In this equation, the integral extends formally to infinity, although the actual domain of interest is finite. By algebraic manipulation, this integral can be expressed as a simple convolution and evaluated to yield

$$(1 + a^2)^{1/2} \sum_{m=1}^{S} \sum_{n=1}^{S} \Delta n'(\ell m, \ell n) \, \text{sinc}\left(\frac{b'}{\ell}\right) = \phi_i \quad \text{for } |a| < 1 \text{ and } |a| \neq 0$$

$$(1 + a^2)^{1/2} \sum_{m=1}^{S} \sum_{n=1}^{S} \Delta n'(\ell m, \ell n) \, \text{sinc}\left(\frac{b'}{a\ell}\right) = \phi_i \quad \text{for } 1 < |a| \infty$$

48

$$\sum_{m=1}^{S}\sum_{n=1}^{S} \Delta n'(\ell m,\ \ell n)\ \text{sinc}\left(\frac{c_i}{\ell}\right) = \phi_i \quad \text{for } |a| = \infty$$

$$\sum_{m=1}^{S}\sum_{n=1}^{S} \Delta n'(\ell m,\ \ell n)\ \text{sinc}\left(\frac{b}{\ell}\right) = \phi_i \quad \text{for } |a| = 0 \tag{14}$$

In the equation for the case of $|a| = \infty$, the equation of the ray is $x' = c_i$. The values of the optical paths, ϕ_i, for a number, S^2, of rays could be obtained from holographic interferograms. Equation (14) would then give a set of S^2 simultaneous algebraic equations in S^2 unknowns, which could be solved for the values of n'. The series (14) would then represent the refractive-index field throughout the object plane under study.

Our method has been found to yield substantial improvement over the discrete-element technique; however, the error was still judged to be too great, basically because the set of algebraic equations tends to be ill-conditioned, particularly when the range of viewing angle is less than 180°.

In order to alleviate the problems associated with the ill-conditioned equations, we applied some recently developed numerical techniques. Although the details of these techniques are not important to the present discussion, the basic approach should be noted. An overdetermined system of equations was generated; i.e., the number of equations formed was much greater than the number of unknowns. In general, these equations are inconsistent as well as overdetermined. These equations were treated by the method of least squares; i.e., the square of the residuals was minimized. The algorithm used is based on Golub's method [54], which utilizes Householder reflections and was developed by C. B. Moler of The University of Michigan. This approach not only leads to greatly improved accuracy but also makes the recording of appropriate experimental data much more convenient. In the following section, typical results of both computer simulations and actual experimentation are presented.

6.4.3. EXPERIMENTAL AND COMPUTER SIMULATION RESULTS

In order to study the technique discussed above, we chose as a hypothetical, differential, refractive-index distribution a displaced Gaussian function

$$\Delta n(x,\ y) = a\left\{\left[\exp-\left(\frac{x - \mu_x}{\Delta_x}\right)^2 - \left(\frac{y - \mu_y}{\Delta_y}\right)^2\right]\right\} \tag{15}$$

within a unit square and zero outside it. The optical path lengths for various rays were determined by numerical evaluation of the integral for (7) for the distribution (15). These values of ϕ_i were treated as if they were interferometric data, and a set of equations of the form (14) were

generated. These were solved with the least squares method to obtain an approximation to $\Delta n(x, y)$. By comparing this approximation to the actual distribution, we could evaluate the error in the method. Figure 34a is a computer plot of the actual distribution for $\mu_x = \mu_y = 0.29$, $\Delta_x = \Delta_y = 0.29$. The square region under study was broken into 36 elements, and 102 rays were used in the analysis. Figure 34b is a plot of the approximate solution for $\Delta n(x, y)$. The actual and computed distributions are also compared in Table 5. The percentage of error in this table is defined by

$$\epsilon = \frac{\Delta n_{actual} - \Delta n_{calculated}}{\Delta n_{maximum} - \Delta n_{minimum}} \tag{16}$$

These results should be considered to be preliminary and not necessarily indicative of the accuracy which will ultimately be attainable with this method. The distribution (15) actually gives a rather severe test for the method. It is completely asymmetric, has discontinuities, and is nonzero at the boundaries. In addition, we limited the total angle of view to 154° rather than use a full-field view of 180°. The results for other test functions, which vanish smoothly at the boundaries, show higher accuracy.

The method was also applied to the analysis of actual experimental data. As a phase object, we used the convective plume above a heated, horizontal, 3/4-in.-long wire which was submerged in water. The optical arrangement for this experiment is shown in Fig. 30. We achieved multi-directional illumination by using a grating, as discussed in Section 6.3. Figure 35 shows three of the six interferograms generated by one double-exposure holographic interferogram. The fringe frequencies in this figure are as high as 20 lines/mm. The viewing angle over which data were obtained was 14°; however, because we assumed that the temperature distribution was symmetric about the center of the wire, this angle was equivalent to a total viewing angle of 28°. The position of each fringe in each view was recorded. These data represented the differential optical path length in wavelength units. Using these experimental values for the ϕ_i's in Eq. (9), we solved the resulting set of 316 equations with the least squares method for 36 values of the unknown, differential, refractive index. Using an empirical relation for refractive index of water as a function of temperature, we computed the temperature distribution. A computer plot of the temperature distribution produced by this computation is shown in Fig. 36, in which the maximum temperature rise shown is about $15^\circ F$. This preliminary experiment was performed in order to demonstrate application of this method; no accurate check of the error is available.

6.4.4. CONCLUSIONS

We have demonstrated a method of analyzing data obtained by holographic interferometry to determine the three-dimensional structure of a differential, refractive-index field. Although more work is required to develop the method fully, this investigation shows it to be feasible and

TABLE 5. RESULTS OF COMPUTER SIMULATION

Element	Actual Δn	Calculated Δn	Normal Error (%)
(1, 1)	0.0541	0.0534	0.0830
(1, 2)	0.0689	0.0494	2.5173
(1, 3)	0.0625	0.0778	-1.9664
(1, 4)	0.0404	0.0270	1.7206
(1, 5)	0.0186	0.0247	-0.7928
(1, 6)	0.0061	0.0029	0.4075
(2, 1)	0.1654	0.1862	-2.6846
(2, 2)	0.2109	0.2011	1.2569
(2, 3)	0.1913	0.1978	-0.8295
(2, 4)	0.1235	0.1188	0.6130
(2, 5)	0.0568	0.0427	1.8130
(2, 6)	0.0186	0.0136	0.6389
(3, 1)	0.3599	0.3474	1.6057
(3, 2)	0.4590	0.4440	1.9192
(3, 3)	0.4164	0.4227	-0.8073
(3, 4)	0.2689	0.2630	0.7555
(3, 5)	0.1235	0.1201	0.4426
(3, 6)	0.0404	0.0740	-4.3287
(4, 1)	0.5575	0.5659	-1.0844
(4, 2)	0.7109	0.7141	-0.4109
(4, 3)	0.6450	0.6441	0.1136
(4, 4)	0.4164	0.4029	1.7391
(4, 5)	0.1913	0.1933	-0.2603
(4, 6)	0.0625	0.0552	0.9494
(5, 1)	0.6144	0.5624	6.6946
(5, 2)	0.7834	0.7953	-1.5310
(5, 3)	0.7109	0.6911	2.5446
(5, 4)	0.4590	0.4372	2.8043
(5, 5)	0.2109	0.2367	-3.3254
(5, 6)	0.0689	0.0735	-0.5836
(6, 1)	0.4818	0.4560	3.3209
(6, 2)	0.6144	0.6093	0.6588
(6, 3)	0.5575	0.5007	7.3091
(6, 4)	0.3599	0.3907	-3.9602
(6, 5)	0.1654	0.1637	0.2155
(6, 6)	0.0541	0.0515	0.3255
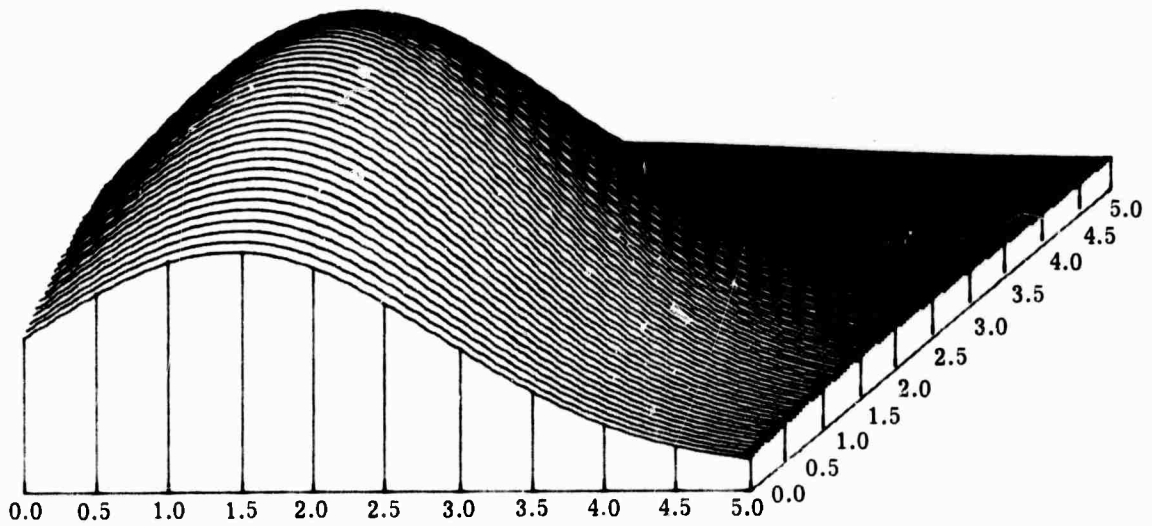
(a) Actual Distribution Used to Generate Simulated Data
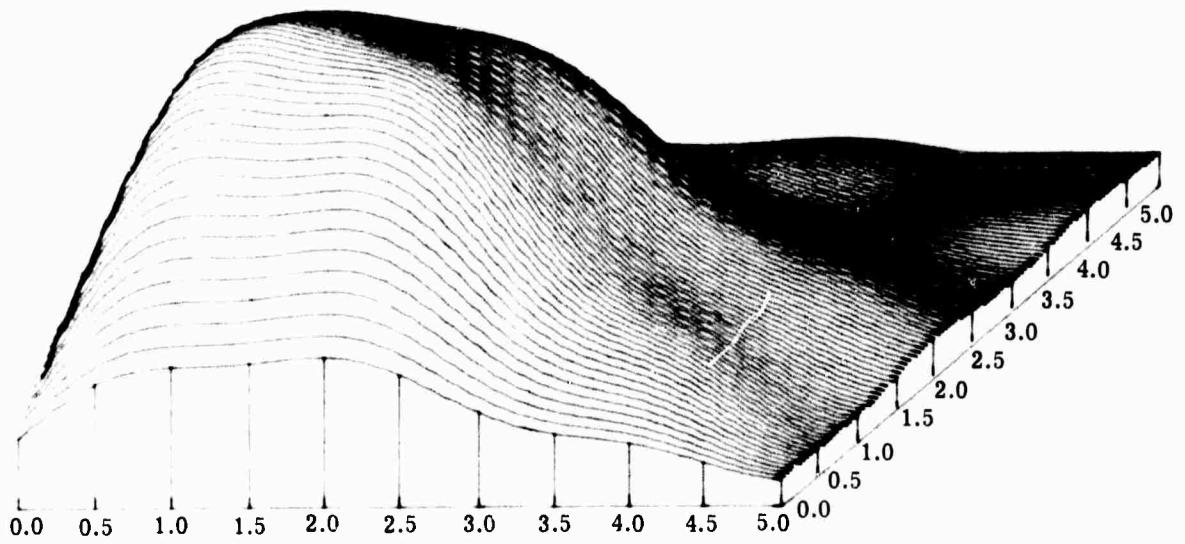
(b) Distribution Reconstructed from Simulated Data

FIGURE 34. COMPUTER SIMULATION OF REFRACTIVE-INDEX FIELD

52
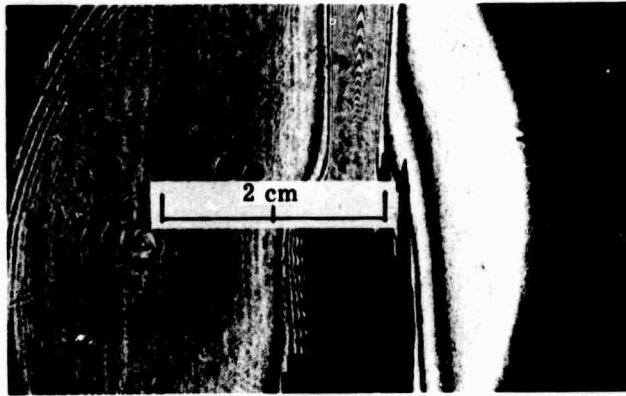
(a)
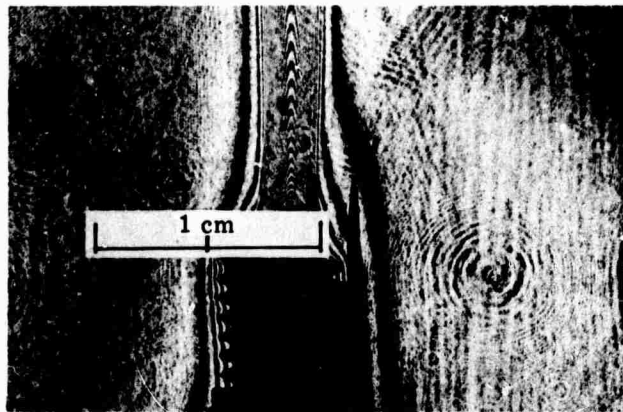
(b)
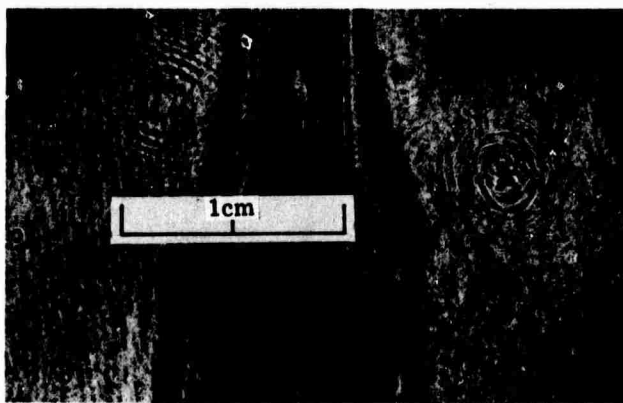
(c)

FIGURE 35. THREE VIEWS OF THE MULTI-
DIRECTIONAL INTERFEROGRAM

relatively convenient. Particular advantages of this analysis technique include the following:

(1) The series used to represent the distribution need not be orthogonalized; hence, unlike other methods, data need not be taken over the full 180° range of viewing angle.

(2) The use of an overdetermined system of equations and the form of the series used to represent the distribution make the task of taking appropriate data from the inter-ferogram convenient and improve the accuracy of the solution.

6.5. INTERFEROMETRY WITH BOTH BEAMS TRAVERSING THE OBJECT

6.5.1. BACKGROUND

Because of the small wavelength of light, optical interferometry is a sensitive measurement technique. In fact, for some applications, it may be too sensitive. For example, if holographic interferometry is used as a tool for experimental stress analysis of a transparent model, the desired load may produce excessively fine fringes which make viewing difficult and produces refraction errors making fringe interpretation difficult. If one could control its sensitivity, interferometry might be a more useful technique for detection of flaws or inhomogeneities in transparent objects. In this section, we describe a technique for reduced-sensitivity holographic interferometry of transparent objects.

6.5.2. EXPERIMENTAL METHOD AND RESULTS

Figure 37 shows the optical arrangement for recording the hologram. Two coherent plane waves traverse a transparent object at slightly different angles. The resulting intensity pattern is recorded on film to form a hologram. No additional reference wave is used during this expo-sure. We will show that if this hologram is reconstructed by one of the plane waves, the fringe pattern obtained by interference of this reconstructed wave with the other plane wave is indicative of the difference in optical path of the two waves which traversed the object. This technique is suggested by the method, developed by Goodman and his colleagues [55, 56], of holographic imaging through aberrating media. They demonstrated that by placing a coherent point source very close to an object and recording a hologram, one could minimize the aberrations caused by refracting media between the object and the hologram plane, since both the object and reference waves deviate in approximately the same manner. We have applied this concept to interferometry.

The two waves striking the hologram in Fig. 37 are denoted by

$$\underline{u_1} = a_1 \exp i[\alpha_1 x + \phi_1(x, y)] \tag{17}$$

and

$$\underline{u_2} = a_2 \exp i[\alpha_2 x + \phi_2(x, y)] \tag{18}$$

where α_1 and α_2 are proportional to the angles of propagation of the waves, and $\phi_1(x, y)$ and
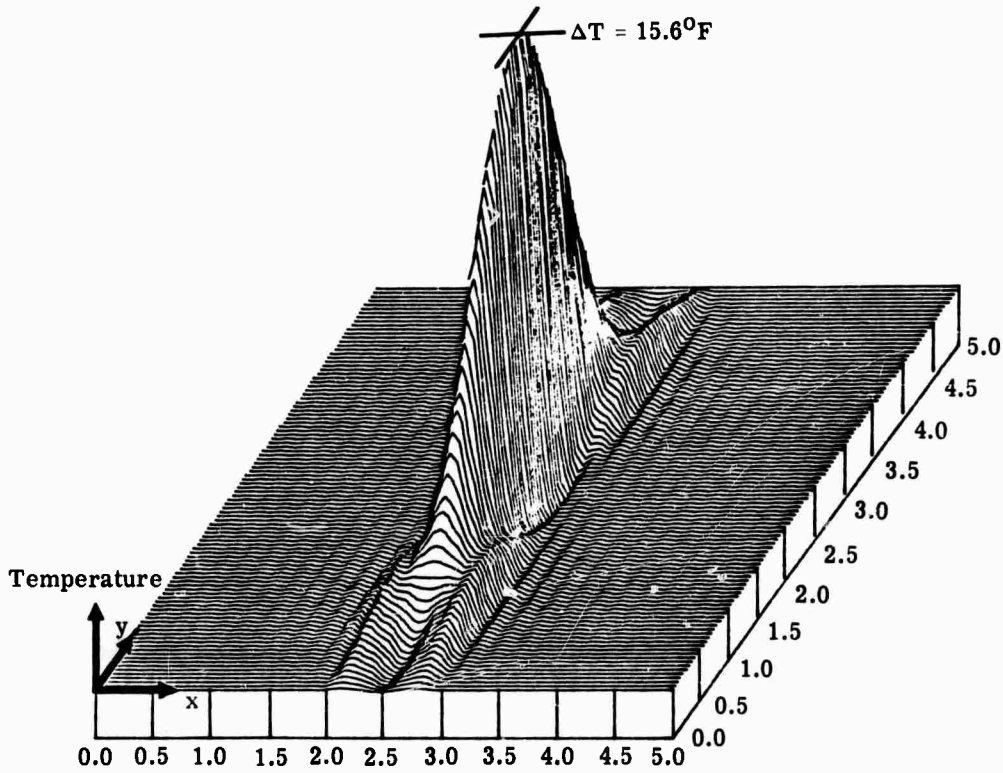
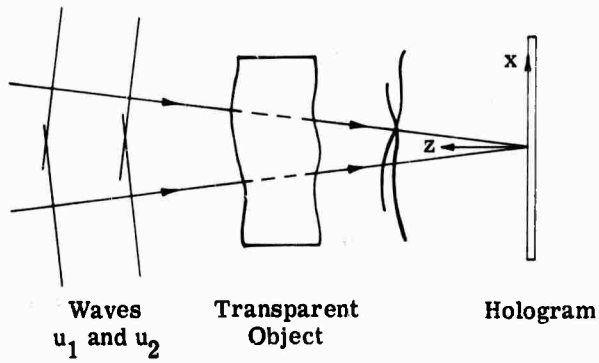FIGURE 36. CALCULATED TEMPERATURE FIELD

FIGURE 37. OPTICAL ARRANGEMENT FOR
RECORDING THE HOLOGRAM

55

$\phi_2(x, y)$ describe the phase variations introduced by the transparent object. As usual, the temporal variation has been suppressed. Let us further assume that $a_1 = a_2 = a$, and that α is uniform across the hologram plane. Under these assumptions, an ideal, linearly recorded hologram would have an amplitude transmittance of

$$t(x, y) = t_b + \beta(\underline{u_1}\underline{u_2}^* + \underline{u_2}\underline{u_1}^*) \tag{19}$$

If we reconstructed this hologram by illuminating it with a plane wave, $\underline{u}_{1p} = a \exp i(\alpha_1 x)$, the reconstructed virtual wavefront would be

$$\underline{u}_{2v} = \gamma a^3 \exp i(\alpha_2 x + \phi_2 - \phi_1) \tag{20}$$

If this reconstructed wavefront interferes with a plane wave, $\underline{u}_{2p} = \gamma a \exp i(\alpha_2 x)$, the resulting intensity is

$$I = K + 2\beta\gamma a^4 \cos(\phi_2 - \phi_1) \tag{21}$$

where K is a constant and γ is an attenuation factor. This interference pattern is only indicative of $\delta\phi = \phi_2(x, y) - \phi_1(x, y)$, which represents the difference in phase variations introduced into the plane waves which traverse the object in different angular directions.

The most obvious feature of this interferometer is that its sensitivity can be very low in comparison with, for instance, the frequency of a Mach-Zehnder interferometer. It may, therefore, be applied to the study of quite coarse phase objects. The interferometer is sensitive to phase variations in the x direction but not in the y direction. If one considers the formation of a hologram—two rays traverse the object and converge to the point on the film at which they interfere, it is obvious that this interferometer is most sensitive to gradients of refractive index in planes far from the hologram where the rays are considerably separated from each other. The interferometer is least sensitive very close to the hologram where the rays nearly coincide. We can shift the region of low sensitivity along the z axis by placing an imaging lens between the object and the hologram. This procedure may be used to study the structure of three-dimensional phase objects. For this application, the two-hologram technique suggested by Bryngdahl and Lohmann [57], together with Goodman's holographic imaging scheme, could be used to advantage.

We have conducted experiments which demonstrate several of the predicted features of this technique. Two coherent plane waves were generated with an optical setup similar to a Michelson interferometer. All holograms were recorded on Kodak 649-F spectroscopic plates with 6328-Å light. Figure 38 shows three interferograms of the same transparent object (a sheet of plexiglass, 0.635-cm thick). 38a was produced by the method described above; the angle between the beams was 1°, and the object was located about 3.2 cm in front of the hologram. We produced the fringe pattern in 38b by placing the object in a Mach-Zehnder interferometer also with 6328-Å light.
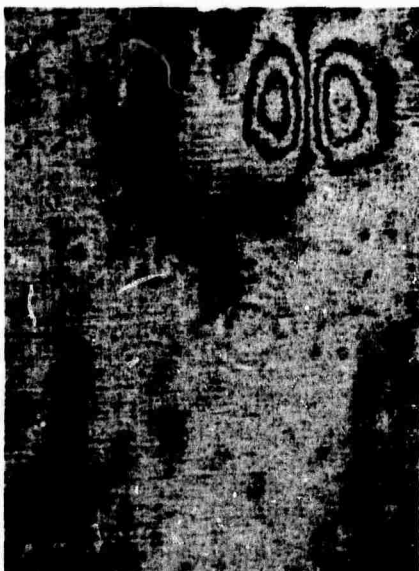
(a) Desensitized Interferogram.
Beam angle = 1°.

(b) Bright-Field Mach-Zehnder
Interferogram.

NOT REPRODUCIBLE

(c) Desensitized Interferogram.
Object rotated 90° prior to re-
cording.

FIGURE 38. THREE INTERFEROGRAMS OF THE SAME PORTION OF A TRANSPARENT
OBJECT

Note that the fringes in 38a are indeed coarse and tend to emphasize lateral variation of phase (i.e., are indicative of the gradient of phase in the lateral direction) as compared with the fringes in 38b. The fringes in 38c were produced as in 38a, except that the object was rotated 90° in the (x, y) plane.

The ability to vary the sensitivity of this interferometer is further illustrated by Fig. 39. The interferogram shown in 39a was produced in the same manner as that in 38a, except the angle between the beams was 3° rather than 1°; hence, the fringes in 39a are more numerous than those in 38a. 39b and 38c may be similarly compared.

For simplicity and ease of adjustment during the experiments reported here, a double-exposure technique was used. During the first exposure, both waves passed through the object and exposed the film. The object was then removed, and the film was exposed to the two plane waves. The second recording simply provided a hologram of the wave, u_{2p}, which is required to form the final interference pattern. Then the developed hologram was illuminated with the other plane wave, u_{1p}, the output of the hologram was Fourier-transformed with a spherical lens, and the unwanted spectral components were filtered out. It should be noted that the angle between the waves which form the hologram is sufficiently small that both the real and virtual holographic images appear upon reconstruction [58]. It is easily shown and has been verified experimentally that we can obtain the same interference pattern using the virtual image.

The basic properties of the interferometer were clearly illustrated by the use of a thin (9° wedge) prism as an object. Figure 40a is an interferogram produced with this method. One wave was parallel to the front face of the prism, and the other was tilted at an angle of 1°. The prism, with its wedge in the (x, y) plane, was located 5 cm in front of the hologram. The resulting fringe frequency is about 4 lines/cm. The fringes shown in 40b were produced with the same setup, but with a 5° angle between the beams. The resulting fringe frequency is 22 lines/cm. We measured the absolute fringe frequency from refraction by the prism by placing the prism in a portion of a collimated beam. The interference between the refracted and unrefracted portions of the beam was recorded on film. The resulting fringe frequency was found, with a scanning microdensitometer, to be 135 lines/mm. When the prism was turned 90° so that the wedge lay in the (y, z) plane, no fringes were produced, since no x gradient of phase was introduced. It is interesting to note that the fringes produced by this interferometer are indicative of deviations from the thin-prism approximation. In this approximation, the linear phase shift introduced is independent of the angle of incidence. If this were indeed the case, no fringes would be produced by this interferometer.

In conclusion, we suggest that the concept of perturbing both the object and the reference waves may lead to interesting new methods and applications of holographic interferometry. We have illustrated this suggestion in terms of a particular interferometer. For thin phase objects,
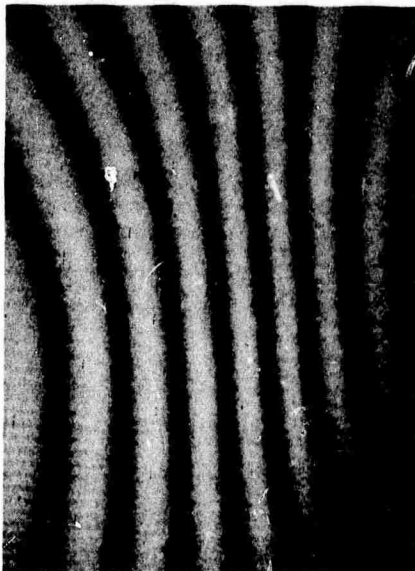
(a) Desensitized Interferogram.
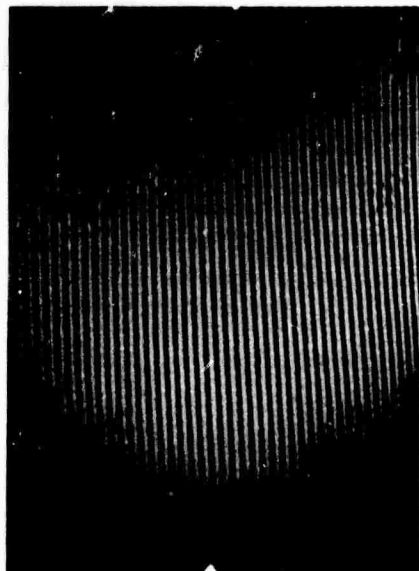Beam angle = 3°.

(b) Desensitized Interferogram.
Object rotated 90° prior to re-
cording.

FIGURE 39. TWO INTERFEROGRAMS OF THE SAME PORTION OF THE OBJECT IN
FIGURE 38

(a) Beam Angle = 1°

(b) Beam Angle = 5°

FIGURE 40. TWO INTERFEROGRAMS OF A 9° WEDGE PRISM

the output of this interferometer is nearly analogous to that of a shearing interferometer. For phase objects of greater thickness, the measurement could be duplicated only by physical rotation of the object between exposures in ordinary two-exposure holographic interferometry. This rotation would be impossible if the refractive-index distribution under study varies with time.

6.6. SUMMARY

We conducted a basic investigation into examination of three-dimensional transparent objects. This work may be of long-range significance in locating nonhomogeneities or other defects in transparent materials and in three-dimensional, experimental, stress analysis. We developed (1) an experimental technique for recording multidirectional interferometric data without laser speckle, (2) a technique for analyzing multidirectional interferometric data to measure three-dimensional, refractive-index fields, and (3) an experimental scheme for producing variable-sensitivity interferograms of transparent objects.

7
MEASUREMENT OF VIBRATIONAL AMPLITUDE

7.1. INTRODUCTION

Time-average holography has proved quite useful for measuring the amplitude of vibration of diffusely reflecting surfaces. Wells [25] and Denby and Butters [26], among others, have discussed the application of time-average holography to the nondestructive testing of honeycomb panels and of turbine disks. In previous reports, we have discussed variable-sensitivity amplitude measurements [32] and detection of vibrational phase by modulated, reference-wave holography.

In this section, we discuss a technique which we have developed for measurement of vibrational amplitude. The technique is not holographic but is closely related to time-average holography in concept. It is a full-field, variable-sensitivity technique which has lower requirements on mechanical stability of the system than holographic techniques.

7.2. DESCRIPTION AND ANALYSIS

The diffuse surface under study is placed in an optical field consisting of two mutually coherent plane waves which propagate in slightly different directions. If the surface is diffuse, a fringe pattern will be formed on it because of the interference of the two plane waves. These fringes will be referred to hereafter as the carrier fringes. This illumination with a laser interference pattern has previously been used by Hildebrand [59] and by Brooks and Heflinger [60] to generate surface contour maps. If a time-averaged image of a surface vibrating within the interference field is formed, either photographically or by visual persistence, it is found that

the visibility of the fringes formed on the surface is modulated by a function of the local amplitude of vibration. Thus, loci of constant vibrational amplitude can be directly observed as regions of high or low fringe visibility in the image of the surface. In most cases, the amplitude loci can be even more clearly observed by simple optical processing of the image.

The method is nearly as simple as speckle techniques [61, 62, 63] to apply and has similar low mechanical stability requirements, yet it produces a map of vibrational amplitude —not just nodal regions —which can be recorded photographically with relative ease. Adjusting the propagation directions of the plane waves and the orientation of the surface allows variations in the sensitivity. In practice, the method operates best at sensitivities which are lower than that of holographic interferometry.

A heuristic explanation of the method for sinusoidal vibration is simple: a surface executing a simple harmonic motion spends a large part of its vibrational period near its two extreme positions. If the fringe pattern formed on a portion of such a surface is identical in each of these two extreme positions, distinct fringes will appear in the time-averaged image of that region of the surface. In another region of the surface, which has a different amplitude, the fringe pattern at the two extreme positions will be out of phase, and the time-averaged image will have low-visibility fringes. The image will thus be overlaid with a pattern of straight fringes in which bands of low visibility represent loci of constant amplitude.

In its basic form, the experimental realization of this technique requires only a means for generating two plane waves of mutually coherent light. It is also desirable to use a camera or other imaging system to make photographic recordings of the fringe pattern on the vibrating surface. Because coherence over a large area is necessary, laser illumination is required. The interfering plane waves can be formed, for example, by an interferometer such as a Michelson or Mach-Zehnder device, by Lloyd's mirror, by a reflection or diffraction grating, or by double-surface reflection. For illumination of a large surface, it may be more practical to use two real or apparent point sources located a large distance from the object.

To analyze the process by which vibrational amplitude is mapped, consider the object and coordinate system shown in Fig. 41. The surface, assumed to be locally plane, oscillates sinusoidally in the z direction. At any instant of time, the complex optical amplitude in the object plane is given by

$$U = A \left(\exp\{-j2\pi[\alpha_1 y + \beta_1 z_0(x, y) \cos \omega t]\} + \exp\{-j2\pi[\alpha_2 y + \beta_2 z_0(x, y) \cos \omega t]\} \right) \quad (22)$$

where $\alpha_{1,2} = \dfrac{\sin \theta_{1,2}}{\lambda}$ and $\beta_{1,2} = \dfrac{\cos \theta_{1,2}}{\lambda}$. The amplitude A, which is common to both waves, is assumed to be uniform over the object surface. The temporal variation has been suppressed; and the arbitrary constant phase difference between the two waves has been ignored, since its

61
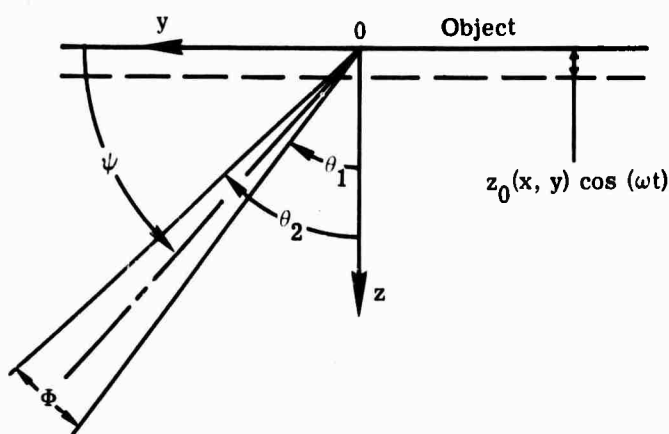
FIGURE 41. COORDINATE SYSTEM AND NOMENCLATURE

effect vanishes during averaging over a long period of time. It should be noted that, unlike most interferometric techniques, the coherent addition of the optical waves to form the inter-ference pattern occurs at the object surface itself. The instantaneous intensity in that plane is

$$I = UU^* = 2A^2\{1 + \cos 2\pi[(\alpha_1 - \alpha_2)y + (\beta_1 - \beta_2)z_0 \cos \omega t]\} \qquad (23)$$

This intensity distribution, imaged onto the retina of the eye or onto photographic film, pro-duces a time-averaged exposure which will be proportional to the averaged intensity over one vibrational period,

$$<I>_t = 2A^2 \int_{-\pi/\omega}^{\pi/\omega} \{1 + \cos 2\pi[(\alpha_1 - \alpha_2)y + (\beta_1 - \beta_2)z_0 \cos \omega t]\} dt$$

$$= 2A^2 \int_{-\pi/\omega}^{\pi/\omega} \{1 + [\cos 2\pi(\alpha_1 - \alpha_2)y] \cos 2\pi[(\beta_1 - \beta_2)z_0 \cos \omega t]$$

$$- [\sin 2\pi(\alpha_1 - \alpha_2)y] [\sin 2\pi(\beta_1 - \beta_2)z_0 \cos \omega t]\} dt \qquad (24)$$

The third integral in (24) vanishes identically, and evaluation of the remaining two integrals yields

$$<I>_t = K\{1 + J_0[2\pi(\beta_1 - \beta_2)z_0(x, y)] \cos 2\pi(\alpha_1 - \alpha_2)y\} \qquad (25)$$

where K is constant and J_0 is the zero-order Bessel function of the first kind.

Equation (25) represents the fringe pattern observed in real-time or by time-exposure photography. It should be noted that the amplitude of the cosine term is modulated by a zero-order Bessel function, the argument of which is proportional to the local amplitude of vibration.

62

Using the classical definition of fringe visibility

$$V = \frac{I_{MAX} - I_{MIN}}{I_{MAX} + I_{MIN}}$$

it is found that

$$V = J_0[2\pi(\beta_1 - \beta_2)z_0(x, y)] \qquad (26)$$

Hence, the fringe visibility is determined by the local amplitude of vibration. The sensitivity of the amplitude measurement can be varied by changing the quantity $(\beta_1 - \beta_2)$, i.e., by adjusting the orientation of the incident plane waves. The expression (26) for fringe visibility can be also written as

$$V = J_0\left[\frac{4\pi}{\lambda} \left(\cos \psi \sin \frac{1}{2}\Phi\right)z_0(x, y)\right] \qquad (27)$$

where ψ is the angle between the object surface and the mean direction of propagation of the incident beams, and Φ is the angle between the incident beams. This form is convenient because the angles ψ and Φ are readily determined experimentally.

As will be demonstrated in the following section, when the spatial frequency of the fringes is low (i.e., in low-amplitude-sensitivity measurements), we can obtain the amplitude mapping by directly viewing the variation of fringe visibility. When the fringe frequency is high or when there is some extraneous intensity variation over the object surface, it is preferable to perform elementary optical processing on a transparency of the fringe pattern. Suppose that the transparency is exposed and developed so that its amplitude transmittance T is proportional to the time-averaged intensity pattern:

$$T = k_0\{1 + J_0[2\pi(\beta_1 - \beta_2)z_0(x, y)] \cos 2\pi(\alpha_1 - \alpha_2)y\} \qquad (28)$$

This transparency can be illuminated by a plane wave of uniform amplitude propagating normal to it. A simple lens and aperture can then be used to filter out all wave components leaving the transparency except for one first-diffracted order. When this first-order diffracted wave is reimaged, its intensity distribution will be

$$I_D = k_1 J_0^2[2\pi(\beta_1 - \beta_2)z_0(x, y)] \qquad (29)$$

where k_1 is a constant of proportionality. Thus, by simple optical processing of the time-averaged image, we can generate fringes which are loci of constant vibrational amplitude.

7.3. EXPERIMENTAL TECHNIQUES AND RESULTS

We conducted experiments using the apparatus depicted in Fig. 42a. Light from a Spectra-Physics He-Ne laser, Model 125 was expanded, filtered, and collimated. The collimated light

was then amplitude-divided by a Michelson Interferometer into two plane waves traveling in slightly different directions. The vibrating surface being studied was placed in the optical field produced by the interferometer so that the angle between the surface and the mean direction of propagation of the optical waves was small. The resulting fringe pattern formed on the surface was either viewed directly or photographed.

(a) System Used for Analysis of Vibrating Surfaces

(b) System Used for Optical Processing
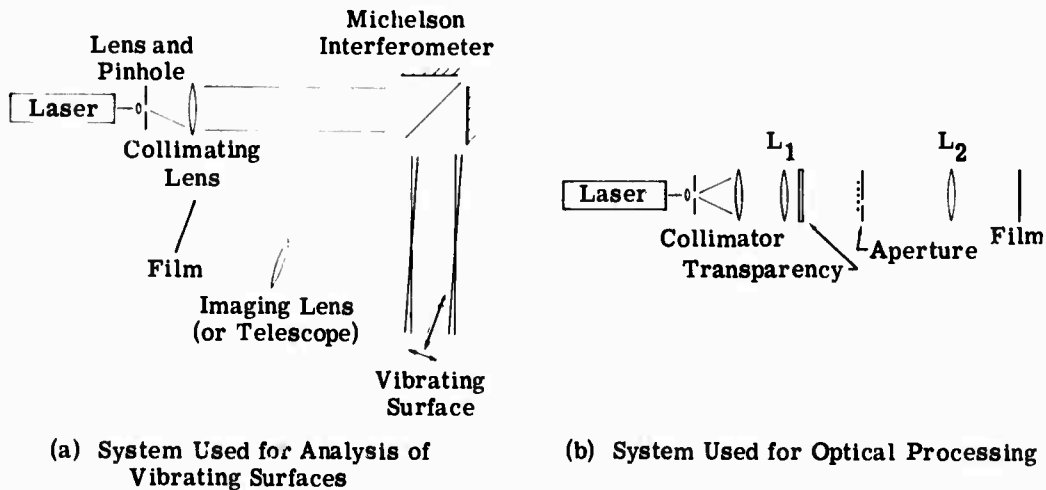
FIGURE 42. OPTICAL APPARATUS

Figure 43 shows some typical experimental results. The object was a circular, 10-cm diameter, cardboard diaphragm. It was excited by a loudspeaker (air coupling) which was driven at a frequency of 50 Hz by an audio oscillator. Figure 43a is a time-average photograph (recorded on Polaroid P/N film) of the fringe pattern on the diaphragm. Note that the fringes around the outer periphery, which was glued to a rigid annulus, have high contrast, while at smaller radii, concentric circular bands of very low fringe contrast are visible. These are loci of constant vibrational amplitude. They were also discernible by direct visual observation. The fringe pattern in Fig. 43b was produced by the same technique, except that the orientation of the plane waves was changed to increase the amplitude sensitivity. This photograph was recorded on an Agfa 10E75 plate. Because of the higher fringe frequency and some nonuniformity of intensity over the surface, the bands of low fringe contrast are less obvious than in Fig. 43a; however, the distinct fringes of constant vibrational amplitude shown in Fig. 43c were produced by simple optical processing of a transparency of Fig. 43b. It may be noted that we can often greatly enhance the fringe contrast effect in a photograph such as Fig. 43b by simply making a xerographic copy of it. Figure 44 shows a more complicated vibrational pattern obtained when the diaphragm was excited at a frequency of 690 Hz. This fringe pattern was produced by optical processing of a time-average photographic transparency.

(a) Bands of Low Carrier Fringe Contrast
Are Loci of Constant Vibrational Amplitude

(b) Same as Part a but with Higher Carrier-
Fringe Frequency
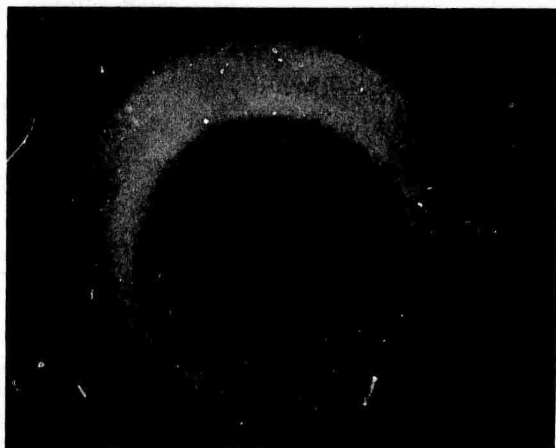
(c) Fringes Representing Constant Vibra-
tional Amplitude Obtained by Optical Pro-
cessing of Part b.

FIGURE 43. TYPICAL EXPERIMENTAL RESULTS. The object is a 10-cm-diameter circular
disk vibrating at 50 Hz.

The optical processing which produced this fringe pattern was quite straight-forward. A beam of laser light diffracted by a transparency of the fringe pattern was Fourier-transformed by a lens. All spectral components other than one first-diffracted order were filtered out, and the remaining wave was reimaged onto Polaroid film. The optical apparatus which was used is shown in Fig. 42b.

The real-time capability for measuring relatively large amplitude vibrations is evident in Fig. 45, a photograph of a rigid flat plate (6 cm × 6 cm) which was executing a rocking motion about its diagonal at a frequency of 50 Hz. The bands of low fringe contrast were quite apparent to the unaided eye.

In order to determine vibrational amplitudes quantitatively, the angles θ_1 and θ_2 (or, alternatively, ψ and Φ) must be measured. Once these are known, the amplitude corresponding to each fringe (i.e., zero of J_0 in Eqs. (26) and (27) can be computed. The dimensionless amplitudes corresponding to the first few fringes are shown as a function of $(\cos \theta_1 - \cos \theta_2)$ in Fig. 46.

In practice, it is convenient to measure ψ and Φ rather than θ_1 and θ_2, since we can determine Φ by Fourier-transforming the two plane waves with a lens and measuring the separation of their spectrum in the back focal plane. We can then determine the angle ψ by measuring the fringe frequency on the object. With this procedure, it was determined that the amplitude corresponding to the first dark fringe in Fig. 44 was 12.7 μm; the corresponding value of Fig. 45 was 83.4 μm.

7.4. DISCUSSION

A noncontacting, full-field, variable-sensitivity optical technique for mapping the amplitude of a vibrating diffuse surface has been developed. Loci of constant vibrational amplitude can be observed in three ways: (1) as regions of constant carrier-fringe visibility in the real-time image of the surface, (2) as regions of constant carrier-fringe visibility in a time-average photographic image of the surface, and (3) as direct fringes of constant amplitude obtained by elementary spatial filtering of the time-average photographic image of the surface. This technique combines the amplitude measurement capability normally associated with time-average holography with the convenience of low mechanical stability requirements and of real-time viewing normally associated with speckle techniques. In theory, the maximum amplitude sensitivity is one-half that of time-average holography; in practice, this requires resolution by the imaging system of unrealistically high fringe frequencies; hence, the technique works best when relatively large amplitudes are to be measured. In this sense, the technique is complementary to time-average holography.

There is a fairly close relationship between this technique and that recently developed by Eliasson and Mottier [63], who place the vibrating surface in a "grainy" light field produced by

FIGURE 44. FRINGES OF CONSTANT VIBRA-
TIONAL AMPLITUDE AT 650 Hz (OF SAME
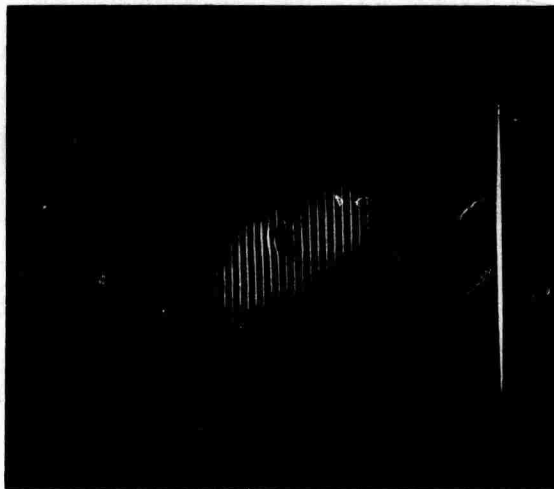OBJECT SHOWN IN FIGURE 43)

FIGURE 45. CARRIER FRINGES ON RIGID
PLATE WHICH IS OSCILLATING ABOUT ITS
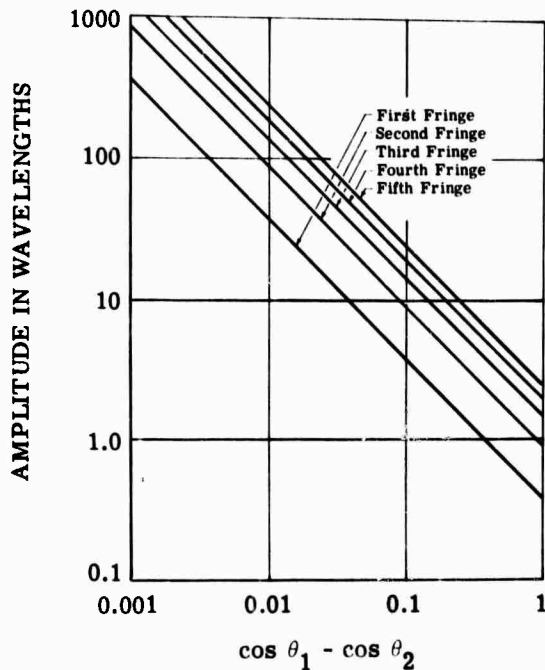DIAGONAL AT 50 Hz

67

FIGURE 46. DIMENSIONLESS AMPLITUDE REP-
RESENTED BY FRINGES AS A FUNCTION OF
PLANE-WAVE ORIENTATION

a diffusing surface. Since the variation of this grain in the direction of vibration is random the resulting speckle pattern on the object surface carries information only about the nodal areas. When the random grainy pattern is replaced by a periodic interference pattern, as in the technique presented here, the resulting fringe pattern on the object surface carries information regarding the local vibration amplitude. A second advantage of using a constant, rather than random, carrier frequency is that fringes of constant amplitude can be generated by elementary spatial filtering. This feature largely alleviates the photographic difficulties normally associated with speckle techniques.

The speckle interferometry technique of Archbold, et al. [64], and Ek and Molin [65] is capable of producing loci of constant amplitude in terms of a modulated speckle contrast; however, the modulation is not as strong as that in the technique described here, and because of the randomness of the carrier, enhancement by spatial filtering is not convenient.

There are two major limitations inherent in our method. First, the method is difficult to apply when the surface being studied is not relatively flat. If the surface has some contour, the fringe frequency and, hence the amplitude sensitivity will vary over the surface. This complicates interpretation and makes spatial filtering difficult. If the contour is too convoluted, shadowing will occur and the method cannot be used at all. Second, vibrational sensitivity and

object size are limited by the system resolution when a photographic record is required. The imaging system must be capable of resolving the fringes over the entire area to be studied, and the film must be capable of recording the resulting fringe frequency in the image. For real-time observation, object size is apparently limited only by the available laser power.

It is interesting to note that slight changes in small-scale surface structures of the vibrating object, which would rule out the use of interferometric techniques such as time-average holography, would have no appreciable effect on this technique. This feature would be of importance, for example, in tests involving fatigue. It may also be noted that the method is rather insensitive to variations in refractive index of the medium surrounding the vibrating surface. This is true for two reasons: (1), the two interfering waves travel very nearly the same path to the object, and (2) because the interference is detected by the object surface itself, refractive-index variations between the object and the observer are relatively unimportant. This feature is of potential value in the study of surfaces vibrating in liquid environments where acoustic-pressure or temperature fields create a significant refractive-index variation.

Finally, a few possible extensions of the technique might be mentioned. It could easily be operated in a stroboscopic mode with the use of either a shutter system or a periodically pulsed laser. This would allow one to observe the amplitude structure at various intermediate phases of the vibration cycle.

A second extension involves modulation of the interfering plane waves. For example, one could phase-modulate one of the waves at the same frequency as the object vibration and with a known phase difference. The instantaneous amplitude in the object plane would be

$$U = A\ (\exp\left\{-j2\pi[\alpha_1\ +\ \beta_1 z_0(x,\ y)\cos\omega t]\right\}$$

$$+\ \exp\left\{-j2\pi[\alpha_2 y\ +\beta_2 z_0(x,\ y)\cos\omega t + M\cos(\omega t + \phi)]\right\}) \tag{30}$$

where $2\pi M$ is the amplitude of the phase modulation and ϕ is the fixed phase difference between the object and modulator vibrations. The fringe visibility in the corresponding time-averaged image of the surface would then be

$$V = J_0\left\{2\pi\left[(\beta_1 - \beta_2)^2 z_0^2 + M_2 + 2M(\beta_1 - \beta_2)z_0 \cos\phi\right]^{1/2}\right\} \tag{31}$$

Examination of the argument of this fringe visibility function shows that information regarding the relative phase as well as amplitude of vibration can be recovered by this procedure, which is directly analogous to modulated reference-wave holography [66, 67].

7.5. SUMMARY

A new method for optical mapping of the amplitude of a vibrating surface was developed. This method complements time-average holography, which has been used in holographic non-

destructive testing. The new method operates in real time, and its amplitude sensitivity can be varied.

8
HOLOGRAPHIC CONTOURING

8.1. INTRODUCTION

The majority of the applications of holography to material testing reported here and else-where have used holographic interferometry to measure surface displacements or changes in refractive index. Relatively few researchers [68-72] have pursued the fact that, in addition to measuring such changes in object configuration, holographic interferometry can be used to produce a contour map of the object's shape. Some possible applications of contour maps are:

(1) Contour maps of master parts for quality control comparison.

(2) Contour maps as inputs to numerically controlled machining systems.

(3) Contour maps to furnish the surface shape measurements necessary for obtaining strain data from holographic interferometry.

(4) An extension of holographic interferometry which uses contour maps to study displace-ments.

The work reported in this section deals primarily with the development of the theory and experimental technique of MFHC (multiple-frequency holographic contouring) to the level at which practical applications could be realized. This particular technique of holographic con-touring has been emphasized largely because it permits one to vary the contouring interval (i.e., the sensitivity of the method) and because it can be adapted to pulsed laser systems to produce single-pulse contour maps for the study of transient events. Only a brief summary of some of the major aspects of this work is presented here. The investigation of MFHC is re-ported in full detail in the doctoral thesis by Varner [73].

8.2. MULTIPLE-FREQUENCY HOLOGRAPHIC CONTOURING (MFHC)

Suppose that an off-axis hologram of an object is recorded in the usual way except that a two-frequency source is used instead of a monochromatic source. If this hologram is recon-structed by illuminating the object with one frequency of the original reference beam, the in-tensity of the reconstructed wavefront in some observation plane can be shown to be

$$I = K\left(\left|U_{01}\right|^2 + \left|U_{02}\right|^2 + 2\left|U_{01}\right|\left|U_{02}\right| \cos \Delta\theta\right) \tag{32}$$

where U_{01}, U_{02} are the object waves of wavelength λ_1 and λ_2 respectively, and $\Delta\theta$ is a function of the difference in optical path lengths for the two frequencies. We assume that there is a

one-to-one correspondence between points in the observation plane and narrow bundles of rays passing through the test point, and that $\Delta\theta$ is defined by

$$\Delta\theta = \frac{2n_2\gamma_0}{\lambda_2} - \frac{2n_1\gamma_0}{\lambda_1} \tag{33}$$

where γ_0 is the average length of the rays in the corresponding bundle. Bright interference fringes will be observed in this observation plane at points where $\Delta\theta = 2\pi N$, $N = 0, 1, 2, \ldots$. Hence, two adjacent fringes will correspond to a difference in distance to the object of

$$\Delta r_0 = \frac{\lambda_1\lambda_2}{|n_1\lambda_2 - n_2\lambda_1|} \tag{34}$$

Here λ_1 and λ_2 are the in vacuo wavelengths and n_1 and n_2 are the refractive indices of the test environment corresponding to the two source frequencies. Obviously, this contouring interval can be varied by varying the two source frequencies. The above relations regarding MFHC are all derived with the assumption that the condition

$$k_1\gamma_1(x) = k_2\gamma_2(x) \tag{35}$$

is satisfied. Here, $\gamma_1(x)$ is the path traveled by the reference wave of wavelength λ_1, $\gamma_2(x)$ is the path traveled by the reference wave of wavelength λ_2, and $k_{1,2}$ are the propagation numbers $2\pi/\lambda_{1,2}$. Satisfying this relation allows perfect alignment of the two zero-order, object-wave components. This relation places an important constraint on the design of the contouring scheme and apparatus.

In most practical applications, it is preferable to design the optical system so that the contouring surfaces are plane (i.e., so that true depth contours with respect to a plane of known orientation are generated). Other contouring surfaces can be generated if necessary. Further, Varner's extensive analysis [73] suggests the following guidelines for design of a contouring system:

(1) The object, or an image of the object, should be as close as possible to the hologram plane.

(2) The reference beams should be such that the multiple coherent image points reconstructed for each object point will be contained in as small a volume as possible.

(3) Each object point should receive light from a source small enough to prevent blurring of the contour map.

8.3. OPTICAL CONFIGURATION FOR MFHC

As indicated in Section 8.2 in an ideal optical configuration for MFHC, contouring surfaces are plane, the object-to-hologram distance is minimum, and reference beam compensation is

achieved (i.e., Eq. 35 is satisfied). Varner [73] analyzed the general problem of designing a configuration subject to these criteria. In this section, we present a brief discussion and experimental results for two configurations which meet (at least approximately) these criteria: (1) systems in which the object is physically close to the hologram and (2) systems requiring auxiliary imaging systems.

8.3.1. TWO CONFIGURATIONS WITH NO AUXILIARY IMAGING SYSTEMS

When the object is placed very close to the recording (hologram) plane, it is generally difficult to supply an appropriate reference beam and object illumination. In this section, we discuss two configurations by which appropriate reference and object illumination can be supplied. In the first, the offset angle between the object and reference beams is less than 90°; in the second, it is greater than 90°.

8.3.1.1. A Tilted Contouring Plane Configuration

This configuration is illustrated in Fig. 47. The object illumination beams corresponding to the two frequencies are collimated and parallel $(\bar{a} = \bar{b})$. The line of sight is normal to the hologram $(\bar{c} = \bar{d})$, and the normal to the contour planes $\bar{e}$ bisects the angle between the line of illumination and the line of sight. We choose a set of reference beam propagation vectors $(\bar{f}_i)$ so that the $\bar{f}_i$ corresponding to the shortest wavelength has an offset angle at least as great as the angle the contour planes make with the recording plane. This choice maximizes the hologram area illuminated by the reference beams for a set of contour planes such as those represented by the dotted lines in Fig. 47. If the vectors $\bar{a}$ and $\bar{b}$ are then chosen to be parallel to the hologram plane, the object can be oriented in the desired position relative to the contour planes and translated just until it is simultaneously touching the recording surface and tangent to the reference beams. This allows us to place the object much closer to the hologram than any other configuration with reference beam offset of less than 90° would allow. Experiments were carried out to test this configuration. We had considerable difficulty in obtaining good results; this difficulty seemed to be caused by the roughly two orders of magnitude increase in the average object-to-hologram distance for this configuration as compared to those described below. The need for imaging onto a tilted plane also contributed to this difficulty. The configuration discussed in the next section appears to be preferable to this one.

8.3.1.2. A Configuration with Lippman Process Holography

A sketch of this configuration is shown in Fig. 48. The reference beams pass through the recording medium, illuminate the object, and reflect from it to become the object beams. The compensation problem (i.e., satisfying Eq. 35) is simplest when the reference beams are parallel to the z axis.

72

For most objects for which plane contouring surfaces are appropriate, this configuration will allow the average hologram-to-object distance to be reduced by at least an order of magnitude over the tilted plane technique discussed above. This distance is further reduced by the imaging techniques to be presented in the next section, but at the expense of added optical complexity and aberrations.

The results discussed here were first reported by Varner [74]. As shown in Fig. 49, a laser beam consisting of two different wavelengths (λ_1, λ_2) is expanded and collimated by the usual procedure; the two wavelengths may be present simultaneously, which allows for recording transient events. The collimated beams are then passed through grating (G) which is parallel to the hologram plane (H) and normal to the incident beams. Alignment is performed for both the grating and the hologram plane by retroreflection through the collimation optics. The first-order diffracted beams strike a portion of the recording plane which is shielded from the undiffracted light by the mask (M). The light which passes through the recording material reflects from the object (S) and is recorded by Lippman process holography. The object (S) is oriented as desired and placed as close as possible to the recording plane; the emulsion side of the plate faces the object.

Figure 50 is a contour map of a quarter made with the setup shown in Fig. 49. The He-Ne lines 6118Å and 6328Å were used. This contour map is the best MFGC result (in the sense of image quality and fringe detectibility) obtained to date with a contour interval (D) on the order of 10 μm. In addition to the high quality of the results, the setup of Fig. 49 has the advantage of (1) requiring few optical elements, (2) being very simple to align, and (3) yielding holograms which can be reconstructed in incoherent light. This experiment gave a clear indication of how far previously obtained results were from optimum.

The disadvantages of this technique are those generally attributed to Lippman process holography. These are: (1) an inability to obtain low reference-to-object beam ratios with many objects; (2) a need for increased mechanical stability of the setup; (3) low diffraction efficiency of the holograms; and (4) the problem of emulsion shrinkage. However, none of these disadvantages present a basic barrier to the use of the setup.

8.3.2. CONFIGURATIONS WITH AN AUXILIARY IMAGING SYSTEM

There are two major reasons why an auxiliary imaging system might be used to reduce the average object-to-hologram distance:

(1) We can actually reduce the average object-to-hologram distance to zero by imaging the object so that the recording plane coincides with some plane centered on the object relative to the desired line of sight (along which the distance is measured).

(2) There may be some applications for which the recording plane cannot be physically close to the object.
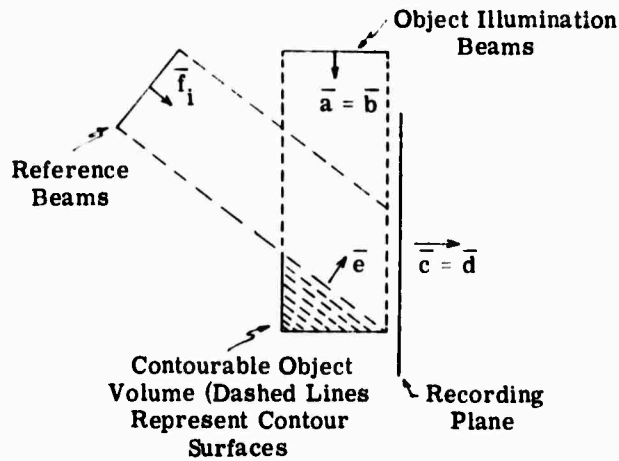
FIGURE 47. CONFIGURATION WITH TILTED CONTOUR
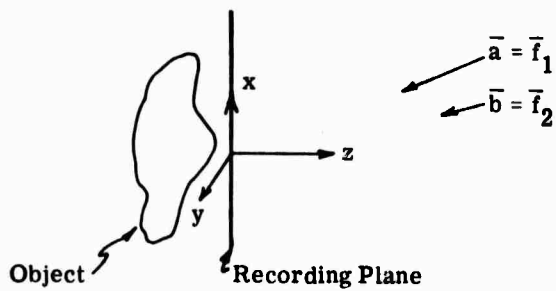PLANES WHICH ALLOWS GREATLY REDUCED OBJECT-
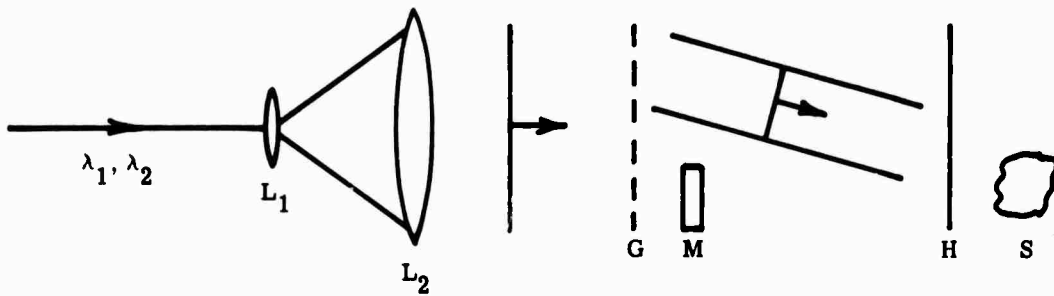TO-HOLOGRAM DISTANCES

FIGURE 48. LIPPMANN PROCESS HOLOGRAPHY

FIGURE 49. LIPPMANN PROCESS MFHC

74

Most of our experimental work was done with the setup shown in Fig. 51 in which a two-lens telescope was used to image a typical object point P_0 to an image point P_1. Our detailed analysis of this system, which included the effect of aberrations by both the telescope and the hologram, is reported in Ref. [73]. The most important result of this analysis, from the standpoint of MFHC, is an expression for the mutual coherence of the total of the image wavefronts with the total of the reference wavefronts. It is shown that this factor is affected only by the chromatic aberrations of the auxiliary imaging system. This fact is illustrated qualitatively by the experimental results presented below; this presentation contrasts the use of a chromatically corrected telescope with the use of a field-corrected telescope. Since the beam splitter used in the telescope configuration described here introduces aberrations (including chromatic) which are directly proportional to the thickness of the beam splitter, we should be able to improve the results considerably either by avoiding the use of the beam splitter or by reducing its thickness to near zero (e.g., by using a pellicle beam splitter). In particular, lateral chromatic aberrations caused by the telescope will be harmful.

NOT REPRODUCIBLE

FIGURE 50. A CONTOUR MAP OBTAINED WITH LIPPMANN PROCESS MFHC. Rms object-to-hologram distance less than 1 mm.
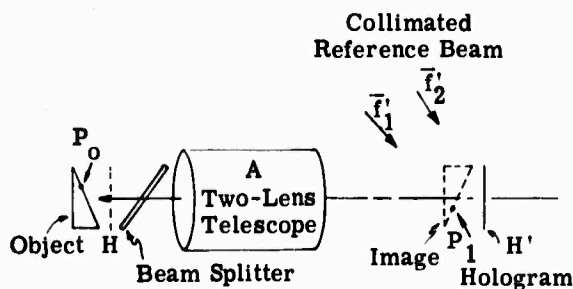

FIGURE 51. MFHC WITH A TELESCOPE

The MFHC configuration sketched in Fig. 51 was first tested and reported by Zelenka and Varner [72]. A Spectra-Physics Model 125 He-Ne laser capable of generating both a red line (λ_1 = 6328 Å) and an orange line (λ_2 = 6118 Å) was used. The object used was a Kennedy half-dollar coin mounted on four flat surfaces, each of which had a slightly different angular orientation. The lateral extent of the object on which fringes were obtained was about 10 cm by 8 cm. Unlike the technique of Haines and Hildebrand [68, 69] there is no theoretical limit on the lateral extent of the object which can be contour-mapped by this technique; the limitations are imposed by the useful apertures of the imaging system and by the collimating lenses used. The experiments were carried out by the real-time, holographic, interferometry procedure.

Figure 52 is a result obtained by the use of a telescope with a demagnification of 2 and an f-number of 50. The depth contours can be seen on the four flat surfaces as well as on the coin. The curvature associated with the contour fringes located at the extremities of the photograph was initially attributed to aberrations introduced by the collimating lenses used to illuminate the object and to provide the reference beams. More recent work has indicated that this anomalous curvature is largely caused by chromatic aberrations in the telescope and beam splitter.

To illustrate the harmful effect of speckle, an enlargement of the central portion of a MFHC result is shown in Fig. 53. Speckle is an unfortunate inherent feature of coherent imagery. When the bandwidth of the speckle is much greater than that of the desired image, several techniques (e.g., mixed integration [75] or incoherent summation) are available for reduction of problems caused by speckle. However, as illustrated in Fig. 53, speckle is most bothersome when the bandwidth of the contour fringe frequency is roughly equal to the bandwidth of the speckle. It might be added that the implementation of mixed integration into MFHC tends to be very cumbersome.

8.4. REDUCTION OF REFERENCE-BEAM NOISE IN IMAGE PLANE HOLOGRAPHY

8.4.1. INTRODUCTION

As indicated in the preceding sections, a number of improvements have been made in holographic contouring, which are based on the use of image plane holography. In spite of the advantages of this type of holography for contouring, it is well known that image plane holography is highly susceptible to noise, either from the illuminating and imaging system or from the reference beam. This discussion will not be concerned with noise in the object branch of the hologram setup because (1) the diffusely reflecting objects used in hologram contouring greatly reduce the effects of noise in the imaging system, and (2) the remaining noise cannot be removed with the use of film effects without similarly affecting the signal.

This investigation was prompted by the discovery that the effects of reference-beam noise on the reconstructed image varied a great deal depending on the ratio of beam intensities and on the average exposure of the hologram.

Figure 54 shows two contour maps of a quarter in which the beam ratios and average exposures were quite different. Obviously, reference-beam noise is a very serious problem, but it can be reduced by choosing the proper beam ratio and average exposure. Leith [76] discussed this problem and concluded that reference-beam noise can be reduced by biasing the recording film at a nonlinear portion of its amplitude-transmittance-versus-exposure curve.

8.4.2. THEORY

Using film exposure data obtained from Upatnieks and Leonard or our laboratory, we computed diffraction efficiency as a function of reference-beam exposure for various signal-beam exposures. Upatnieks and Leonard found a function which gives a very good fit to the experimental data for Agfa-Gevaert 10E70 plates developed for 12 min in Metinol-U. This function is

$$T_A = \exp -cE^2 \tag{36}$$

where T_A is the amplitude transmittance, E is the film exposure in erg/cm^2, and c is a constant which gives the best fit $\left[c \text{ was found to be } \frac{1}{930} \frac{(cm)^4}{(ergs)^2} \right]$.

Assuming that two plane waves strike the film, one has

$$E = E_0 + S + 2\sqrt{E_0 S} \cos x \tag{37}$$

where E_0 and S are the reference- and signal-beam exposures, respectively, x is a coordinate lying in the plane of the film, and $\cos x$ represents the interference fringes with unity spatial frequency assumed (making this assumption involves no loss of generality). Once the film is exposed and developed, it can be illuminated normally with a plane wave of unit amplitude so that the amplitude of the transmitted wave is given simply by T_A. Then if we represent T_A by a Fourier cosine series, we can associate the first harmonic and second harmonic with the first- and second-order diffracted beams. In other words, the Fourier coefficient equals the square root of the diffraction efficiency of the corresponding diffracted order. These coefficients are computed by the following integral

$$A_n = \frac{2}{\pi} \int_0^\pi T_A \cos nx \, dx \tag{38}$$

Because of the difficulty in the integration, it was performed numerically on a digital computer. The results are shown in Fig. 55.
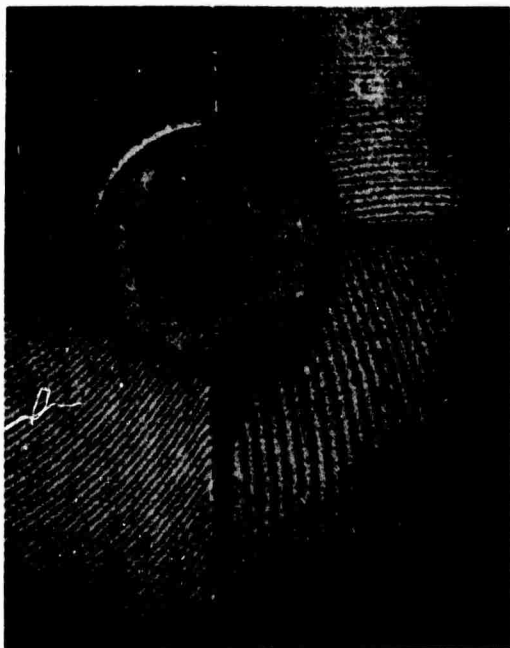
FIGURE 52. DEPTH CONTOURS OBTAINED
WITH AN AUXILIARY TELESCOPE LIKE
THAT SHOWN IN FIGURE 51

FIGURE 53. AN ENLARGEMENT OF THE
CENTRAL PORTION OF FIGURE 52 SHOW-
ING SPECKLE EFFECT

NOT REPRODUCIBLE

(a) One of the Initial Results with Image-
Plane Hologram Contouring

(b) A Result from the Use of Different
Average Exposure and Beam Ratio

FIGURE 54. EFFECTS OF REFERENCE-BEAM NOISE

The curves plotted represent normalized intensities diffracted into the first order, λ_1, as a function of reference-beam exposure, E_0, for constant signal-beam exposure, S, (the terms signal and reference refer simply to the less intense and the more intense beam, respectively). These curves indicate that, for signal-beam exposures between 1 and 8 erg/cm^2, the reference-beam exposure can vary by ±25% from its peak value of about 25 erg/cm^2 with a maximum change of only 10% in the intensity of the reconstructed beam. It is also important to note that, as shown in Fig. 56, the response to signal-beam exposure variation is strong, but locally it is reasonably linear in this entire range. It is quite possible that the response to the reference-beam variations would also be very low for E_0, well beyond the peak value; but in this region, the diffraction efficiency is probably very low, and the response to signal-beam variation is also considerably decreased. Experiments were performed to verify these predictions. The results are given in Section 8.4.3.

8.4.3. EXPERIMENTAL RESULTS

The experimental results support, at least qualitatively, the results given in Fig. 55. The holographic setup shown in Fig. 57 was used. On each hologram, an effort was made to obtain at least seven points on a curve which corresponded to the curves in Fig. 55. In other words, a uniform signal-beam exposure was mentioned, while seven or more reference-beam exposures were made.

The component T_1 in Fig. 57 represents a telescope beam expander used to make the inputs to LP_1 and LP_2 as uniform as possible, except for higher frequency noise such as that caused by dust on the preceding optical components. LP_1 and LP_2 represent the usual lens-pinhole components which are used to decrease the effects of the higher frequency noise. Particular care is taken with LP_2, since it is to provide a very uniform signal beam. Once a good point source has been obtained with the use of LP_2, polarizer A_1* is placed in the beam with its polarizing axis parallel to that of the laser beam. Polarizer P_1 precedes A_1 and is rotated to vary the signal-beam intensity. In the reference-beam branch, LP_1 is followed by a collimating lens L_1, a step wedge attenuator, and a telescope which images the step wedge onto the recording plane with unity magnification. The steps of the wedge are numbered from 9 to 18, and one tries to center the exposure from step 14 on the peak diffraction efficiency for any given signal-beam exposure. Reference-beam noise in the form of the diffraction pattern of a hair placed in the plane of lens L_3 is caused to fall on each of the steps. One would expect that the reconstructed signal beam would show additive noise caused by the hair, but also that this noise would be least visible on the step (which should be step 14) of peak diffraction efficiency. An additional effect is that the noise should be seen as a positive on one side of the peak and as a negative on the other. These predictions are borne out by the results shown in Fig. 58.

---

*One would usually place both of these polarizers in the beam before the lens-pinhole LP_2, but here the low quality of these polarizers was found more acceptable in the expanded beam.
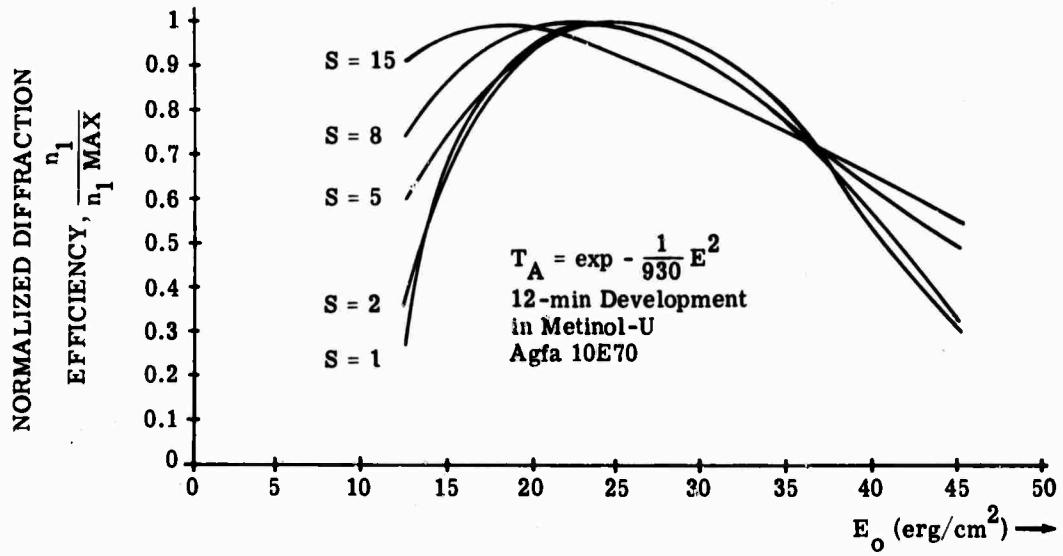
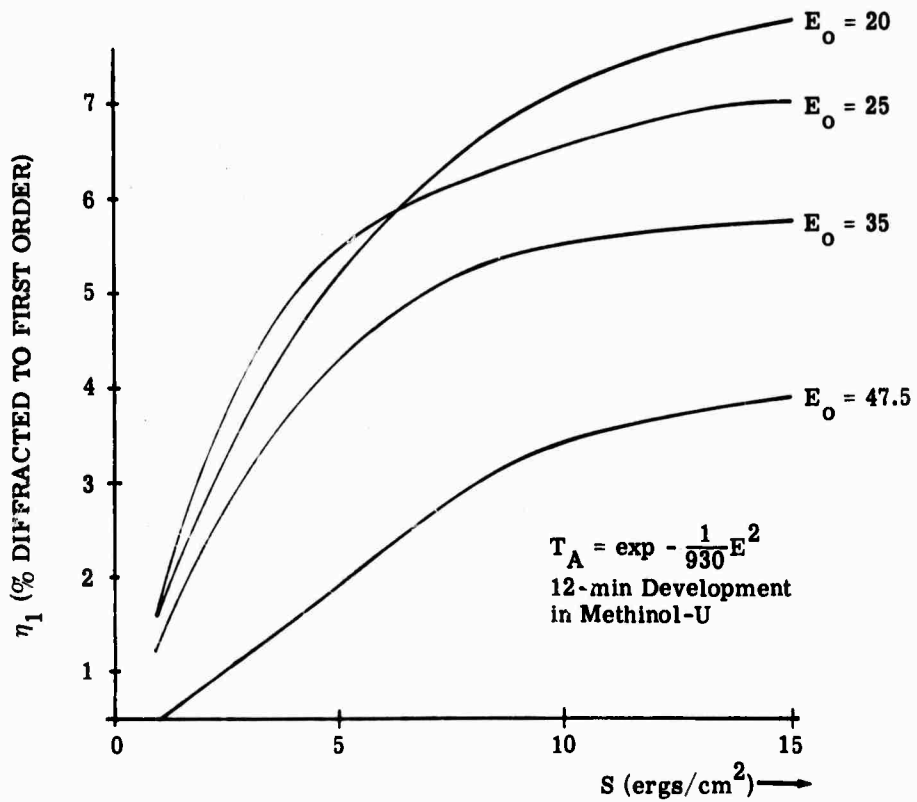FIGURE 55. COMPUTED NORMALIZED DIFFRACTION EFFICIENCY

$T_A = \exp - \frac{1}{930} E^2$

12-min Development
in Metinol-U
Agfa 10E70

$T_A = \exp - \frac{1}{930} E^2$

12-min Development
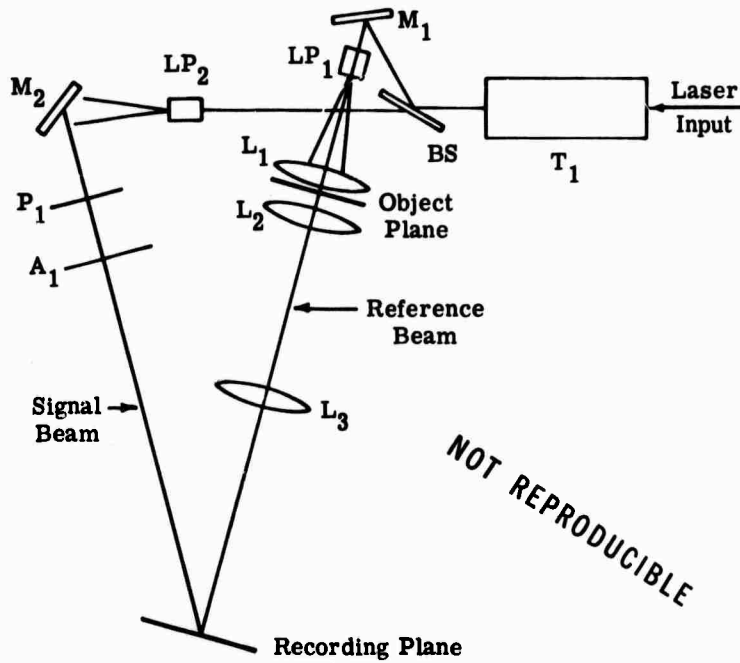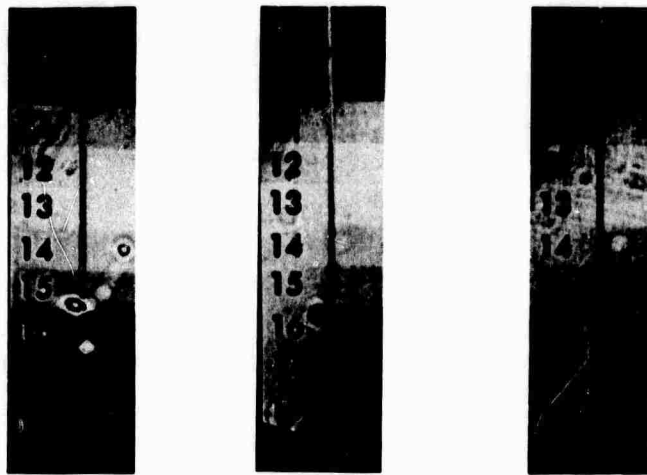in Methinol-U

FIGURE 56. COMPUTED DIFFRACTION EFFICIENCY

80

FIGURE 57. HOLOGRAPHIC SETUP FOR TESTING FILM EFFECTS
IN REFERENCE-BEAM-NOISE REDUCTION

(a) $S = 1$ erg/cm^2 (b) $S = 8$ erg/cm^2 (c) $S = 15$ erg/cm^2

FIGURE 58. EXPERIMENTAL RESULTS IN REFERENCE-BEAM-NOISE REDUCTION.
Reference-beam changes are monotonically increasing by 33%/step from 9 to 18. The
hair is in the vertical strip in the center.

8.5. VARIABLE -SENSITIVITY HOLOGRAPHIC INTERFEROMETRY

8.5.1. INTRODUCTION

Previously, we have shown hologram interferometry to be a useful technique for determining displacement fields of diffusely reflecting objects. Extremely sensitive, the method is capable of measuring displacements of the order of 0.3 μm. It is obvious that for many applications which require the measurement of displacements of the order of millimeters or centimeters, standard hologram interferometry is, in fact, too sensitive to be useful, since the fringes become too fine to resolve. Therefore, we have conducted an experimental and theoretical study of the use of multiple-wavelength holography to perform desensitized hologram interferometry. Desensitized hologram interferometry should be useful for studying objects subjected to large deformation by static loads, steady-state vibrations, or transient events of many types. A short analysis of one of the simplest possible static loading cases has been completed, and experiments have been performed to support the conclusions of this analysis.

Both the analysis and the experiments are concerned with cases in which all object point displacements are assumed to be in one direction between two fringes corresponding to a displacement sensitivity on the order of $\lambda/2$. By using multiple-wavelength holography, we have demonstrated a displacement sensitivity on the order of $(\lambda_1\lambda_2)/(2\lambda_2 - \lambda_1)$; the quantity $(\lambda_1\lambda_2)/(2\lambda_2 - \lambda_1)$ is never smaller than $\lambda_1/2$, where λ_1 is less than λ_2.

8.5.2. THEORY

The optical setup shown in Fig. 59 was analyzed and used in our experimental work. A contour map of the surface of an object can be produced by reconstructing a double-exposure hologram of the object. The immersion tank is filled with fluids of known, but different refractive indices during each exposure. The illumination system is carefully aligned to illuminate the tank normal to its transparent side with a collimated beam. The viewing system is arranged so that each object point can be seen only by light rays reflected almost parallel to the illumination beam. It is convenient to select a coordinate system with its origin at the intersection of the optical axis and the inner surface of the immersion tank. The x-y plane is taken to lie in the plane of the inner surface; the z axis is therefore parallel to both the illumination beam and the line of sight. Thus, it is effectively the axial optical path length traversed from the inner surface of the tank to the object and back which changes between exposures.

Reconstructing the hologram, we have two wavefronts interfering in the image plane of the viewing system

$$U_I = S_1(x, y) \exp j2k_1 z(x, y) + S_2(x, y) \exp j2k_2 z(x, y) \tag{39}$$

where U_I is the sum of the complex amplitudes of the two reconstructed wavefronts at the image plane; $S_1(x, y)$ and $S_2(x, y)$ are directly related to the object brightness at (x, y) for the
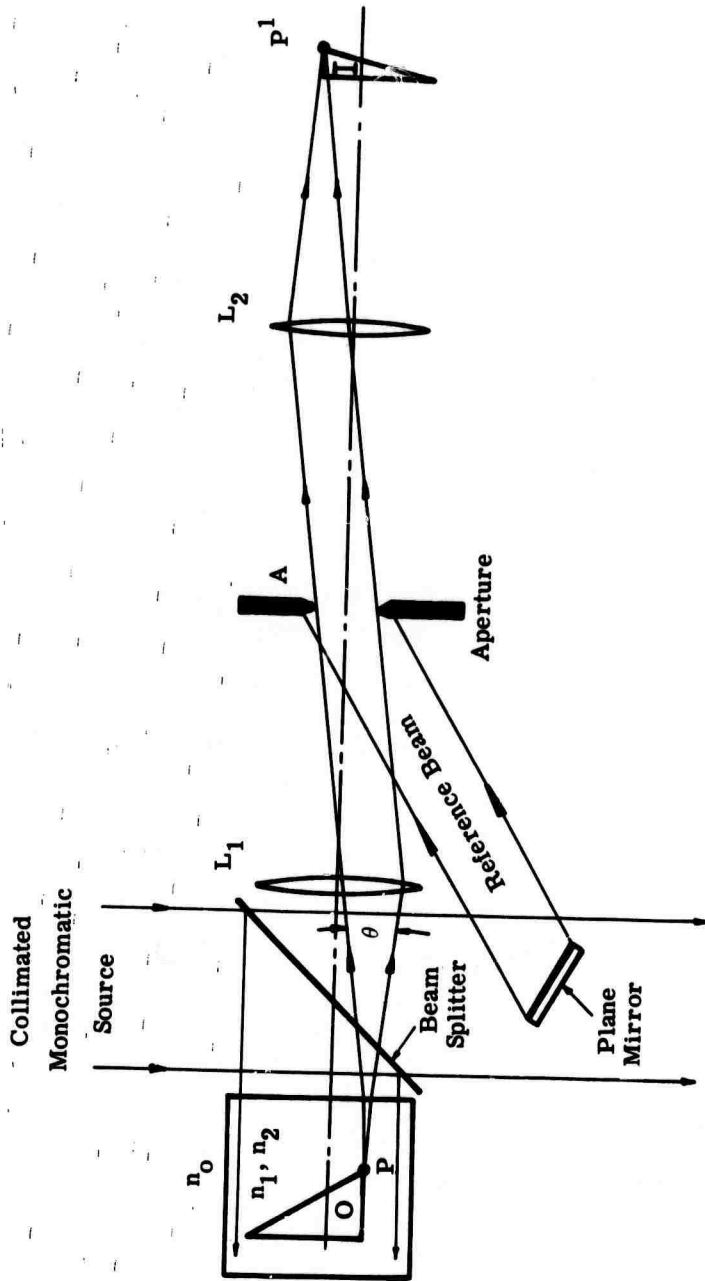
82

FIGURE 59. A SYSTEM FOR GENERATING DEPTH CONTOURS BY THE MULTIPLE-INDEX METHOD

two different exposures; k_1 and k_2 are the respective wave numbers for the two different fluids; and $z(x, y)$ is the axial coordinate of the object point at (x, y).

In practice, $S_1(x, y)$ and $S_2(x, y)$ are almost identical. By using a uniform illumination beam and by treating the object surface (in any permissible way) to make it diffusely reflecting, we can usually make S_1 and S_2 very slowly varying functions. This procedure places the contour fringes on a much less confusing background. Thus, we arrive at the intensity of the image

$$|U_I|^2 = 2S_1^2[1 + \cos 2(k_2 - k_1)z(x, y)] \tag{40}$$

Thus, for any set of lateral object coordinates (x^*, y^*), the reconstructed image brightness is modulated according to the axial coordinate as shown by the above expression for $|U_I|^2$. The overall result is a depth contour map of the object.

The simple analysis we have performed is concerned with measuring a displacement along the axis (i.e., Δz). We can do this by making two depth contour maps of the object; the displacement of any point can then be found by fringe counting. But since fringe counting could be very tedious, we would prefer to find some convenient means of getting a direct display of the displacement information. One means of obtaining such a display is to overlay the two contour map transpariencies to produce a moiré fringe pattern; this would often be satisfactory. Adding the two contour maps, we obtain

$$|U_{I1}|^2 + |U_{I2}|^2 = S_1^2[4 + 2\cos 2\Delta kz_1(x, y) + 2\cos 2\Delta kz_2(x, y)] \tag{41}$$

$$|U_{I1}|^2 + |U_{I2}|^2 = 4S_1^2[1 + 1\cos \Delta k\Delta z \cos \Delta k\Sigma z] \tag{42}$$

where $\Delta k = k_2 - k_1$, $\Sigma z = z_2 + z_1$, and $\Delta z = z_2 - z_1$.

In some cases, one might find considerable advantage in making a four-exposure hologram, thus eliminating any errors in the moiré fringe pattern which might be caused by misalignment of the two contour maps. From the four-exposure hologram we reconstruct

$$U_{I1} + U_{I2} = S_1(\exp i2k_1z_1 + \exp i2k_2z_1 + \exp i2k_1z_2 + \exp i2k_2z_2) \tag{43}$$

The intensity of the image in this case is of the form

$$|U_{I1} + U_{I2}|^2 = 4S_1^2\left[1 + \frac{1}{2}\cos \Sigma z\Delta k \left(\cos \Sigma z\Delta k + \cos \Sigma k\Delta z\right) + \frac{1}{2}\cos \Sigma z\Delta k \cos \Sigma k\Delta z\right] \tag{44}$$

The factor of interest (in both cases) is

$$\cos \Delta k\Delta z$$

which has a period of $(\lambda^2/\Delta\lambda)$. This factor gives the densitized interferometry information. The term $\cos \Delta z\Sigma k$ corresponds to an average contour modulation, and $\cos \Sigma z\Delta k$ corresponds

84

to an average hologram interferometry modulation.

The above expression for $\left|U_{I1} + U_{I2}\right|^2$ assumes that the interference between the four terms is independent of the fine surface structure of the object. Further analysis is needed to test this assumption; a basic question remains to be answered: whether or not the reflected wavefront from the object resolution cell seen at (x^*, y^*) in one load condition and the reflected wavefront seen at (x^*, y^*) in the second condition are correlated within the depth of field of the optical viewing system. If not, then no meaningful interference could take place to indicate the object displacement by the usual hologram interferometry. We would then obtain the same expression as that for overlaying two contour map transparencies

$$\left|U_{I1} + U_{I2}\right|^2 = 4S_1^2(1 + \cos \Delta z \Sigma k \cos \Sigma z \Delta k) \tag{45}$$

Before the surface correlation question and others can be answered, object shapes, surface structures, and displacements will have to be categorized. From these categories, definite statements can be made about the advantages of desensitized hologram interferometry.

8.5.3. EXPERIMENTAL RESULTS

We chose a simple object, a cantilever beam, for our first experiments with desensitized hologram interferometry. The multiple-index-contouring technique was used because of its simplicity and its available range of contouring intervals.

Figure 60 shows a clear set of densensitized fringes on the cantilever beam (the beam is about 1/16 in. thick, 3/4 in. wide, and 4 in. long). Load condition 1 had a total end-to-end displacement of about 1/4 in., and we counted about 100 contour fringes end-to-end. By counting moiré fringes, we see that condition 2 had 16 more (or fewer since an ambiguity exists without previous knowledge) fringes. The end displacement was actually about 3/40 in. Thus, the experimental value for the equivalent wavelength is

$$\frac{\lambda_{eq}}{2} \cong \frac{3/40}{16} \cong \frac{3}{640} \cong \frac{1}{210} \cong 0.005 \text{ in.} \tag{46}$$

whereas

$$\frac{\lambda}{2} = \frac{0.63 \,\mu\text{m}}{2} = 0.31 \,\mu\text{m} = 0.000015 \text{ in.}$$

which indicates a desensitization factor of 300.

The two liquids used in obtaining the result shown in Fig. 60 were water and a 12% solution of ethyl alcohol in water. The refractive index of water is about 1.33 and that of ethyl alcohol is about 1.36. The difference is 0.03, about one-tenth of which was assumed to exist between water and the 12% solution. Thus,

$$\frac{\lambda}{\Delta n} = \frac{\lambda}{0.003} = 333 \tag{47}$$

where λ is the light wavelength in air. As previously stated, the contouring interval is

$$\frac{\dfrac{\lambda^2}{n_1 n_2}}{\dfrac{\lambda}{n_1} - \dfrac{\lambda}{n_2}} = \frac{\lambda}{\Delta n} \tag{48}$$

Thus, we find that our tacit assumption of a linear variation of refractive index with percentage of concentration was good for small percentages. Of course, in practice, we would want to know the refractive indices more accurately.

We can increase the moiré fringe contrast by recording the contour maps on higher contrast film and, sometimes, by using optical spatial filtering. The result shown in Fig. 60 was obtained by making four exposures on one hologram with the same reference wavefront. Figure 61 shows the moiré fringes in much higher contrast after spatial filtering; the large speckle effect is caused by the low pass filter used in this case. The fact that we could observe no indication of the extra terms predicted in Eq. (44) would imply either that the extra terms were of too high a spatial frequency to be resolved or that (because of an addition of the uncorrelated, surface-structure images) the extra terms did not exist in the region of focus. When we tried to repeat this experiment with ordinary hologram interferometry, we could observe fringes only in the area of minimum displacement very near the clamped portion of the cantilever beam. The expected average spatial frequency of the fringes was about 50 lines/mm, and our optical system had a resolution capability on the order of 200 lines/mm; therefore, we think the lateral surface-structure displacement may have been the important factor in this case. However, we would have to do more work in this interesting area to make conclusive statements.

The result shown in Fig. 60 was for two very similar contour maps. Figure 62 on the other hand, shows a result for two very different contour maps. The moiré fringes are quite hard to see in this photograph; but in the region of minimum displacement, they are visible. An extreme example of very different contour maps is obtained when a flat object normal to the z axis is loaded and unloaded; the contour map of the loaded object, then, is the desensitized fringe system.

8.5.4. CONCLUSIONS

Although this work is rather preliminary, we can conclude that desensitized hologram interferometry holds promise for extending the range of applications of hologram interferometry.

86

FIGURE 60. DESENSITIZED HOLOGRAM INTERFEROMETRY: VERY SIMILAR SHAPES
AFTER DISPLACEMENT

FIGURE 61. DESENSITIZED HOLOGRAM INTERFEROMETRY: RESULTS SHOWN IN FIGURE
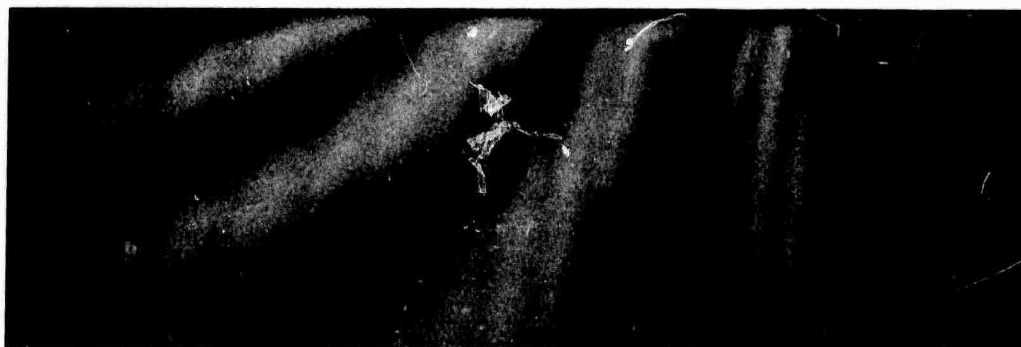60 AFTER SPATIAL FILTERING

FIGURE 62. DESENSITIZED HOLOGRAM INTERFEROMETRY: VERY DIFFERENT SHAPES
AFTER DISPLACEMENT

8.6. A COMPARISON OF VARIOUS OPTICAL-FIELD-CONTOURING TECHNIQUES

8.6.1. SOME COMMON CHARACTERISTICS OF THE OPTICAL-FIELD-CONTOURING TECHNIQUES

The objective of any contouring technique is to form an image of the object overlaid with a set of contour lines. The optical-field-contouring techniques measure the necessary distances to all the object points simultaneously rather than the distance to one point (or one subset of points) at a time, as is done by mechanical probing, optical focusing, and optical-impulse-ranging methods.

All of the contouring techniques discussed here have certain features in common. For instance, all of them require that the object be opaque and somewhat diffusely reflecting. The use of a translucent object results in very low contrast fringes in most cases; the reduction in contrast is apparently caused by a multiplicity of optical paths from the object source to the object point and back to the observer. A diffuse reflector is advantageous because it tends to make the object brightness independent of the illumination and viewing angles. Typically, a surface coating is applied to an object that is not sufficiently opaque and/or diffuse. The use of such coatings is, of course, prohibited in many applications. These contouring techniques are also limited in sensitivity, acceptable object size, and distance from a key optical element to the object. In addition, they all require careful alignment and accurate orientation of the object with respect to the optical contouring system.

8.6.2. MULTIPLE-INDEX HOLOGRAPHIC CONTOURING

8.6.2.1. Theory

The multiple-refractive-index technique [71-72] is quite similar to multiple-frequency contouring. Indeed, the holographic setup shown in Fig. 59 is just a modification of that depicted in Fig. 51. Because only one laser frequency is used, the holographic aberrations are largely eliminated; and the setup shown in Fig. 59, may in fact, be unnecessarily expensive, since the importance of the telescope is greatly reduced.

If a diffuse object placed in a transparent box which contains a fluid, the refractive index of which is considerably different from that exterior to it, the simplest light rays to consider are those which are nearly perpendicular to the front surface of the box. Thus, the object illumination geometry shown in Fig. 59 is a natural one to consider. The beam splitter allows the object illumination as well as the useful portion of the backscatter from the object to pass through the front surface of the box at nearly normal incidence The lenses, L_1 and L_2, constitute a telescope with its axis normal to the front of the box.

The aperture, A, allows only those light rays through the telescope which are nearly perpendicular to the front surface of the box. In particular, images result from light rays which,

88

at the boundary of the box, make a small angle with respect to the axis of the telescope. Thus, the aberrations introduced at the boundary are reduced, since small angle approximations are valid. The medium outside the box has an index, n_0, which can usually be approximated by unity.

To obtain range contours (actually depth contours) with the configuration shown in Fig. 59, an off-axis hologram is first constructed anywhere to the right of the beam splitter, while the object is immersed in a fluid of known index, n_1. Then the geometry of Fig. 59 is maintained, while the fluid in the box is replaced by one with a known but different index, n_2. If the telescopic image of the object together with that formed by the normal wavefront emanating from the hologram are viewed or photographed simultaneously, the resulting image is superposed with constant depth contours.

Let us now turn our attention to the actual location of the depth contours. As the index about the object is changed from n_1 to n_2, the phase at the image plane of the telescope changes by an amount equal to

$$\Delta\phi = \frac{2\pi}{\lambda} \left| n_1 - n_2 \right| 2z \tag{49}$$

where z is the distance from the hologram to a point on the object. The distance between successive depth contours occurs when the differential phase, $\Delta\phi$, changes by an amount, 2π. Thus, the spacing of the depth contours is given by

$$D = \frac{\lambda}{2} \left| n_1 - n_2 \right| \tag{50}$$

The wavelength of light inside the box is either

$$\lambda_1 = \frac{\lambda}{2} \left| n_1 - n_2 \right| \quad \text{or} \quad \lambda_2 = \frac{\lambda}{n_2} \tag{51}$$

depending on which medium is present. Eliminating n_1 and n_2 by inserting (51) into (50), we find

$$D = \frac{\lambda_1 \lambda_2}{2 \left| \lambda_1 - \lambda_2 \right|} \tag{52}$$

which is the same expression obtained for depth contouring with a two-frequency source.

A very close analogy exists between multiple-refractive-index holographic contouring and MFHC. A useful and simple illustration of this analogy is given by considering a collimated beam of coherent light which strikes a plane boundary between two media of different refractive indices. Let the angle of incidence be θ_0. By Snell's law

$$k_0 \sin \theta_0 = k_1 \sin \theta_1 \tag{53}$$

where θ_1 is the angle between the boundary normal and the plane wave on the other side of the boundary. When the refractive index is changed on one side of the boundary, we find

$$k_0 \sin \theta_0 = k_1 \sin \theta_1 = k_2 \sin \theta_2 \tag{54}$$

Thus, any object inside the medium is illuminated by plane waves at angles compensated according to (35). This implies that plane-contouring surfaces are automatically available whenever plane-wave illumination is used. If a given object is perfectly diffuse, we could conceivably collect light over a very wide viewing angle. If the centroid of the viewing cone of light is normal to the boundary, the lateral distortion goes to zero, and an object point at (x, y, z) has Gaussian images at $(x, y, \frac{n_0}{n_2} z)$ in the two different fluids. The magnitude of the longitudinal shift is therefore

$$\Delta z = z \frac{n_0}{\lambda_0} \left| \lambda_2 - \lambda_1 \right| \tag{55}$$

where λ_2 is λ_0 / n_2, λ_1 equals λ_0 / n_1, and λ_0 is the wavelength for n_0. This expression is very similar to that obtained for MFHC with plane-contouring surfaces when the reconstruction temporal frequency differs from either of the recording frequencies. Thus, for multiple-index contouring, both of the interfering coherent images will suffer from distortion and aberrations. Using Eq. (55), we can obtain a constraint on object surface orientation and distance from the boundary. This constraint for MFHC takes the form

$$z \tan^2 \beta \leq \frac{D^2}{n_0 |\Delta \lambda|} \tag{56}$$

8.6.2.2. Experimental Results

The contour maps for comparison of the multiple-index technique with MFHC are shown in Fig. 63, in which the contouring intervals are roughly equal. The two media used were water and ethyl alcohol, and the depth-contouring interval is $\lambda_0 / (2 |n_1 - n_2|)(11.8 \ \mu m)$. This result is clearly similar in quality to the corresponding MFHC result. The multiple-index technique has two important advantages over the multiple-frequency method. First, it is much easier to apply. Second, a wide and continuous range of contour intervals is available. Figure 64 shows a multiple-index contour map of a complicated object, a dental casting. The contour interval is approximately 0.3 mm.

8.6.3. MULTIPLE-SOURCE CONTOURING

Multiple-source contouring is one of the simplest of the contouring methods. The multiple-source method generally involves the illumination of an object by two or more coherent point light sources. A typical setup is shown in Fig. 65; this setup, used by Hildebrand [70], made use

90

(a) 11.8 μm (Two-Index Method)

(b) 9.25-μm MFHC Result

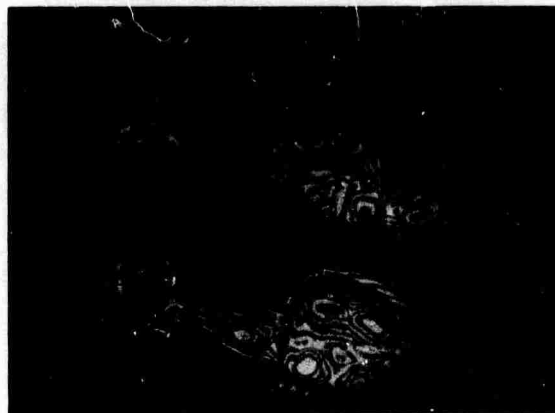FIGURE 63. DEPTH CONTOURS DENOTING CHANGES

NOT REPRODUCIBLE

FIGURE 64. MULTIPLE-INDEX CONTOUR
MAP OF SEGMENTS OF A METAL CAST OF
A LOWER DENTAL ARCH (D $\cong$ 1/3 mm)

of double-exposure holography and a movable light source. However one actually obtains the
multiple sources, the intensity of the resulting image of the sources is dependent upon positions
of the sources. The intensity-modulation function depends only upon the location of the two point
sources. Basically, the intensity-modulation function is the magnitude of the mutual coherence
function between the two points. The volume of the object space over which fringes can be gener-
ated is a function only of the size and temporal spectrum of the sources. Maximum sensitivity
is obtained when the line-of-sight vector is normal to the bisector of the angle between the illumi-

nation vectors. For two point sources, the contour interval is

$$D \approx \frac{\lambda}{2 \sin \frac{\theta}{2}}$$

(57)

where θ is the angle between the two beams striking the object. In the result given by Hildebrand [70], shown in Fig. 66, the contouring interval is about 2 mm. The chief limitation of the method is the shadowing, as seen in Fig. 66. Specular objects are also generally more difficult to work with than with any of the other methods. Whenever an object is suitable, however, the technique is very powerful. The range of contouring intervals is continuous and wider than with any of the other methods. Very large objects can be contoured with relatively little equipment [77] and, perhaps more important, the method gives real-time results (except for the holographic variations).

8.6.4. MOIRÉ FRINGE CONTOURING

8.6.4.1. Discussion

In terms of simplicity and real-time operation, the moiré-fringe-contouring method [78] may well be the most desirable contouring technique for many applications. A major advantage is that coherent light is not necessary. In fact, coherent light can sometimes decrease the quality of the contour map. There are many variations of the moiré contouring method; however, we will restrict our attention to the simple system shown in Fig. 67. The only equipment required for this system is an approximate point source of temporally incoherent light and an amplitude line grating. The object is placed as close as possible to the grating, and the combination is illuminated by the light source at some angle, θ, with respect to the normal to the grating plane. Focusing on some plane between the object and the grating, the viewer sees the grating and its shadow on the object simultaneously. The moiré beat between the two patterns yields the contour map. It is not necessary that the viewer resolve the grating in order to observe the contour map; however, it is necessary that the two patterns have reasonably high modulation depth. If plane-wave illumination and normal viewing are assumed, the contour interval is simply

$$D = \frac{d}{\tan \theta}$$

(58)

where d is the period of the grating.

Suppose the effective illumination source subtends a small angle, α, at the grating. The sharpness of the shadow cast can be seen to be reduced by the penumbra as the object surface is further from the grating. Note that the location of the grating plane is critical as is the location of the hologram plane in MFHC and the location of the media boundary in the multiple-index technique. If the grating period is less than about 100 wavelengths of light, one can find an approxi-

He-Ne Laser

Hologram

Beam Splitter

Lens Pinhole
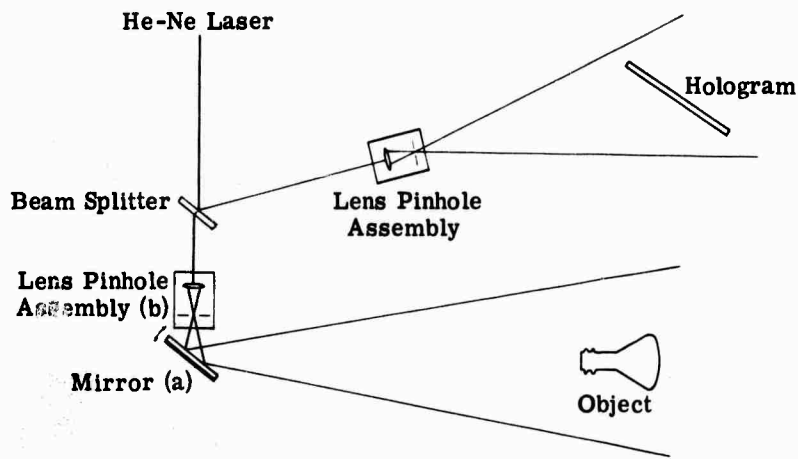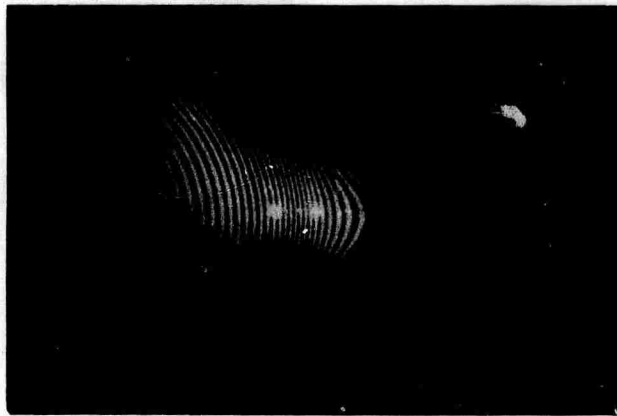Assembly

Lens Pinhole
Assembly (b)

Mirror (a)

Object

FIGURE 65. GEOMETRY FOR MULTIPLE-SOURCE, HOLOGRAPHIC
CONTOUR GENERATION (AFTER HILDEBRAND). See Ref. [70]. The
geometry can usually be modified to operate in real time.

FIGURE 66. MULTIPLE-SOURCE CONTOUR MAP OF OPAQUE,
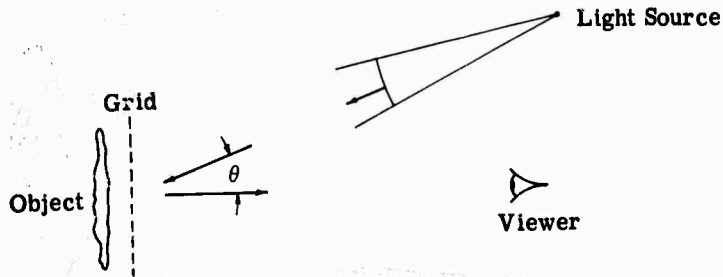DIFFUSE FLOOD LAMP (AFTER HILDEBRAND). See Ref. [70].
(D ≈ 2.2 mm)

Light Source

Grid

Object

θ

Viewer

FIGURE 67. GEOMETRY FOR MOIRÉ CONTOURING

mate, maximum allowable distance from the object to the grating plane by geometrical optics. Another critical consideration is the minimum allowable f-number, since the technique depends on a sharply defined illumination pattern which is then multiplied by a transmission pattern to produce the moiré effect. When the effective viewing aperture at the grating for a given object surface element includes more than one period of the grating, the moiré visibility will be significantly decreased no matter how sharply defined the shadow pattern is. This constraint can be expressed as

$$\frac{z}{f} \leq d \tag{59}$$

where the line of sight is normal to the grating. The shadow sharpness constraint can be written

$$z\alpha \leq \frac{d}{4} \cos \theta \tag{60}$$

Combining the two constraints

$$z \leq \frac{d}{2}\sqrt{\frac{f}{\alpha}} \cos \theta \tag{61}$$

We would expect that this would be the form of the constraint on object-to-grating distance, but that some multiplicative factor would have to be determined experimentally.

8.6.4.2. Experimental Results

To show an example of the moiré-fringe-contouring technique, the contour map shown in Fig. 68 was recorded. A Ronchi grating of 5 lines/mm was used with the illumination angle, θ, equal to 70°. This gives

$$D \cong \frac{d}{\tan \theta} \cong 68 \ \mu m$$

The light source used was an unfiltered mercury arc which was focused onto a small (2-mm-diameter) aperture and approximately collimated by a 15-cm focal length lens. The source angle, α, was therefore about 0.01 rad. For the result in Fig. 68, the coin was actually in contact with the grating. To show the effect of moving the object away from the grating, the contour maps in Fig. 69 were generated. For these maps, the illumination angle was changed to 25° and the effective source angle, α, was changed to 0.005 rad. Object-to-grating distances of one-half, one, two, and four mm, respectively, were used for Fig. 69a through d. Since the contour fringe visibility is significantly reduced at 2 mm and is zero at 4 mm, one can take 2 mm as roughly the maximum allowable distance for this particular grating and geometry. Eq. (61) yields

$$z \leq 0.1\sqrt{\frac{8}{0.005}} \times 0.9 \approx 3.8 \ mm$$

where the photographs were taken at f/8. This result implies that Eq. (61) should be more
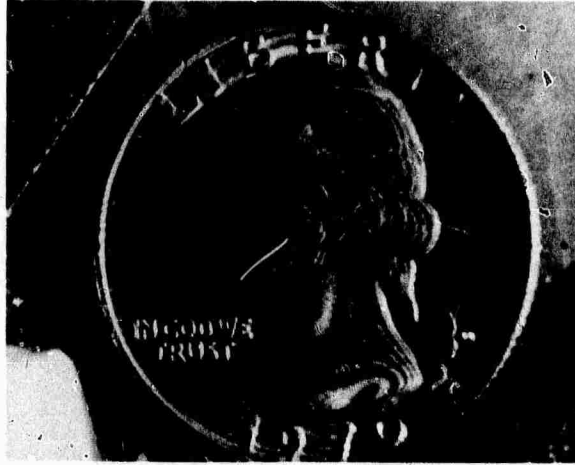
FIGURE 68. MOIRÉ CONTOURING. Grid frequency
5 lines/mm, normal viewing, illumination at 60° from
normal (D ≈ 70 μm)

stringent by a factor of two. We would have to do more research to make a stronger statement about this constraint.

Other researchers have used contouring intervals as small as 25 μm, but have found that the technique becomes exceedingly difficult to apply at about 50 μm. Certainly the contourable, longitudinal extent of the object is greatly reduced at 25 μm. Another reported difficulty is the introduction of extraneous noise-like terms caused by the grating (these terms are called aliasing terms). Further study [79] has shown that this aliasing can be removed by moving the grating as the photograph is recorded; the aliasing terms vary as the grating moves, while the contour fringes are unchanged. Care must be taken that the motion of the grating is in a plane normal to the line of sight. Another disadvantage is that the grating (or grid) must be at least as large as the lateral extent of the object; the construction of a large grid within the necessary tolerances could be very expensive.

8.6.5. CONCLUSIONS

Three alternatives to MFHC have been discussed. Each has been found to have its own advantages and disadvantages. The moiré fringe method has the advantages of simplicity, real-time operation, and a useful, continuous range of contouring intervals. For suitable object shapes, the multiple-source technique is competitive in simplicity and real-time operation. In addition, multiple-source contouring has a wider range of contouring intervals. Unfortunately, as smaller contouring intervals are sought, however, the restrictions on surfaces and shapes become very stringent.

(a) Distance, z = 1/2 mm
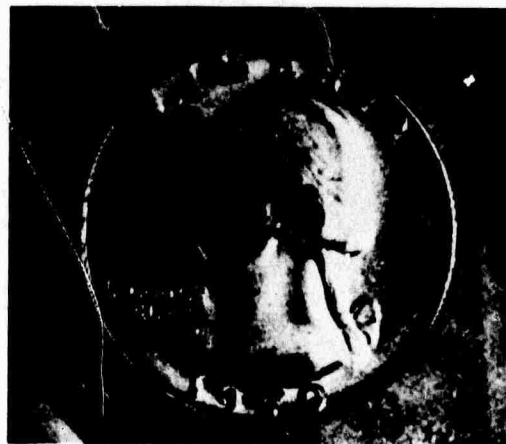
(b) z = 1 mm

NOT REPRODUCIBLE

(c) z = 2 mm

(d) z = 4 mm

FIGURE 69. VARIATION OF MOIRÉ CONTOURING WITH INCREASED OBJECT-TO-GRID DISTANCE

Although it is more complex than the other methods and requires the use of coherent light, MFHC has some unique features. In MFHC, for example, temporal rather than spatial bandwidth is required for information gathering. This is of importance when large f-number imaging systems are necessary (e.g., when fiber optics systems are used). The recent work of Heflinger and Wuerker [80] with pulsed laser MFHC shows that it may be a useful technique for studying transient events. Also, with the development of continuously tunable liquid dye, CW (continuous-wave) lasers will provide a wide, continuous range of contouring intervals for MFHC.

8.7. SUMMARY

We have done considerable basic research which is aimed at improved methods to produce contour maps of surfaces optically. Particular emphasis was placed on a variable-sensitivity technique called multiple-frequency holographic contouring. Several criteria for improving laboratory techniques were developed. A technique was developed for measuring large displacements by forming a moiré pattern between contour maps generated before and after deformation on displacement of a surface. A comparative study was made to determine the practical characteristics and limitations of the various available optical-contouring schemes.

9
HOLOGRAPHIC SURFACE-ROUGHNESS MEASUREMENT

9.1. THEORY AND EXPERIMENT

Whenever two optical wavefronts are superimposed, the resulting light intensity distribution is called an interference fringe pattern because of the mutual reinforcement and cancellation of the light amplitude distribution of the two wavefronts. The contrast ratio of these interference fringes (i.e., ratio of maximum to minimum intensity) is a function of the relative intensity of the two interfering beams and the mutual coherence or cross-correlation of the local phase of the two wavefronts in the plane in which the interference pattern is observed and/or recorded.

This phenomenon of optical interference can be applied to the measurement of the surface roughness of a material. For an understanding of this measurement, it is helpful to refer to Fig. 70. The apparatus shown in Fig. 70 is essentially a Michelson interferometer. The incoming monochromatic light beam is split into two beams. The resulting light components are reflected from a pair of surfaces and recombined to produce an interference pattern in plane P_3. Planes P_1 and P_2 are so inclined that a small number (i.e., 2 or 3) of interference fringes are obtained in plane P_3.

The contrast ratio of these fringes is determined by the ratio of the two light intensities and the mutual coherence or cross correlation between the light amplitude components u_1 and u_2. The latter is influenced by the spatial and temporal coherence of the incident light beam and by

the roughness of the surfaces in P_1 and P_2. If the light source (e.g., spatially filtered laser beam) is sufficiently coherent, the cross-correlation between u_1 and u_2 is determined primarily by the roughness of the two surfaces.

Under this condition, the fringe contrast ratio is determined by the roughness of the two surfaces. If both surfaces are nominally flat (i.e., of the order of the wavelength of the illuminating light source) and one is perfectly smooth (e.g., mirror surface), fringe contrast ratio is uniquely determined by the roughness of the other surface. We can find the roughness of this surface by measuring the interference fringe contrast ratio.

The theory and experimental work on the measurement of the roughness of nominally flat surfaces with the use of the Michelson interferometer has already been reported [81]. It is the purpose of this section to summarize an alternate but similar instrumentation and method for measuring surface roughness, which can be extended to nonflat surfaces. The basis of this method is holographic interferometry.

To understand the application of holographic interferometry to surface-roughness measurement, it is convenient to refer to Fig. 71. In Fig. 71, the object, the surface roughness of which is to be measured, is recorded holographically. For this purpose, the light from a laser is split into two beams. One beam, denoted by u_0, illuminates the object and the other, denoted u_r, is the reference beam for holographically recording the light amplitude u_1 reflected from the object.

A photographic plate is placed in plane P_1 and exposed to the superposition of u_1 and u_r. After it is developed, this plate is a hologram of the object. Whenever it is illuminated by u_r at the proper angle, a portion of u_r is diffracted (the portion denoted u_2 in Fig. 71). This complex, light amplitude distribution is identical to the light amplitude u_1, which is reflected from the object, and carries enough information to form a virtual image of the object.

However, the most significant aspect of light amplitude distribution u_2 is its high correlation with u_1. An interference pattern is formed between u_1 and u_2 whenever the object is illuminated by u_0 and the hologram plate by u_r. The fringe contrast ratio of the interference pattern is a function of the cross correlation and relative amplitudes of the two beams similar to that of the configuration in Fig. 70.

The surface roughness of the object shown in Fig. 71 can be measured by measuring the interference fringe contrast ratio. We can do this most easily by photographing the interference pattern, measuring the density of the developed photograph, and converting the density variations to intensity ratios.

For completeness, we will define surface roughness specifically. Figure 72 is a sketch of the intersection of the surface of a material with a plane normal to the surface, drawn at a greatly enlarged scale. The random variations of the surface are apparent in this sketch. A surface-
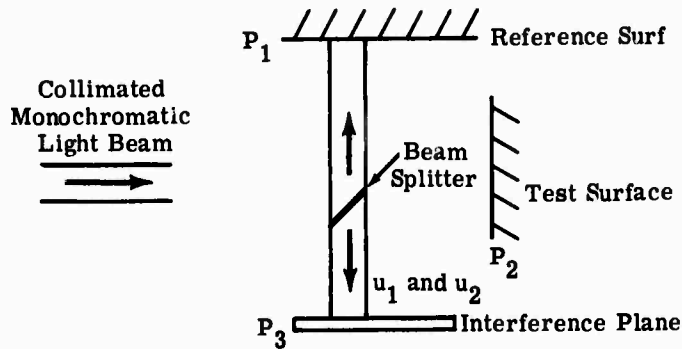
FIGURE 70. APPARATUS FOR INTERFEROMETRIC SURFACE-
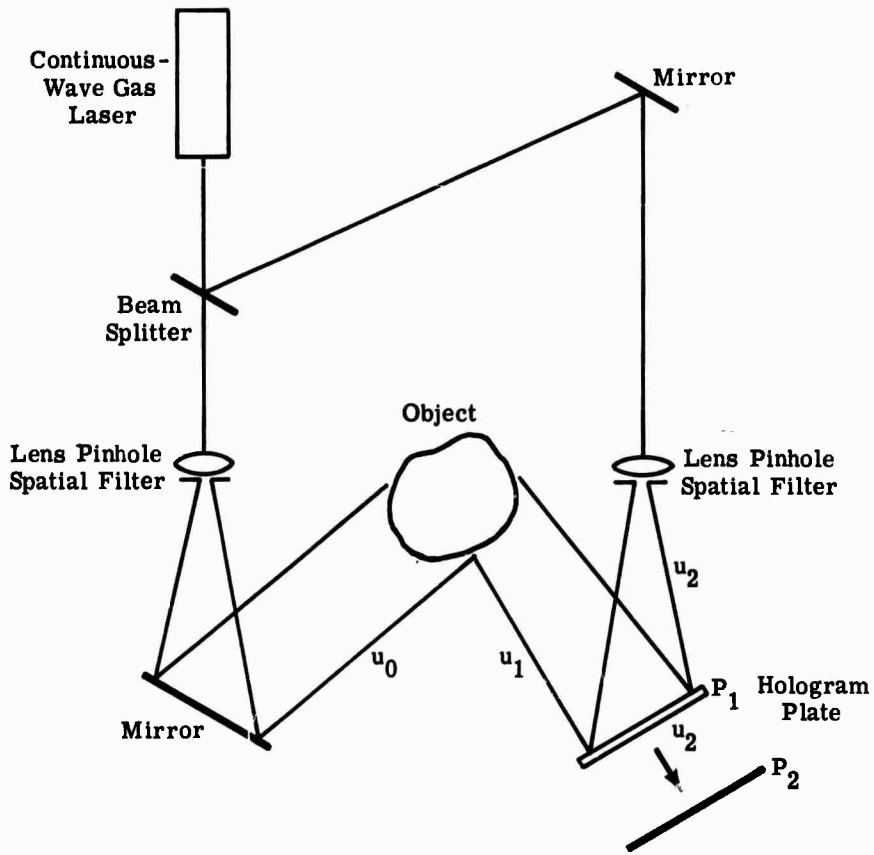ROUGHNESS MEASUREMENT

FIGURE 71. CONFIGURATION FOR HOLOGRAPHIC SURFACE-ROUGHNESS
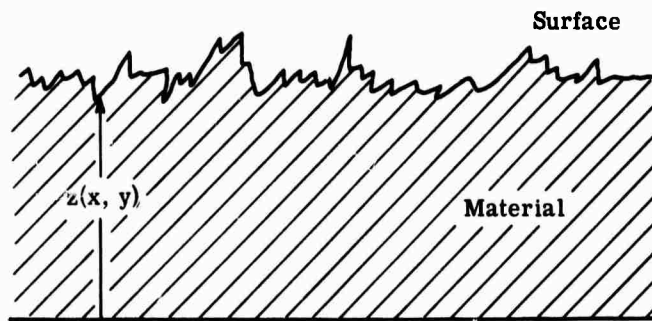MEASUREMENT

Surface

FIGURE 72. SURFACE CONTOUR GREATLY MAGNIFIED

roughness function $z(x, y)$ is defined as the distance from a datum surface to the material surface at any point (x, y). It is convenient to define a mean surface $\bar{z}(x, y)$

$$\iint_{surf} [z(x, y) - \bar{z}(x, y)]\, dx\, dx = 0 \qquad (62)$$

With this definition, it is possible to define an rms roughness σ

$$\sigma^2 = \iint (z - \bar{z})^2\, dx\, dy \qquad (63)$$

where the integrals in both Eqs. (62) and (63) are taken over the entire surface of the material.

An experimental investigation of this holographic interferometry method of measuring surface roughness was conducted. We prepared the specimens for the experiment by cutting thin disks from a steel cylinder 2 in. in diameter. Preparing the specimen in this way assured that the material was identical for all specimens, thereby assuring a constant material reflectivity for all experiments. In addition, the influence of effects such as depolarization of the reflected beam was isolated and identified.

The surfaces of the specimens were prepared in three separate ways: grinding, lapping, and super-finish lapping. The relationship between contrast ratio (i.e., R) and surface roughness (i.e., σ) was investigated separately for the three classes of surface finish. This procedure allowed the greatest possibility of determining all of the parameters of this method of measuring surface roughness. The test specimens were prepared having surface roughness and in the following sequence:

Preparation Roughness (μin.)		
Ground	Lapped	Super Finish
4	2	4
8	4	8
16	8	
32	16	

100

The surface roughness of these test specimens was measured with a Bendix profilometer, which is a contacting stylus instrument calibrated in accordance with ISA standards. The above values for σ constitute accepted standards for measuring surface roughness of hard, flat surfaces.

The experimental configuration for this measurement is illustrated schematically in Fig. 73. The configuration shown in Fig. 73 is similar to that shown in Fig. 71 except that the object beam u_0 is collimated by means of lens L_1. This collimated object beam offers several advantages over the uncollimated object beam of Fig. 71. First, it makes sufficient use of available light because the reflected beam u_1 is principally specular reflection from the nominally flat test surface. In addition, it enables a simple mathematical formulation of the wavefronts u_1 and u_2 in the theoretical interpretation of the experimental data. In the experimental configuration of Fig. 73, plane P_1 contains the hologram plate, and plane P_2 is the plane in which the interference pattern is observed.

There are certain characteristics of this interference pattern which influence the accuracy of this method of measuring surface roughness. A close examination of a typical interference pattern (i.e., Fig. 74) reveals that a fine-structure random pattern is superposed on the coarse fringe pattern. The coarse pattern is a consequence of the interference of the wavefronts as determined by reflection from the average surface (i.e., $\bar{z}$ of Eq. 62). This is the pattern which would be observed if the surface were perfectly smooth and the laser perfectly coherent. This fine structure, which is a consequence of the surface roughness and, to a lesser extent, of the imperfect laser coherence, lowers the contrast ratio of the interference fringe pattern from that which would be obtained if the two wavefronts u_1 and u_2 were perfectly coherent.

For an accurate determination of the fringe contrast ratio, the coarse fringe pattern must contain the minimum possible number of fringes across the pattern, allowing at least one maximum and one minimum intensity. This is required so that the operation by which the light intensity in plane P_2 is measured adequately samples the fine-structure intensity variations. The aperture used must be sufficiently large to sample this random function adequately. On the other hand, this aperture must be sufficiently small, as compared to the coarse fringe pattern, that the average light intensity is approximately constant over the aperture. Thus, the viewing aperture in plane P_2 is a compromise between the low spatial frequency content of the coarse fringe pattern and the relatively high spatial frequency content of the random fine-structure pattern.

The optimum instrumentation for measuring fringe contrast ratio includes a scanning photocell in plane P_2. The photocell output voltage v_0 is proportional to the integrated light intensity, $I(x_2 y_2)$, over its entire aperture:

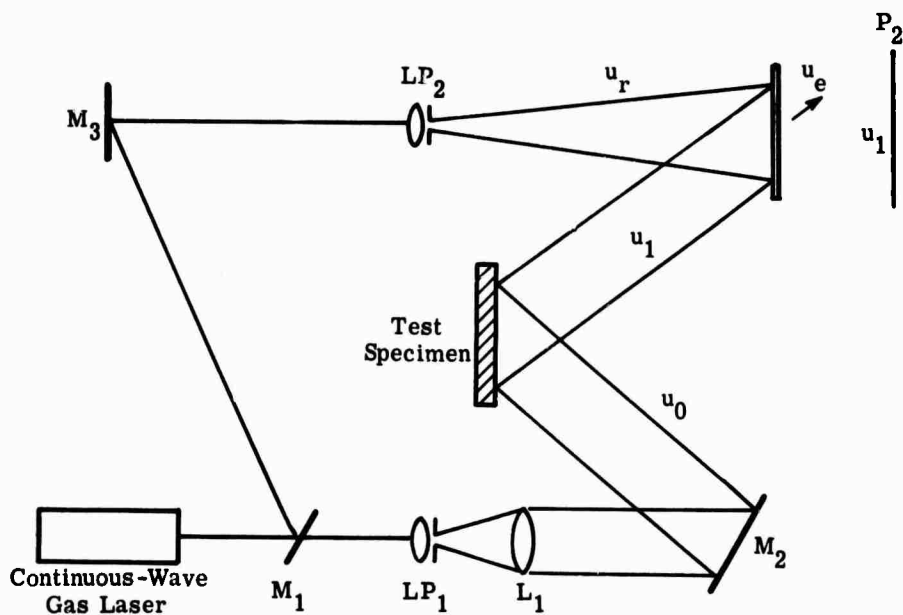$$v_0 = k \iint_{\text{aperture}} I(x_2 y_2)\, dx_2\, dy_2 \tag{64}$$

FIGURE 73. EXPERIMENTAL SETUP FOR HOLOGRAPHIC SURFACE-ROUGHNESS
MEASUREMENT

FIGURE 74. TYPICAL INTERFERENCE PATTERN

where k is a photocell parameter, $x_2 y_2$ are the coordinates of plane P_2, and the integral is taken over the photocell aperture. If we assume that the ensemble average statistics of intensity $I(x_2 y_2)$ are identical to the spatial average (i.e., ergodic statistics), this voltage v_0 is proportional to the expected value $E[I(x_2 y_2)]$; this is significant for the explanation of the theory of this method which is given below.

Unfortunately, a scanning photocell was not available for measuring the light intensity distribution in plane P_2 of the instrumentation shown in Fig. 73. Instead, we measured the

102

intensity distribution by first recording it photographically, then measuring the film density variations on a recording microdensitometer, which produces a chart record on graph paper of the film local density. The light intensity maxima and minima are determined by converting density to intensity with the use of the film sensitometric curves.

The film introduces an error in the measurement of the desired light intensity distribution because the film density is a logarithmic function of intensity

$$D_1 - D_2 = \gamma \log \frac{E_1}{E_2} = \gamma \log \frac{I_1}{I_2} \qquad (65)$$

where I_1 and I_2 are the intensities at any two points in the intensity distribution, D_1 and D_2 are the corresponding film densities, and γ is a film parameter depending upon the film processing. It is convenient to write the intensity distribution in plane P_2 as

$$I(x_2 y_2) = \overline{I} + f(x_2 y_2) \qquad (66)$$

where $\overline{I}$ is the intensity of the coarse fringe pattern which would be obtained if the surface were perfectly smooth, and $f(x_2 y_2)$ is the fine-structure variation intensity which results from the surface irregularity. Using this notation, we can give the density variations of the film which records $I(x_2 y_2)$

$$D - \overline{D} = \gamma \log \frac{I}{\overline{I}} \qquad (67)$$

$$= \log \left[1 + \frac{f}{\overline{I}}(x_2 y_2) \right]^{\gamma} \qquad (68)$$

$$= \log \left[1 + g(x_2 y_2) \right]^{\gamma} \qquad (69)$$

where $g = \dfrac{f(x_2 y_2)}{\overline{I}}$. The intensity transmittance of this film is given by

$$\frac{T}{\overline{T}} = \log^{-1} D - \overline{D} = \left[1 + g(x_2 y_2) \right]^{\gamma} \qquad (70)$$

The microdensitometer measures the integrated average value $\hat{y}_t$ of T over an aperture A which is selected for the operation of the instrument

$$y_t = k \iint_A T(xy) \, dx \, dy \qquad (71)$$

103

$$= k\bar{f} \iint_A [1 + g(x_2 y_2)]^{-\gamma} dx_2 dy_2 \tag{72}$$

Recall from Eq. (64) that the desired quantity for determining the contrast ratio R is proportional to the following integral

$$\iint_A [1 + g(x_2 y_2)] dx_2 dy_2 = A + \iint_A g(x_2 y_2) dx_2 dy_2 \tag{73}$$

The microdensitometer output is proportional to the desired integral (73) only if $\gamma = 1$. However, in the experimental study, $\gamma = 0.56$, and the use of film as an intermediate step in measuring R introduces errors in this constant ratio.

On the other hand, the rms surface roughness for all test specimens is small as compared to the laser wavelength. As a consequence of this,

$$g(x_2 y_2) << 1 \tag{74}$$

In this case, the integrand of Eq. (72) can be expressed approximately by

$$(1 + g)^{-\gamma} \simeq 1 - \gamma g \tag{75}$$

Substituting this approximation into Eq. (72) yields the following approximation for the micro-densitometer output

$$y_t = k\bar{T} \iint_A [1 - \gamma g(x_2 y_2)] dx_2 dy_2 \tag{76}$$

$$= k\bar{T}[A - \gamma \iint_A g(x_2 y_2) dx_2 dy_2] \tag{77}$$

$$\simeq k\bar{T}[A + \iint_A g(x_2 y_2) dx_2 dy_2]^{-\gamma} \tag{78}$$

Here the approximation (75) has been used to write Eq. (78).

The microdensitometer display is calibrated in equivalent average density D_a

$$D_a - \bar{D} = -\log \frac{y_t}{k\bar{T}} = \gamma \log [A + \iint_A g(x_2 y_2) dx_2 dy_2] \tag{79}$$

Thus, provided that $g(x_2 y_2) << 1$, the microdensitometer output is proportional to the desired integrated intensity in plane P_2.

104

The experimental investigation of the surface roughness of the test specimens with the use of the configuration shown in Fig. 73 proceeded as follows:

(1) With a test specimen in place, a hologram was exposed, developed, and returned to plane P_1.

(2) The interference fringe pattern occurring in plane P_2 was observed and photographed with Kodak super Panchro-press film.

(3) After the film was developed, the average density, D_a, for this film was measured on a Joyce-Loebl recording densitometer.

(4) We converted the average film density, D_a, to the intensity in plane P_2 using the relationship

$$D - \bar{D} = \log \frac{T}{\bar{T}}$$

(5) The maximum and minimum intensities in plane P_2 were determined, and the contrast ratio, R, was computed, where $R = I_{max}/I_{min}$.

Figures 75 and 76 are graphs of the function $R(\sigma)$ for ground and super-finish surface preparations, respectively. In these graphs, σ represents the rms roughness of the test specimens as measured on the (profilometer) stylus instrument.

The exact theory of this method of measuring surface roughness is extremely complicated and requires a vector formulation of physical optics. However, as shown in Fig. 77, the first-order scalar approximation to this theory correlates well with experimental results and offers valuable insight into the method, although it should be emphasized that this theory is, at best, an approximation which ignores the effect of depolarization of the incident light at the surface of the material and which assumes a specific statistical distribution of the surface-roughness function. In addition, this theory assumes perfect, laser spatial and temporal coherence and attributes the imperfect correlation of the wavefronts u_1 and u_2 entirely to the surface roughness. Furthermore, this theory assumes that the spatial frequency content of the roughness function is sufficiently high that an adequate statistical sampling of the intensity distribution in plane P_2 can be obtained. However, the justification of this approximate theory is its close agreement with experimental results.

For the purposes of describing this theory, the light amplitude distribution in plane P_2 of Fig. 73 is denoted $U(x_2 y_2)$. According to Ref. [81], U_2 is related to the light amplitude distribution on the object surface $U(x_1 y_1)$ by the expression

$$U(x_2 y_2) = \frac{\exp i\Phi}{\lambda R} \iint\limits_{A_o} U(x_1 y_1) \exp \left\{ i[kz(x_1 y_1) + \frac{2\pi}{\lambda R} (x_1 x_2 + y_1 y_2) dx_1 dy_1] \right. \tag{80}$$
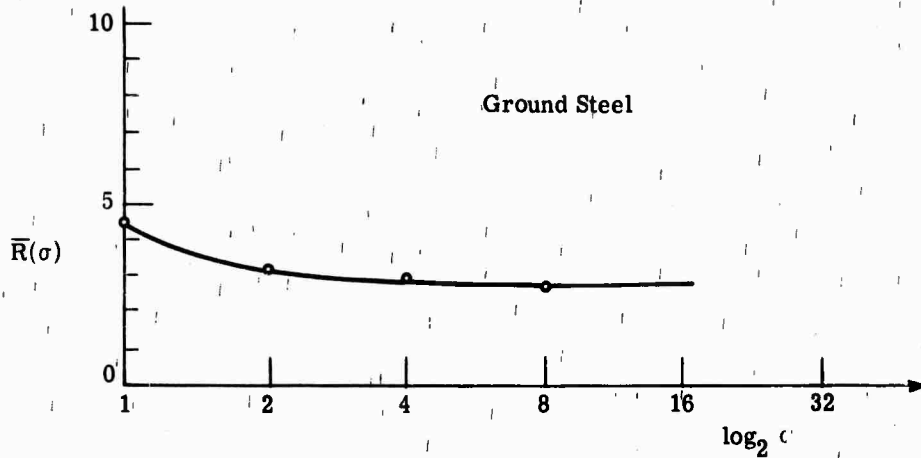
FIGURE 75. CONTRAST RATIO VERSUS SURFACE ROUGHNESS FOR GROUND SURFACE
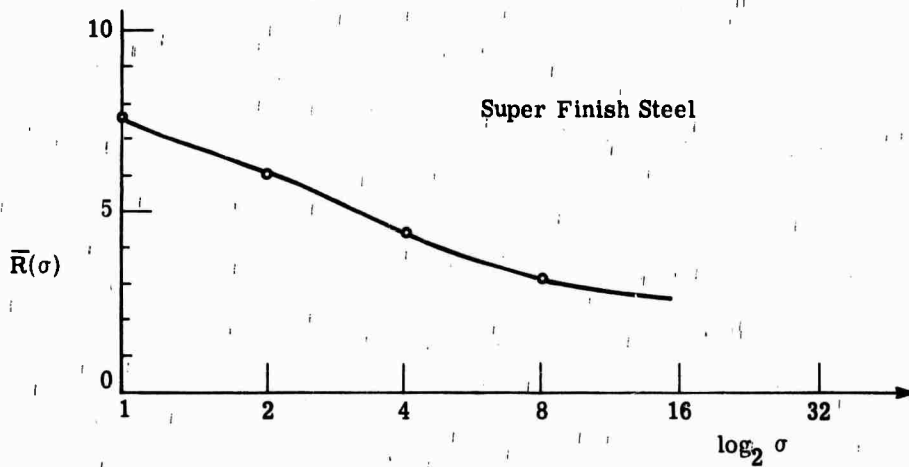
FIGURE 76. CONTRAST RATIO VERSUS SURFACE ROUGHNESS FOR SUPER FINISH
SURFACE
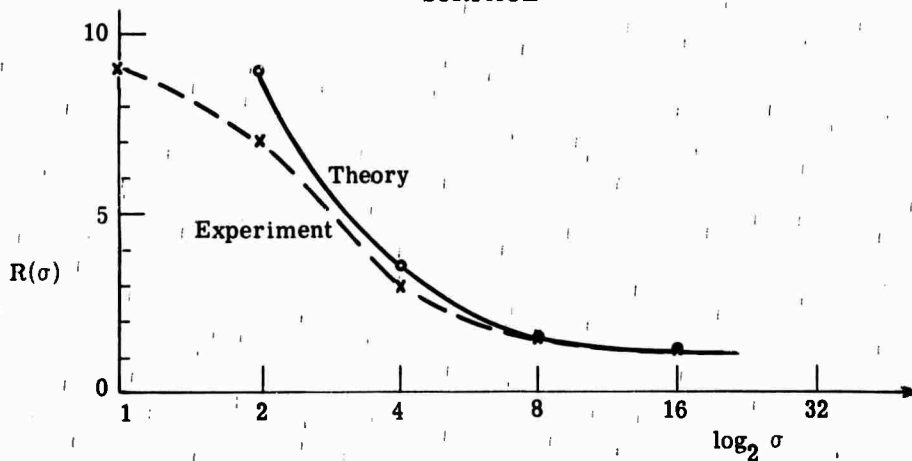
FIGURE 77. COMPARISON OF SCALAR THEORY AND EXPERIMENTAL RESULTS
OF INTERFEROMETRIC SURFACE-ROUGHNESS INSTRUMENT

106

where the following notation is approximate:

R = the distance from the center of the object ot the center of plane P_2 (i.e., origin of $x_1 y_1$ to origin of $x_2 y_2$)

Φ = the optical phase shift corresponding to distance R

A_0 = the illuminated area of the object's surface

λ = the optical wavelength

z = $f(x_1 y_1) - \bar{f}$ = the deviation of the surface-roughness function from the mean surface

With the object in place and the reference beam blocked, the light amplitude distribution in plane P_2 is denoted, $U_1(x_2 y_2)$. With the object beam blocked and the hologram illuminated by the reference beam, the light amplitude distribution in plane P_2 is denoted $U_2(x_2 y_2)$. These two functions are related to $U(x_1 y_1)$ by the expressions

$$U_1(x_2 y_2) = K \iint_{A_0} F(x_1 y_1 x_2 y_2) \exp [ikz(x_1 y_1)] dx_1 dy^1 \tag{81}$$

$$U_2(x_2 y_2) = K\rho \iint_{A_0} F(x_1' y_1' x_2 y_2) \exp [kz(x_1' y_1')] dx_1^1 dy_1^1 \tag{82}$$

where F = $U(x_1 y_1) \exp j\frac{2\pi}{\lambda R}(x_1 x_2 + y_1 y_2)$

$K = \frac{\exp \phi}{\lambda R}$

ρ = ratio of the amplitude of u_1 and u_2 as determined by reference beam and hologram diffraction efficiency

$x_1' y_1'$ = the coordinates of the virtual image of the object as seen through the hologram

The interference pattern in plane P_2 is represented by the superimposition of U_1 and U_2

$$U_1 + U_2 \tag{83}$$

The fringe contrast ratio R is the ratio of the maximum expected value to the minimum expected value of the intensity

$$I = \left| U_1 + U_2 \right|^2 \tag{84}$$

where the symbol I denotes intensity. If we assume that the statistics of the random intensity pattern in plane P_2 are ergodic, the ensemble average or expected value, E(I), is the same as

the spatial average over same aperture, A:

$$E(I) = \int_{-\infty}^{\infty} P(I) I \, dI = \lim_{A \to \infty} \frac{1}{A} \iint_A I(x_2 y_2) \, dx_2 \, dy_2 \tag{85}$$

If we assume also that the aperture A of the scanning microdensitometer is sufficiently large, the following approximation is valid

$$E(I) \cong \frac{1}{A} \iint_A I(x_2 y_2) \, dx_2 \, dy_2 \tag{86}$$

This approximation is the basis of the comparison between theory and experiment. The ensemble average or expected value, $E(I)$, can be computed theoretically, and the spatial average (i.e., $\frac{1}{A} \iint_A I \, dx_2 \, dy_2$) can be measured experimentally. Correlation of theory and experiment depends upon the validity of this approximation.

In this case, the appropriate quantity to determine measured fringe contrast ratio is $E(I)$, where

$$E(I) = \int_{-\infty}^{\infty} p(I) |U_1 + U_2|^2 \, dI \tag{87}$$

However, the probability-density function, $p(I)$, is determined by the probability-density function, $p(z)$, which represent the statistics of the roughness function $z(xy)$. It is shown in subsequent calculations that a Gaussian, probability-density function gives good agreement between this simple scalar theory and experimental results. The expected value in Eq. (87) can be found by the following calculation

$$E(I) = \int_{-\infty}^{\infty} p(z) I(z) \, dz \tag{88}$$

The intensity I in plane P_2 can be written in the form

$$I = K \left| \iint_A F(x_1 y_1)[\rho \exp i\phi(x_2 y_2) + \exp (ikz) \, 1] dx_1 \, dy_1 \right|^2 \tag{89}$$

where ϕ is the local phase difference between wavefronts U_1 and U_2, and $z_1 = z(x_1 y_1) - z(x_1' y_1')$. In this latter function, the coordinates $x_1' y_1'$ are related to $x_1 y_1$ by the simple transformation

$$x'_1 = x_1 + \Delta x \tag{90}$$

$$y'_1 = y_1 + \Delta y \tag{91}$$

where Δx and Δy are the translation between the coordinate system caused by registration change in relocating the hologram plate after it is developed. It is this misalignment between the actual object position and the apparent position of the hologram virtual image which causes the interference fringes.

In Appendix II, it is shown that the expected value, E(I), for this fringe pattern is given by

$$E(I) = K\left(\rho^2 + 2\rho \cos \exp \frac{-k^2\sigma^2}{2} + \exp -k^2\sigma^2\right) \left| \iint_A F \, dx_2 \, dy_2 \right|^2 \tag{92}$$

It is worthwhile to interpret Eq. (92) to understand the interference pattern in plane P_2. The integral factor of Eq. (92) represents the light intensity distributi n in plane P_2, caused by either U_1 or U_2, of the light refracted from the object. The first factor represents the interference pattern produced by the superimposition of U_1 and U_2. The maxima of this pattern occur for $\phi = 2n\pi$ (n integer), and the minima occur for $d = (2n + 1)\pi$ (n integer).

As a consequence of the collimated object beam, the second factor of Eq. (92) is nearly constant over the central portion of the interference pattern. This has been established experimentally by measurements of the density of film exposed to U_1 alone and U_2 alone. Therefore, the contrast ratio, R, is given by the expression

$$\frac{E(I)\big|_{\phi=0}}{E(I)\big|_{\phi=\pi}} \tag{93}$$

$$R = \left(\frac{\rho + \exp \frac{-k^2\sigma^2}{2}}{\rho - \exp \frac{-k^2\sigma^2}{2}} \right)^2 \tag{94}$$

Figure 77 is a plot of Eq. (94) and of the experimental results obtained for lapped steel surfaces. Note that the contrast ratio, plotted versus $\log_2 \sigma$, covers a range from 2μin. $\leq \sigma \leq 32\ \mu$in. There is high correlation between theory and experiment over this entire range.

A similar co.nparison between theory and experiment was not attempted for super finish or ground surfaces because of the limited range of available surface roughness for the super finish. Also, we did not compare theory and experiment for ground surface, since the assumptions we would have to make for the simple scalar theory are not valid for these surfaces.

9.2. SUMMARY

We devised a method to measure the rms surface roughness of metals by examining the way the surface scatters light. By using holographic interferometry, we may be able to make surface-roughness measurements on curved surfaces. The results of this optical measurement were compared with profilometer measurements.

10
NONDESTRUCTIVE TESTING OF ARTILLERY COMPONENTS

10.1 INTRODUCTION

The major objective of this portion of the research program was to apply holography to special military problems. To fulfill this objective, we studied the use of holographic interferometry to locate defects in artillery components (specifically, projectiles and shell casings) without destroying them.

10.2 GENERAL EXPERIMENTAL PROCEDURE

The configuration for this experimental investigation is illustrated schematically in Fig. 78, a configuration similar to that shown in Fig. 73. This investigation used real-time holographic interferometry, as described in Sections 2, 4, and 5 of this report, to locate and/or identify defects in shells and casings. The defects appear as nonuniformities in the interference fringe pattern on the image of the specimen when it is subjected to some mechanical load. Our general experimental procedure was as follows:

(1) A hologram was made of the object, which initially had no defects, and the changes in the interference pattern obtained from this object when it was placed under mechanical stress were observed and recorded photographically.

(2) An artificial defect was machined into the object.

(3) A second hologram was made, and the changes in the interference pattern obtained from the defected object subjected to the same amount of mechanical stress were observed and photographed.

(4) A comparison of the changes in fringe patterns from (1) and (3) was made.

(5) The location and sometimes the nature of the defect were identified by nonuniformities evident from the comparison of fringe patterns (4).

10.3. SHELL CASINGS

Our experiments were performed on a 75-mm artillery shell casing and a 75-mm projectile.
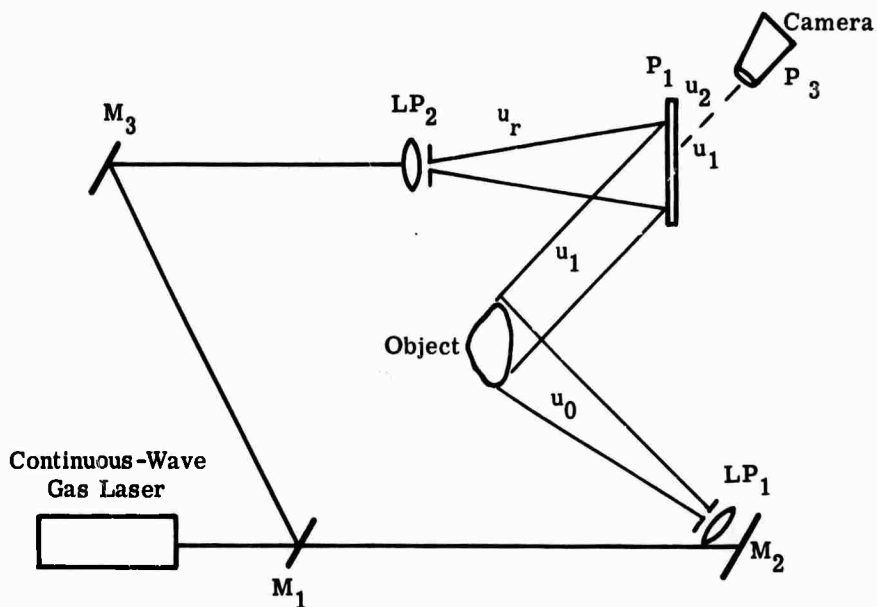
FIGURE 78. SETUP FOR HOLOGRAPHIC INTERFEROMETRIC DETECTION OF FLAWS

10.3.1. EXPERIMENTS

The initial experiments were performed on an empty brass shell casing cut 4 in. from the end plate which supports the firing cap. Figure 79 is a cross-section drawing of this modified shell casing, showing the location and type of defects.

This shell casing was placed in a holder (as shown in Fig. 80), which sealed both ends of the shell. A pressure fitting was attached to the holder so that the shell casing could be pressurized internally by a compressed air source, and a gauge was attached to the pressure line so that the magnitude of the pressure inside the cylinder could be measured. Figure 80 shows a wet gate which is used for holding the hologram plate. Both the wet gate and a conventional plate holder were used in the experiments reported in this section.

Figure 81 is a schematic sketch of Fig. 80. Note that a lens and diffusing screen are used in this configuration to provide uniform illumination of the shell. In addition, the shell casing was sprayed with flat white paint to make it a more diffusely reflecting object; this improves visibility of those portions of the shell casing not along the cylindrical axis.

In order to have some basis for comparison of the interference fringes before and after the defects were cut into the shell casing, a hologram was made of the defect-free shell. The shell was placed in the holder as shown in Fig. 80, and a hologram was recorded. The hologram plate was developed and returned to plane P_1 of the configuration shown in Fig. 78.
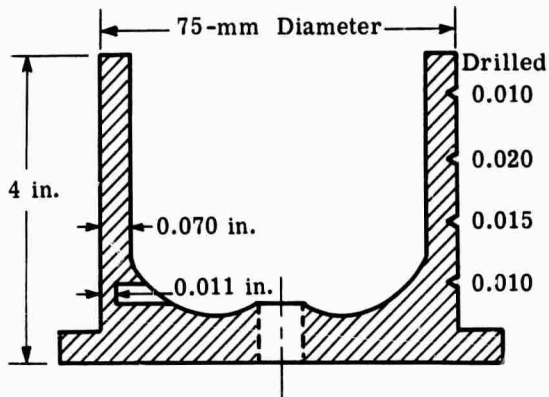
FIGURE 79. SKETCH OF BRASS ARTILLERY
SHELL CASING
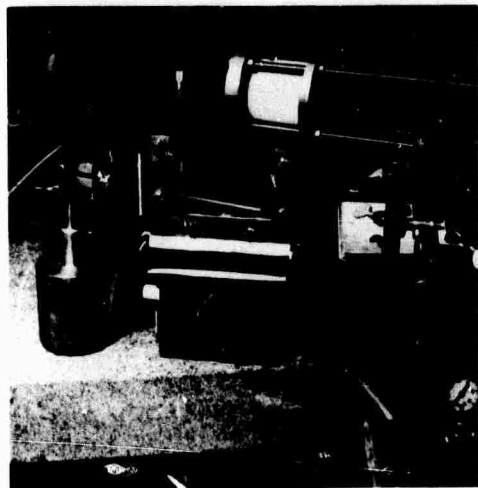
FIGURE 80. EXPERIMENTAL SETUP FOR
DETECTING DEFECTS IN ARTILLERY SHELL
CASING
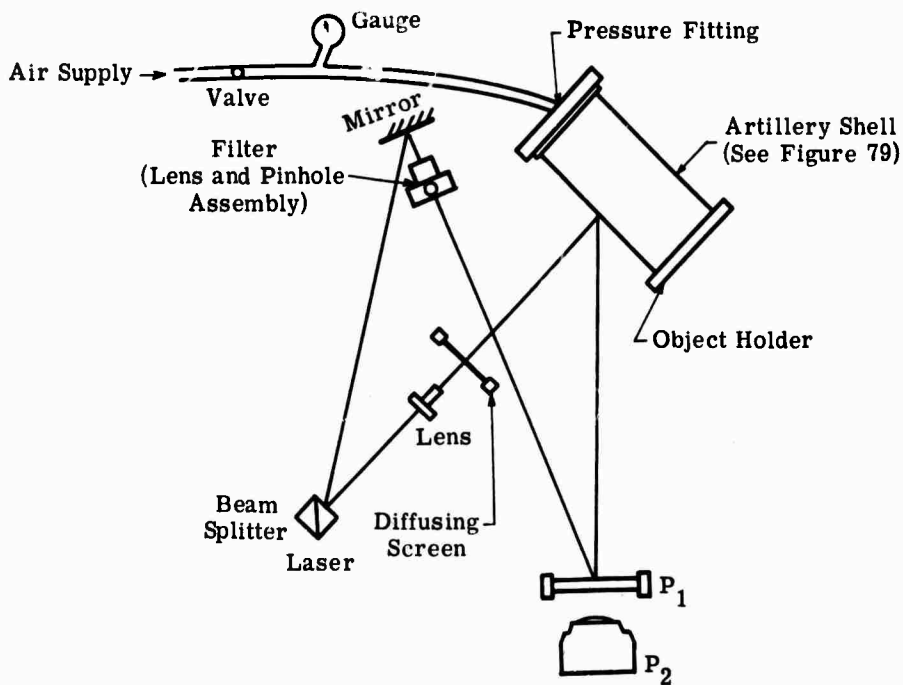
FIGURE 81. SCHEMATIC OF SETUP FOR STUDYING DEFECTS IN ARTILLERY SHELL
CASING

The object was illuminated by U_o and the developed hologram by the reference beam, producing an image in plane P_2 (i.e., camera focal plane) of the object superposed with an interference pattern. This interference pattern was observed and photographed for various internal pressures. Figure 82 is a sequence of photographs of the fringe pattern for several representative pressures. These fringe patterns indicate a uniform expansion of the shell casing, giving no evidence of any nonuniformity in expansion such as would occur around a defect.

After the defects shown in Fig. 79 were machined into the shell casing, it was returned to the holder and another hologram was made. To make this hologram, the shell casing was oriented so that the cut in the fillet on the inside of the casing was along the viewing axis of the shell casing. This afforded the maximum influence on the interference fringes in the vicinity of the cut. The hologram was recorded, developed, and returned to the plate holder. The interference fringe pattern was observed and photographed as described above for the same internal pressure readings as those used for the defect-free object. Figure 83 is a series of photographs of the resulting fringe patterns.

The only evidence of any nonuniformity in the fringe pattern is a slight flattening of the fringe shape in the vicinity of the cut. However, this is not a strong enough effect to identify and/or locate the defect clearly. The fringe density at the other end of the shell casing increases with increasing pressure, indicating normal cylindrical expansion. Evidently, the cut in the inside shell wall is too small in lateral extent to be resolved by this method.

A similar holographic study was made with the shell casing oriented so that the four, small, drilled holes were along the viewing axis. Again, it was found that these defects could not be resolved with this loading technique.

In previous studies using holographic interferometry to locate defects, it was noted that dents and large deformations could be observed in cylindrical surfaces [32, 33]. A second artillery shell casing was cut 4-in. long, as shown in Fig. 79. This shell casing was painted with a flat white paint to make its surface diffusely reflecting. Two artificial defects were made along an element of the cylindrical surface of this shell casing. One defect was a small dent made by striking the shell with a center punch. This defect had a conical shape with a diameter at the outside of approximately 1 mm. The second defect was a larger deformation caused by forcing a 1/4-in.-diameter sphere into the shell by means of a hydraulic press. After this second shell casing with the two artificial defects was placed in the object holder shown in Fig. 80 and oriented so that the defects were along the viewing axis, a hologram was recorded. The developed hologram plate was returned to the holder, and the fringe pattern was photographed for various internal pressures. Figure 84 is a series of photographs of the resulting interference fringe pattern.

Although there is no apparent fringe pattern deformation associated with the center punch dent, there is substantial fringe nonuniformity in the region surrounding the larger dent. The
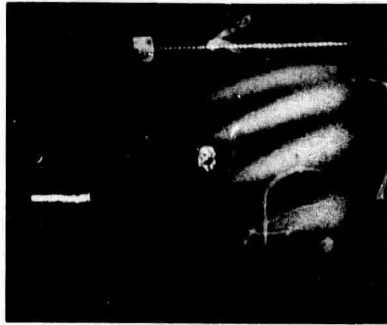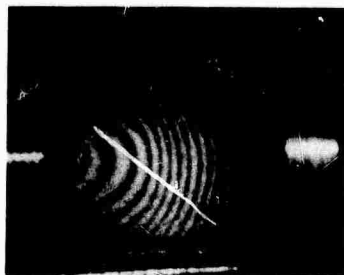
(a)
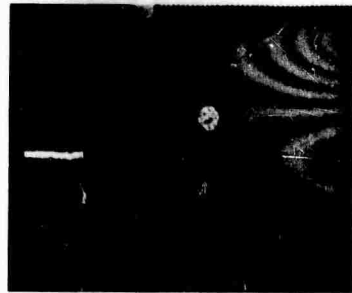
(b)
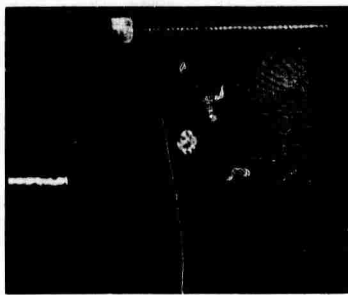
(c)
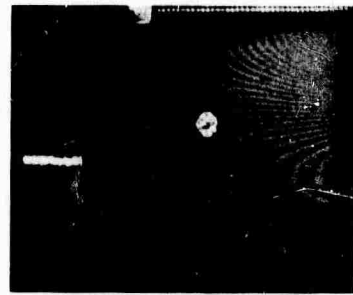
(d)

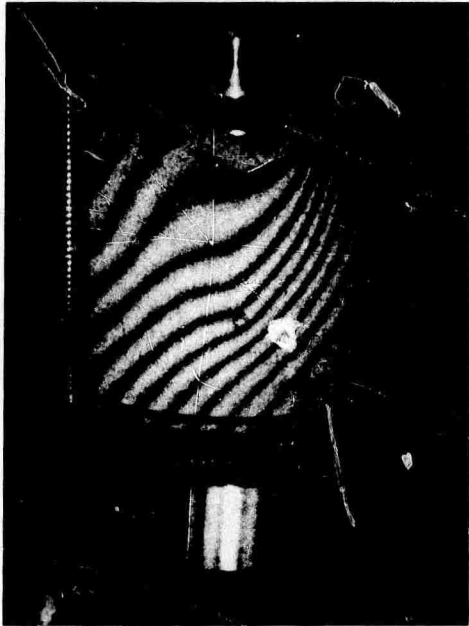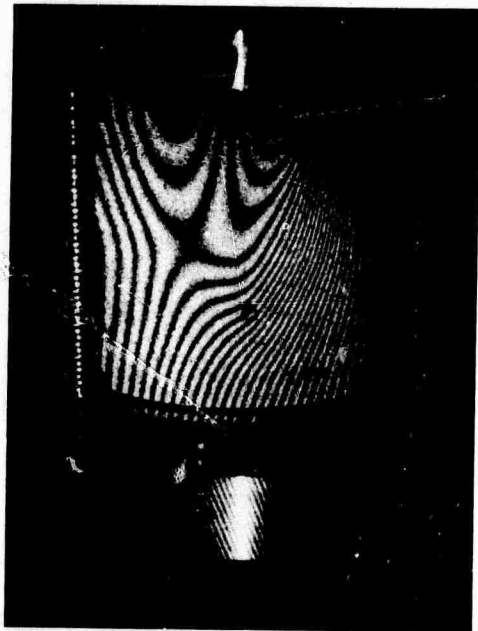FIGURE 82. INTERFERENCE FRINGES ON PRESSURIZED SHELL CASING
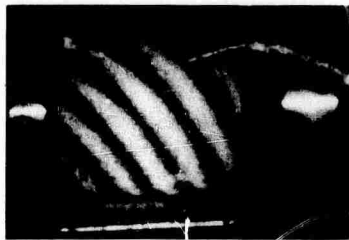
(a)
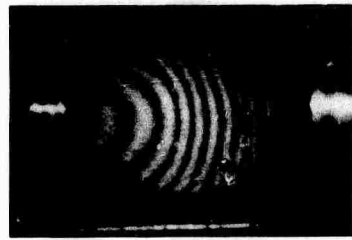
(b)

(c)

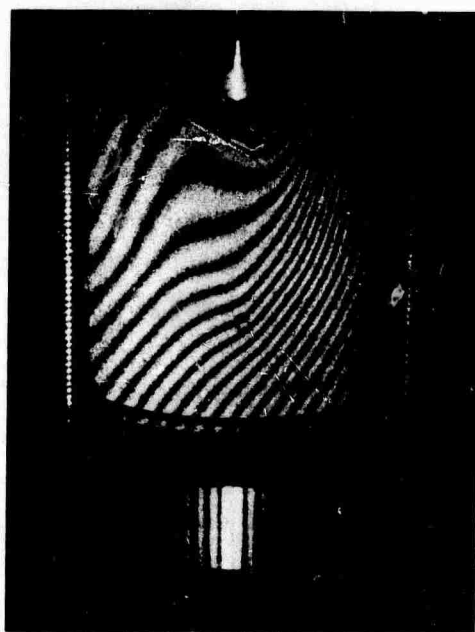FIGURE 83. INTERFERENCE FRINGE PATTERNS ON OBJECT, SHOWN IN FIGURE 83, WITH INTERNAL CUT

NOT REPRODUCIBLE

FIGURE 84. INTERFERENCE FRINGES ON SECOND SHELL CASING WITH DENT DEFECTS

nonuniformity of the fringe localizes slightly off the viewing axis, apparently because of the nonhomogeneity of this deformation. The characteristics of the deformation produced by forcing a steel sphere into the shell casing are nonuniform, since the control over the resulting shell deformation was imperfect.

10.3.2. CONCLUSIONS

Several conclusions can be drawn from the above experimental study. Perhaps the most important of these is that the method cannot distinguish small, geometrically uniform defects. In addition, those defects which are made apparent by this method of viewing are imprecisely located. Furthermore, it is impossible to determine the exact nature of the defect because of the poor resolution in the fringe anomaly associated with the defect. Improved loading fixtures would likely render this technique more feasible.

10.4. PROJECTILES

10.4.1. EXPERIMENTS

The configuration for this study is essentially the same as that for the shell casing study, shown in Fig. 78, the only major difference is the difference in object holders. The artillery projectile, a much stronger structure than the shell casing, has an average wall thickness of about 3/8 in. Clearly, a much larger force is required to deform the projectile than to deform the shell casing.

For the purposes of this investigation, the artillery projectile was placed between the jaws of a hydraulic press. The press is capable of exerting an axial compressive force of several thousand pounds on the projectile. Figure 85 is a photograph of a 75-mm artillery projectile in the hydraulic press.

The procedure for studying the defects in the artillery projectile is to make a hologram of a projectile while it is in the press. Then a series of photographs is obtained as the projectile is compressed axially by the press. This series of interference fringe patterns served as a reference for studying the influence of defects on the interference pattern.

The fringe patterns became more dense as the projectile was loaded; however, the form of these patterns was essentially unchanged. This change in the interference pattern apparently resulted from a translation of the projectile along the direction in which it was viewed through the plate, and not from expansion of the cylinder.

The projectile was removed from the press, and a pair of artificial defects was machined into its interior. Figure 86 is a sketch of these defects shown in profile along a cross section of the cylinder. Near the base of this projectile, a circumferential ring, with a depth of 0.125 in. and a width of 0.125 in., was cut into the projectile. In addition, a half-cylindrical-shaped, longi-

tudinal section of material was removed near the projectile top by means of a grinding wheel. Although these defects were clearly artificial, they were assumed to be sufficiently large to cause a nonuniform deformation of the projectile when it was compressed. It was expected that this nonuniform expansion would be detectable as a nonuniformity in the interference pattern obtained when the cylinder was subjected to axial pressure.

The projectile with artificial defects was returned to the experimental apparatus, and a hologram was recorded and developed. The interference pattern was observed and photographed as the projectile was compressed. Figure 87 is a series of photographs of these interference patterns.

Note that the interference fringes became more dense as the projectile was compressed and that the shape of these fringes was essentially uniform. Evidently, a linear translation of the projectile in the hydraulic press was large compared with its deformation under load. It was concluded that the hydraulic press was too unstable for this application of holographic interferometry.

To overcome this problem, the system shown in Fig. 88 was used. The hologram plate was mounted on the metal plate in the hydraulic press. In this setup, the hologram plate translated along with the projectile and maintained registration as the projectile was compressed.

A hologram was made of the artillery projectile with the setup shown in Fig. 88. After it was developed, this hologram plate was returned to its holder, and the resulting interference fringe pattern was observed and photographed. Figure 89 is a series of photographs of this fringe pattern taken for several values of pressure.

Note that as the pressure is increased from 0 psi to about 300 psi, the fringe pattern is perturbed in the region of the defect. This defect is a 1/8-in.-deep, circumferential groove, as shown in Fig. 86.

10.4.2. RESULTS

This method of locating defects with the setup illustrated in Fig. 88 is important because it demonstrates the necessity of maintaining registration of the object and the hologram plate. In the earlier experiment in which the projectile was not held firmly in place with respect to the hologram plate, the linear translation of the projectile was large compared with the deformation caused by loading the projectile axially. Also, locating the defect requires relatively large object deformation to produce a fringe pattern substantially altered from the no-load fringe pattern.

Although we also used thermal expansion for deforming the projectile (a piece of metal with approximately the same mass as the projectile was heated to a high temperature and placed on top of the projectile), we were unable to locate the defects with the fringe patterns produced by this technique.

117
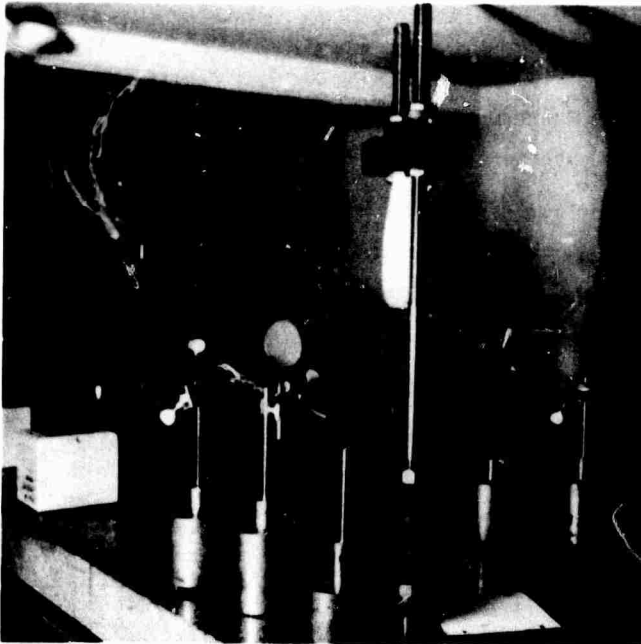
FIGURE 85. PROJECTILE AND HYDRAULIC
PRESS
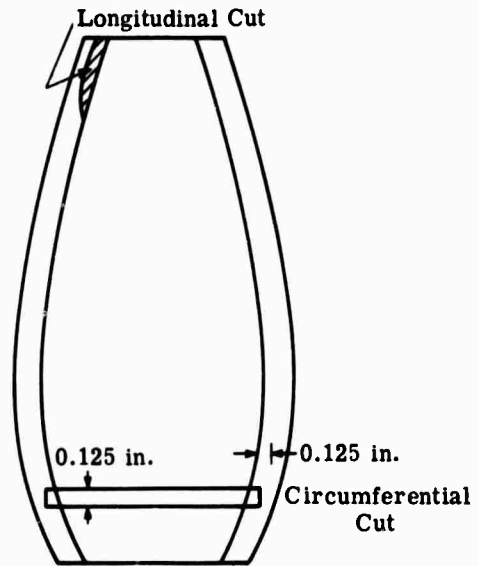
FIGURE 86. SCHEMATIC OF DEFECTS CUT
INTO ARTILLERY PROJECTILE

NOT REPRODUCIBLE

(a)   (b)   (c)

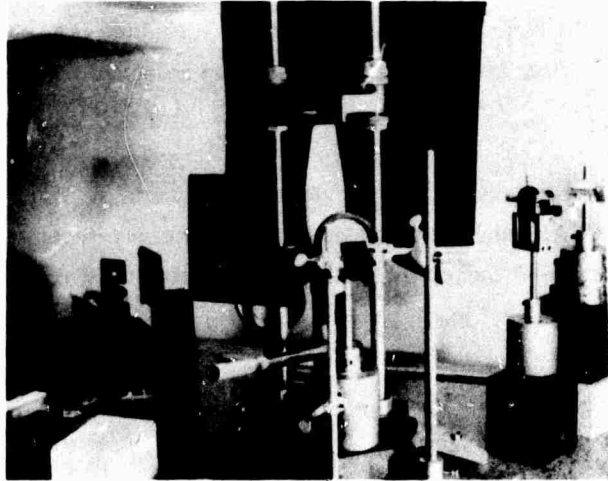FIGURE 87. INTERFERENCE FRINGE PATTERNS FOR COMPRESSED PROJECTILE
WITH ARTIFICIAL DEFECTS

FIGURE 88. EXPERIMENTAL SETUP FOR STUDYING
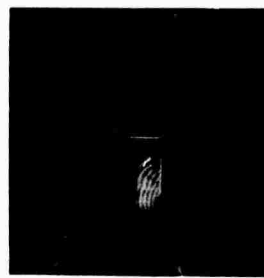AXIALLY LOADED ARTILLERY PROJECTILE

(a)

(b)

(c)

(d)

FIGURE 89. INTERFERENCE FRINGE PATTERNS OB-
TAINED FROM SETUP SHOWN IN FIGURE 88

119

Hence, on the basis of these experiments, the most promising technique for locating defects appears to be loading by the hydraulic press. But if this technique is used, one must be careful to maintain proper registration between the object and the hologram.

10.5. SUMMARY

The use of holographic interferometry for detecting flaws in artillery shell casings and projectiles was investigated. Although we found that holographic interferometry has some potential for nondestructive inspection of these components, its practicality was not clearly assessed. One reason was the lack of a sufficient loading mechanism.

Appendix I
FRINGE FORMATION AND LOCALIZATION WITH TRANSPARENT OBJECTS

Section 6 of this report referred to the phenomenon of fringe localization in holographic interferometry of transparent objects. In order to explain this phenomenon, this appendix describes the formation of interferometric fringes when a simple transparent object is diffusely illuminated.

Consider the configuration in which the test object is bound by parallel flat surfaces separated by a distance L as shown in Fig. 90. We are considering the two-dimensional case here for simplicity, but the extension to three dimensions is obvious. The field of the change in refractive index which occurs in the test object between holographic exposures is denoted by $\Delta\mu(y, z)$. For purposes of describing the fringe formation, the presence of the hologram is inconsequential. What is important is that the observer at location (y, z) simultaneously detects two wave fields emanating from the diffusing screen, and that these differ from each other only by the effect of $\Delta\mu(y, z)$. The formation of interference fringes is caused by the change between exposures of the optical path of the light rays along the viewing direction. This is given by

$$\Delta \ell = \int \Delta\mu \, ds \qquad (95)$$
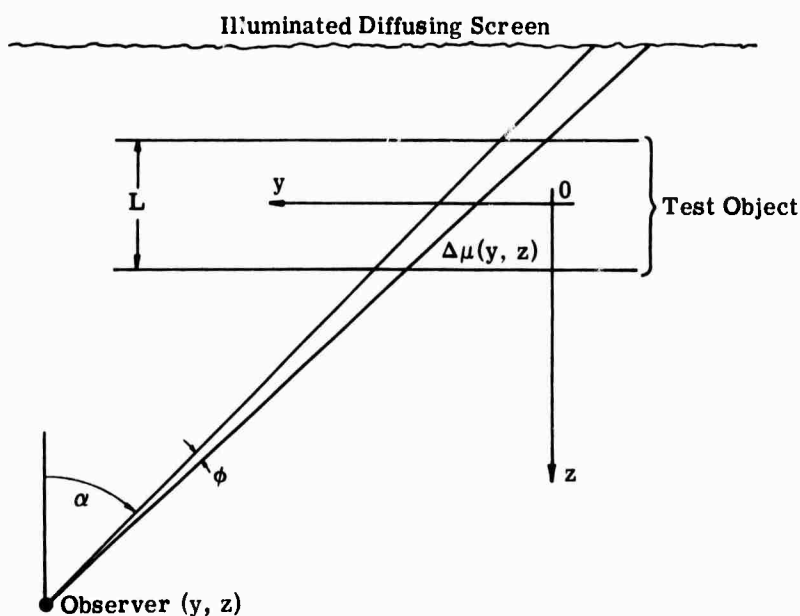
FIGURE 90. OBJECT CONFIGURATION AND COORDINATE SYSTEM

where s is the distance along the ray. In evaluating the integral (95), we shall neglect refraction effects; i.e., we will assume that the ray follows a straight path through the test section. Then

$$\Delta \ell = \int_{-L/2}^{+L/2} \Delta \mu(y, z) \sec \alpha \, dz \qquad (96)$$

where

$$y = Y - (Z - z) \tan \qquad (97)$$

along the light ray. As the holographic interferogram is viewed, a dark fringe will occur through a small aperture along a given direction (i.e., constant α) at every location for which

$$\Delta \ell = \frac{(2n + 1)\lambda}{2}$$

where n is an integer and λ is the wavelength of the light. The fringes viewed in a given direction are therefore equivalent to those which could be formed by a perfectly compensated Mach-Zehnder interferometer with the same orientation with respect to the test section.

Now consider the phenomenon of fringe localization. Any observing instrument, the eye for example, must gather light rays over a finite range of viewing angle. At an arbitrary observation location, the rays from the various angles will arrive with random phases, and no distinct fringes will be observed. Consequently, the fringes will appear to form only at those points for which

$$\left. \frac{\partial(\Delta \ell)}{\partial \phi} \right|_{\phi=0} = \frac{\partial(\Delta \ell)}{\partial \alpha} = 0 \qquad (98)$$

where ϕ is a small deviation from the viewing angle α. Using (96), we find

$$\frac{\partial \Delta \ell}{\partial \alpha} = \int_{-L/2}^{+L/2} \left[\Delta \mu(y, z) \frac{\sin \alpha}{\cos^3 \alpha} + \frac{\partial(\Delta \mu)}{\partial y} \frac{dy}{d\alpha} \sec \alpha \right] dz \qquad (99)$$

where $y = y(z, \alpha)$ is given by (97). When the fringe pattern is viewed normal to the test object ($\alpha = 0$), Eq. (99) reduces to

$$\left. \frac{\partial(\Delta \ell)}{\partial \alpha} \right|_{\alpha=0} = - \int_{-L/2}^{+L/2} \frac{\partial(\Delta \mu)}{\partial y}(Z - z) \, dz \qquad (100)$$

Hence, the surface in which the fringes localize, when it is viewed normal to the test section, will be that surface, $z = z(y)$, for which the integral in (100) vanishes. If $\Delta \mu$ does not vary in the z

122

direction, or if $\partial(\Delta\mu)/\partial y$ is an even function of z, the fringes will be localized in the center plane of the test section, $z = 0$.

It is instructive to consider a particular example in more detail. Suppose $\Delta\mu$ varies linearly in the y direction and is independent of z

$$\Delta\mu = \epsilon_0 + \epsilon y \tag{101}$$

Evaluation of (96) yields the change in optical path

$$\Delta\ell = [\epsilon_0 + \epsilon(Y - Z \tan\alpha)]L \sec\alpha \tag{102}$$

and (99) gives the condition for fringe localization

$$\frac{\partial(\Delta\ell)}{\partial\alpha} = \frac{L}{\cos^3\alpha}[(\epsilon_0 + \epsilon Y)\sin\alpha - \epsilon Z(1 + \sin^2\alpha)] = 0 \tag{103}$$

The fringes will therefore appear to be localized in a plane, the equation for which is

$$(\epsilon\sin\alpha)y - \epsilon(1 + \sin^2\alpha)z = -\epsilon_0\sin\alpha \tag{104}$$

It should be noted that the apparent surface of the fringe localization changes with the viewing angle α.

A similar analysis of an axially symmetric, refractive-index distribution indicates that the interference fringes will localize in the center plane of the cylinder normal to the viewing direction for all values of α.

Appendix II
DEVELOPMENT OF EXPRESSION FOR EXPECTED VALUE (EQUATION 92)

Given the function

$$I = \left|\iint_A F(\rho\exp i\phi + \exp ikz)\,dx_2\,dy_2\right|^2 \tag{105}$$

we must compute the expected value, $E(I)$

$$E(I) = \int_{-\infty}^{\infty} I(z)p(z)\,dz \tag{106}$$

where

$$p(z) = \frac{\exp\dfrac{-z^2}{2\sigma^2}}{\sigma\sqrt{2\pi}} \tag{107}$$

123

For the purpose of making this calculation, Eq. (105) must be rewritten in the form

$$\frac{I}{K} = \int_A dx_1 dy_1 \int_A dx_1' dy_1' F(x_1 y_1) F(x_1' y_1')[(\rho \cos \phi + \cos kz)(\rho \cos \phi + \cos kz)$$

$$+ (\rho \cos \phi + \sin kz)(\rho \cos \phi + \sin kz)] \tag{108}$$

where $z' = z(x_1' y_1')$. Using the trigonometric identities and simplifying algebraically, we can rewrite Eq. (108) in the form

$$\frac{I}{K} = \int_A dx_1 dy_1 \int_A dx_1' dy_1' FF'[\rho^2 + \rho \cos \phi (\cos kz + \cos kz') + \sin \phi (\sin kz + \sin kz')$$

$$+ \sin (\sin kz + \sin kz') + \cos k(z - z')] \tag{109}$$

We can find the expected value, E(I), by computing the expected value of each of the three terms in the record factor of the integrand of Eq. (109). For this purpose, the following identities are used:

$$\cos kz = \frac{1}{2} (\exp jkz + \exp -jkz)$$

$$\sin kz = \frac{1}{2j} (\exp jkz - \exp -jkz)$$

$$E (\exp jkz) = \exp \frac{-k^2 \sigma^2}{2} \tag{110}$$

$$E \cos k(z - z') = \exp \left\{ -k^2 [R_{zz'}(0) + R_{zz'}(x_1 - x_1', y_1 - y_1')] \right\}$$

where $R_{zz'}(x_1 y_1)$ is the cross correlation between $z(x_1 y_1)$ and $z' = z(x_1' y_1')$. For the assumed Gaussian statistics, $R_{zz'}(0) = \sigma^2$, and $R_{zz'} \approx 0$ for $x_1 - x_1' > 3\sigma$ and $y_1 - y_1' > 3\sigma$. The contribution of $R_{zz'}(x_1 - x_1', y_1 - y_1')$ to the integral in Eqs. (105-108) is negligible except for $x_1 - x_1' < 3\sigma$. Thus, if $A >> \sigma^2$, $R_{zz'}$ can be neglected in the integral. Substituting these identities into Eq. (105) yields

$$\frac{I}{K} E(I) = \int_A dx_1 dy_1 \int dx' dy_1' [\rho^2 + \rho \cos \phi E (\cos kz + \cos kz')$$

$$+ \sin \phi E (\sin kz + \sin kz') + E \cos k(z - z')] FF' \tag{111}$$

$$\cong \int dx_1 dy_1 \int dx_1' dy_1' FF' \left[\rho^2 + 2\rho \cos \phi \exp \frac{-k^2 \sigma^2}{2} + \exp -k^2 \sigma^2 \right] \tag{112}$$

124

provided that $A \gg \sigma^2$. Then, the formula for E(I) is given by

$$E(I) = K\left(\rho^2 + 2\rho \cos \phi \, \exp \frac{-k^2\sigma^2}{2} + \exp -k^2\sigma^2\right)\left(\iint_A F \, dx_1 \, dy_1\right)^2$$

Appendix III
TABLES OF CONTENTS OF PREVIOUS TECHNICAL REPORTS

Semiannual Report, 2420-5-P
(AD 857 061)

CONTENTS

Semiannual Report, 2420-9-P
(AD 705 220)

CONTENTS

Semiannual Report, 2420-12-P
(AD 875 043)

CONTENTS

CONTENTS

Appendix IV
GLOSSARY

aberrations — phase errors on a light wave which forms the image of a point

beam splitter — an optical element which reflects one portion of incident light and transmits the remainder

bleached hologram — a hologram, the complex transmittance of which has been converted to a pure phase function

coherence length — a measure of the temporal coherence of a light source (in essence, the maximum difference in optical path at which time-invariant interference can occur)

collimated — description of a beam of light, all rays of which are parallel to one another

complex amplitude — a quantity consisting of magnitude and phase, usually used to describe one polarization component of an optical electrical field

complex transmittance — a quantity which, when it is multiplied by the complex amplitude of an incident light beam, yields the complex amplitude of the transmitted beam

contour fringes — the contour lines of a contour map obtained by interference techniques

contour map — an image of an object with an overlaid set of lines connecting points of equal height

contrast — a ratio similar to signal-to-noise, usually the ratio of the difference between maximum and minimum image intensities to their sum

diffraction efficiency — the percentage of incident light energy diffracted by a hologram to form a reconstructed wave

diffuse — description of an opaque object surface which scatters light randomly in many directions from a single incident ray

distortion — similar to aberration, except that the phase error changes the location rather than the shape of the image spot

exposure — the amount of light energy per unit of the area which strikes a photographic film

f-number — the ratio of the base diameter of an image-forming cone of light to its height

fringe frequency — the number of fringes per unit of length in, e.g., a grating, hologram, or interferogram

grating — an object which diffracts light reflected or transmitted by it

laser — acronym for "light amplification by stimulated emission of radiation," a source of highly coherent, monochromatic light

mode — a radiation field pattern which is independent of time (a laser which oscillates in a single transverse mode emits spatially coherent radiation)

object beam (or wave) — the light which is scattered or transmitted by the object to the hologram

optical path — the product of the distance travelled by a light ray and the refractive index of the medium in which it is propagating

phase — a property of a sinusoidal oscillation which describes the portion of a cycle completed at any given instant

phase grating — a grating consisting of a periodic refractive-index structure, as opposed to an amplitude grating in which the optical density varies periodically

phase modulation — a time- or space-varying modification of the phase of some oscillation

phase object — a transparent object which is characterized by its refractive-index field

phasor — a vector representation of a sinusoidal oscillation

plane wave — a propagating, sinusoidal disturbance with a constant phase across a plane in space

polarized — description of a light beam for which the electric vector is oriented in a single (linear) direction

quarter-wave plate — an optical element which retards the oscillation of a certain polarization by one-fourth of a cycle with respect to light polarized at 90° to it

real image — an image which is formed on the viewer's side of an optical element such as a hologram or lens

reference beam (or wave) — the light which is coherently added to the object beam to form a hologram

reference-beam compensation — the process by which the reference beam sources for each frequency must be modified to have the reconstructed images interfere as desired when multiple-frequency holograms are made

refractive index — the ratio of the speed of light in vacuo to the speed of light in a medium

scalar diffraction theory — a principle that although light is a vector quality, certain scalar quantities can be used to calculate the radiation patterns approximately

signal beam (or wave) — synonym for object beam (or wave)

spatial coherence — a measure of the degree of phase correlation at two different points illuminated by the same light source, primarily determined by the width of the light source (a laser oscillating in a single transverse mode produces highly spatially coherent light)

spatial filter — a transparency or aperture which is used to modify or sample selectively the Fourier transform of a light wave in spatial-filtering operations

130

spatial filtering—selective extraction of information which is encoded by spatial modulation of a light wave, particularly associated with modifying the two-dimensional Fourier transform of a light wave which is formed in the back focal plane of a spherical lens

spatial frequency—if a plane wave impinges on a plane of arbitrary orientation, its phase will be periodic across that plane; the reciprocal of this period is the spatial frequency of that wave

speckle—diffuse objects illuminated by coherent light appear to be illuminated with a granular light pattern called speckle which changes as one changes his viewing position and which is caused by the random interference of the scattered light

telecentric—an image-forming system which collects light from all object points in cones of light with centroid rays parallel to the optical axis

telescope—an image-forming system which converts entering plane waves into exiting plane waves

temporal coherence—a measure of the degree of phase correlation with time between two fixed points along a given ray direction

virtual image—an image which appears to form on the side of an optical element, such as a hologram or lens, opposite the viewer

visibility (of fringes)—the ratio of the difference of the maximum and minimum intensities in an interference pattern to their sum

white-light hologram—a hologram in which the interference fringes are nearly parallel to the surface of the recording film and which can be used to yield nearly single-color images with a multicolor (white) reconstruction beam

REFERENCES

1. D. Gabor, "A New Microscopic Principle," Nat., Vol. 161, 1948, p. 777.

2. D. Gabor, "Microscopy by Reconstructed Wavefronts," Proc. Roy. Soc. Lond., Vol. 197 A, 1949, p. 454.

3. E. N. Leith and J. Upatnieks, "Reconstructed Wavefronts and Communication Theory," J. Opt. Soc. Am., Vol. 52, 1962, p. 1123.

4. E. N. Leith and J. Upatnieks, "Wavefront Reconstruction with Diffused Illumination and Three-Dimensional Objects," J. Opt. Soc. Am., Vol. 54, 1964, p. 1295.

5. O. Bryngdahl, "Polarizing Holography," J. Opt. Soc. Am., Vol. 57, 1967, p. 545.

6. M. E. Fourney, A. P. Waggoner, and K. V. Mate, "Recording Polarization Effects Via Holography," J. Opt. Soc. Am., Vol. 58, 1968, p. 701.

7. M. H. Horman, "An Application of Wavefront Reconstruction to Interferometry," App. Opt., Vol. 4, 1965, p. 333.

8. R. L. Powell and K. A. Stetson, "Interferometric Vibration Analysis by Wavefront Reconstruction," J. Opt. Soc. Am., Vol. 55, 1965, p. 1593.

9. K. A. Haines and B. P. Hildebrand, "Surface Deformation Measurement Using the Wavefront Reconstruction Technique," Appl. Opt., Vol. 5, 1966, p. 595.

10. J. M. Burch, "The Application of Lasers in Production Engineering," Prod. Eng., Vol. 44, 1965, p. 431.

11. L. O. Heflinger, R. F. Wuerker, and R. E. Brooks, "Holographic Interferometry," J. Appl. Phys., Vol. 37, 1966, p. 642.

12. E. B. Aleksandrov and A. M. Bonch-Bruevich, "Investigation of Surface Strains by the Hologram Technique," Sov. Phys.-Tech. Phys., Vol. 12, 1967, p. 258.

13. J. E. Sollid, "Holographic Interferometry Applied to Measurements of Small Static Displacements of Diffusely Reflecting Surfaces," Appl. Opt., Vol. 8, 1969, p. 1587.

14. A. E. Ennos, "Measurements of In-Plane Surface Strain by Hologram Interferometry," J. Sci. Instrum., Series 2, Vol. 1, 1968, p. 731.

15. T. Tsuruta, N. Shiotake, and Y. Itoh, "Formation and Localization of Holographically Produced Interference Fringes," Opt. Acta, Vol. 16, 1969, p. 723.

16. J. C. Vienot, C. J. Frochly, J. Monneret, and J. Pasteur, "Hologram Interferometry: Surface Displacement Fringe Analysis as an Approach to the Study of Mechanical Strains and Other Applications to the Determination of Anistropy in Transparent Objects," Symposium on the Engineering Uses of Holography, Glasgow, September 1968, pp. 17-20.

17. K. A. Stetson, "A Rigorous Treatment of the Fringes of Hologram Interferometry," Optik, Vol. 29, 1969, p. 386.

18. K. Biedermann and N. E. Molin, "Combining Hypersensitization and Rapid In-Situ Processing for Time-Average Hologram Interferometry," J. Phys. E. (Sci. Instrum.) [to be published].

19. K. A. Stetson and R. L. Powell, "Interferometric Hologram Evaluation and Real-Time Vibration Analysis of Diffuse Objects," J. Opt. Soc. Am., Vol. 55, 1965, p. 1694.

20. E. Archbold and A. E. Ennos, "Observation of Surface Vibration Modes by Stroboscopic Hologram Interferometry," Nat., Vol. 217, 1968, p. 942.

21. B. P. Hildebrand and K. A. Haines, "Multiple Wavelength and Multiple Source Holography Applied to Contour Generation," J. Opt. Soc. Am., Vol. 57, 1967, p. 155.

22. T. Tsuruta, N. Shiotake, J. Tsujiuchi, and K. Matsuda, "Holographic Generation of Contour Maps of a Diffusely Reflecting Surface by Using the Immersion Method," Jap. J. Appl. Phys., Vol. 6, 1967, p. 661.

23. J. S. Zelenka and J. R. Varner, "Multiple-Index Contouring," Appl. Opt., Vol. 8, 1969, p. 1431.

24. C. M. Vest, E. L. McKague, Jr., and A. A. Friesem, "Holographic Detection of Microcracks," J. Basic Eng. (ASME), Vol. 93, 1971, p. 237.

25. D. R. Wells, "NDT of Sandwich Structures by Holographic Interferometry," Mater. Eval., Vol. 27, 1969, p. 225.

26. D. Denby and J. N. Butters, "Holography as an Engineering Tool," New Sci., Vol. 45, 1970, p. 394.

27. G. D. Currie, "High Power, Single-Mode He-Ne Laser," Appl. Opt., Vol. 8, 1969, p. 1068.

28. J. M. Burch, et al., "Dual- and Multiple-Beam Interferometry by Wavefront Reconstruction," Nat., Vol. 209, 1966, p. 1015.

29. K. Biedermann, "Attempts to Increase the Holographic Exposure Index of Photographic Materials," Appl. Opt., Vol. 10, 1971, p. 584.

30. E. Champagne and L. Kersch, "Control of Holographic Interferometric Fringe Patterns," J. Opt. Soc. Am., Vol. 59, 1969, p. 1535A.

31. L. A. Kersch, "Advanced Concepts of Holographic Nondestructive Testing," Mater. Eval., Vol. 29, 1971, p. 125.

32. E. N. Leith, et al., "Investigation of Holographic Testing Techniques," Report No. 2420-9-P, Willow Run Laboratories of the Institute of Science and Technology, The University of Michigan, Ann Arbor, April 1970.

33. E. N. Leith, et al., "Investigation of Holographic Testing Techniques," Report No. 2420-5-P, Willow Run Laboratories of the Institute of Science and Technology, The University of Michigan, Ann Arbor, August 1969.

34. M. E. Fourney, "Application of Holography to Photoelasticity," Exp. Mech., Vol. 8, No. 1, 1968, p. 33.

35. J. D. Hovanesian, V. Brcic, and R. L. Powell, "A New Experimental Stress-Optic Method: Stress-Holo-Interferometry," Exp. Mech., Vol. 8, No. 8, 1968, p. 362.

36. H. M. Chau, "Holographic Interferometer from Isopachic Stress Analysis," Rev. Sci. Instr., Vol. 39, 1968, p. 1789.

37. M. E. Fourney and K. V. Mate, "Further Application of Holography to Photoelasticity," Exp. Mech., Vol. 10, No. 5, 1970, p. 177.

38. R. J. Sanford and A. J. Durelli, "Interpretation of Fringes in Stress-Holo-Interferometry," Exp. Mech., Vol. 11, No. 4, 1971, p. 161.

39. R. O'Regan and T. D. Dudderar, "A New Holographic Interferometer for Stress Analysis," Exp. Mech., Vol. 11, No. 6, 1971, p. 241.

40. L. H. Tanner, "Scope and Limitations of Three-Dimensional Holography of Phase Objects," J. Sci. Instrum., Vol. 44, 1967, p. 1011.

41. L. H. Tanner, "A Study of Fringe Clarity in Laser Interferometry and Holography," J. Sci. Instrum., Series 2, Vol. 1, 1968, p. 517.

42. L. I. Goldfischer, "Autocorrelation Function and Power Spectral Density of Laser-Produced Speckle Patterns," J. Opt. Soc. Am., Vol. 55, March 1965, p. 247.

43. J. W. Goodman, Introduction to Fourier Optics, McGraw-Hill, 1968.

44. E. N. Leith and J. Upatnieks, "Imagery with Pseudo-Randomly Diffused Coherent Illumination," Appl. Opt., Vol. 7, October 1968, p. 2085.

45. R. D. Matulka and D. J. Collins, "Determination of Three-Dimensional Density Fields from Holographic Interferograms," J. Appl. Phys., Vol. 42, 1971, p. 1109.

46. C. D. Maldenado and H. N. Olsen, "New Method for Obtaining Emission Coefficients from Emitted Spectral Intensities," Part I, J. Opt. Soc. Am., Vol. 55, 1965, p. 1247.

47. C. D. Maldenado and H. N. Olsen, "New Method for Obtaining Emission Coefficients from Emitted Spectral Intensities," Part II, J. Opt. Soc. Am., Vol. 56, 1966, p. 1305.

48. H. N. Olsen, et al., "A Numerical Method for Obtaining Internal Emission Coefficients from Externally Measured Spectral Intensities of Analytical Plasmas," J. Quant. Spectry. Radiat. Transfer, Vol. 8, 1968, p. 1419.

49. H. N. Olsen, et al., Report No. ARL 66-0016, Aerospace Research Laboratory, 1966.

50. P. D. Rowley, "Quantitative Interpretation of Three-Dimensional Weakly Refractive Phase Objects Using Holographic Interferometry," J. Opt. Soc. Am., Vol. 59, 1969, p. 1496.

51. M. V. Berry and D. F. Gibbs, "The Interpretation of Optical Projections," Proc. Roy. Soc. Lond., Vol. 314A, 1970, p. 143.

52. L. H. Tanner, "The Application of Berry-Gibbs Theory to Phase Objects, Using Interferometry, Holography, or Schlieren Methods," J. Sci. Instrum., Vol. 3, 1970, p. 987.

53. W. Alwang, et al., "Optical Techniques for Flow Visualization and Flow Field Measurements in Aircraft Turbomachinery," Report No. PWA-3942, Pratt and Whitney Aircraft Corp., 1970.

54. C. B. Moler, "Notes on Matrix Computations," The University of Michigan, Ann Arbor, 1971 [unpublished manuscript].

55. J. W. Goodman, "Wavefront-Reconstruction Imaging Through Random Media," Appl. Phys. Lett., Vol. 8, 1966, p. 311.

56. J. W. Goodman, et al., "Experiments in Long-Distance Holographic Imagery," Appl. Opt., Vol. 8, 1969, p. 1581.

57. O. Bryngdahl and A. Lohmann, "Holographic Penetration of an Inhomogeneous Medium," J. Opt. Soc. Am., Vol. 59, 1969, p. 1245.

58. E. N. Leith, et al., "Holographic Data Storage in Three-Dimensional Media," Appl. Opt., Vol. 5, 1966, p. 1303.

59. B. P. Hildebrand and K. A. Haines, "Multiple-Wavelength and Multiple Source Holography Applied to Contour Generation," J. Opt. Soc. Am., Vol. 57, 1967, p. 155.

60. R. E. Brooks and L. O. Heflinger, "Moiré Gauging Using Optical Interference Patterns," Appl. Opt., Vol. 8, 1969, p. 935.

61. G. A. Massey, Report No. NASA-CR-75643 (1965) and Report No. NASA-CR-985 (1968), National Technical Information Service, Springfield, Virginia 22151.

62. N. Fernelius and C. Tome, "Vibration-Analysis Studies Using Changes of Laser Speckle," J. Opt. Soc. Am., Vol. 61, 1971, p. 566.

63. B. Eliasson and M. Mottier, "Determination of the Granular Radiance Distribution of a Diffuser and Its Use for Vibration Analysis," J. Opt. Soc. Am., Vol. 61, 1971, p. 559.

64. E. Archbold, et al., "Visual Observation of Surface Vibration Nodal Patterns," Nat., Vol. 22, 1969, p. 263.

65. L. Ek and N. E. Molin, "Detection of the Nodal Lines and the Amplitude of Vibration Measurement by Speckle Interferometry," Opt. Commun., Vol. 2, 1971, p. 419.

66. C. C. Aleksoff, "Temporally Modulated Holography," Appl. Opt., Vol. 10, 1971, p. 1329.

67. D. B. Neumann, et al., "Holographic Technique for Determining the Phase of Vibrating Objects," Appl. Opt., Vol. 9, 1970, p. 1357.

68. B. P. Hildebrand and K. A. Haines, "The Generation of Three-Dimensional Contour Maps by Wavefront Reconstruction," Phys. Lett., Vol. 21, 1965, p. 422.

69. B. P. Hildebrand and K. A. Haines, "Multiple-Wavelength and Multiple-Source Holography Applied to Contour Generation," J. Opt. Soc. Am., Vol. 57, 1967, p. 155.

70. B. P. Hildebrand, A General Analysis of Contour Holography, Ph.D. Dissertation, The University of Michigan, Ann Arbor, 1967.

71. Tsuruta, et al., "Holographic Generation of Contour Map of Diffusely Reflecting Surface by Using Immersion Method," Jap. J. Appl. Phys., Vol. 6, 1967., p. 661.

72. J. S. Zelenka and J. R. Varner, "A New Method for Generating Depth Contours Holographically," Appl. Opt., Vol. 7, 1968, p. 2107.

73. J. R. Varner, Multiple-Frequency Holographic Contouring, Ph.D. Dissertation, The University of Michigan, Ann Arbor, 1971.

74. J. R. Varner, "Simplified Multiple-Frequency Holographic Contouring," Appl. Opt., Vol. 10, 1971, p. 212.

75. 14th Annual Tri-Service Radar Symposium Record (U), Vol. II, Willow Run Laboratories of the Institute of Science and Technology, The University of Michigan, Ann Arbor, 1968, p. 114,(SECRET).

76. E. N. Leith, "Improvement of Image Quality by Exploitation of Excess Channel Capacity," Contributed Paper, Optical Society of America, meeting, Philadelphia, Pennsylvania, October 1970.

77. G. D. Currie, "High-Power, Single-Mode He-Ne Laser," Appl. Opt., Vol. 8, 1969, p. 1068.

78. D. M. Meadows, et al., "Generation of Surface Contours by Moiré Patterns," Appl. Opt., Vol. 9, 1970, p. 942.

79. H. Takasaki, "Moiré Topography," Appl. Opt., Vol. 9, 1970, p. 1467.

80. L. O. Heflinger and R. F. Wuerker, "Holographic Contouring via Multifrequency Lasers," Appl. Phys. Lett., Vol. 15, 1969, p. 28.

81. W. B. Ribbens, "Interferometric Surface Roughness Measurement," Appl. Opt., Vol. 8, November 1969, p. 2173.

135